Studies of Degradation of Organic Solar Cell Materials using Electrical Scanning Probe Microscopy

DISSERTATION

zur Erlangung des Grades
„Doktor der Naturwissenschaften“
am Fachbereich Physik, Mathematik und Informatik
der Johannes Gutenberg-Universität in Mainz

vorgelegt von

Esha Sen Gupta
geboren in Braunschweig, Deutschland

Mainz, den 23. Oktober 2012

Dedicated to my parents
for their love, encouragement
and endless support.

Zusammenfassung

Im Bereich organischer Solarzellen konzentriert sich die Forschung vor allem auf die Optimierung des Bandabstandes von organischen Molekülen, um eine Steigerung des Wirkungsgrades zu erreichen. So dienen Moleküle mit niedriger Bandlücke als Elektronendonor, welche bikontinuierlich mit einem Elektronenakzeptor, typischerweise ein Fullerenderivat, vermischt sind. Die Phasenseparation innerhalb dieser photoaktiven Schicht liegt dabei in der Größenordnung von Nanometern. Der höchste bekannte Wirkungsgrad organischer Solarzellen liegt zurzeit bei 10,6%. Organische halbleitende Materialien unterscheiden sich von anorganischen Halbleitern im Auftreten stark gebundener Exzitonen, sog. Elektron-Loch-Paare. Diese Frenkel-Exzitonen besitzen eine sehr große Bindungsenergie im Bereich von 0,3-1 eV, die in der niedrigen Dielektrizitätskonstante ($\epsilon_r \approx$ 2-4) des organischen Materials begründet liegt. Daher reicht das elektrische Feld allein nicht aus, um eine Trennung der Exzitonen in freie Ladungsträger zu ermöglichen. Es ist eine zusätzliche Antriebskraft notwendig, welche in der Energiedifferenz zwischen den LUMOs des Donor- und Akzeptormaterials besteht. Darüber hinaus hängt der Wirkungsgrad organischer Solarzellen von der Energiedifferenz zwischen dem HOMO des Donors und dem LUMO des Akzeptors ab. Daher ist eine genaue Charakterisierung und Kontrolle der Energieniveaus der beteiligten Materialien unerlässlich. Eine Veränderung dieser Energieniveaus durch z.B. äußere Einflüsse hat eine Verringerung des Wirkungsgrades der Solarzelle zur direkten Folge.

Besonders die lichtinduzierte Alterung hat einen erheblichen Einfluss auf die Morphologie der photoaktiven Schicht und damit auf die elektrischen Eigenschaften der Solarzelle, weshalb ein gutes Verständnis dieser Alterungsmechanismen und ihrer Auswirkungen auf das Material auf molekularer Ebene von großer Bedeutung ist. Die Rasterkraftmikroskopie bietet die Möglichkeit, die bikontinuierlich strukturierte Morphologie der photoaktiven Schicht im Nanometerbereich abzubilden. Des Weiteren können mittels elektrischer Modi der Rasterkraftmikroskopie die Kontaktpotentialdifferenzen (CPD) der Materialien bestimmt werden, welche eine Ableitung der Energieniveaus der Materialien ermöglichen. Somit ist die Rasterkraftmikroskopie eine ideale Methode zur Charakterisierung der Morphologie, der Änderungen des Oberflächenpotentials sowie der Leitfähigkeit unter simulierten Betriebsbedingungen.

Ziel dieser Arbeit war es die Photooxidation organischer Solarzellenmaterialien, welche einen bedeutenden Anteil an der Alterung organischer Solarzellen haben, darzustellen. Mittels Rasterkraftmikroskopie, NMR Spektroskopie sowie UV-Vis Spektroskopie konnte ich die der lichtinduzierten Alterung zugrundeliegenden chemischen Reaktionen innerhalb der photoaktiven Schicht identifizieren. Diese experimentellen Ergebnisse erlaubten es mir weiter, die Energieniveaus sowie deren Verschiebung als Folge der Alterung abzuleiten und somit ein besseres Verständnis der Physik innerhalb der organischen Solarzellen zu erlangen. Außerdem wurde die Alterung durch eine Korrelation der lokalen Änderung der CPD und der Leitfähigkeit mit den Solarzellparametern, d.h., der offenen Klemmspannung und dem Kurzschlussstrom, quantifiziert. Mittels der zeitaufgelösten elektrostatischen Rasterkraftmikroskopie konnten darüber hinaus selektiv Einblicke in die Dynamik der Ladungsgenerierung in Domänen des Akzeptors und des Donors in der photoaktiven Schicht gewonnen werden. Es konnte beobachtet werden, dass unter Bestrahlung zunächst die Akzeptormoleküle oxidiert werden und somit vorerst die Alterung der Donormoleküle verhindert wird.

Die definierte Modifizierung der Austrittsarbeit von Metallen kann durch eine chemische Reaktion in Flüssigkeiten erreicht werden, bei der Monolagen organischer Moleküle auf der Metalloberfläche adsorbieren. Dies ist besonders im Bereich der Optoelektronik von Interesse, da der Wirkungsgrad entscheidend von der Lage der Energieniveaus der Elektrodenmaterialen sowie der organischen Materialien zueinander abhängt. In dieser Arbeit habe ich Kelvinsonden-Rasterkraftmikroskopie in Flüssigkeiten eingesetzt, um die Änderung der Austrittsarbeit von Gold durch Adsorption von Hexadekanthiolen in-situ zu untersuchen.

Zusammenfassend führen die in dieser Arbeit vorgestellten Methoden demnach zu einem besseren Verständnis der Photooxidation der photoaktiven Materialien im Nanobereich. Des Weiteren wird hierdurch eine schnelle Selektion geeigneter optoelektronischer Materialien ermöglicht, da ein Vergleich ihrer Stabilität untersucht werden kann, ohne eine zeit- und materialintensive Präparation vollfunktionaler Solarzellen vorauszusetzen.

Abstract

Intense research is being done in the field of organic photovoltaics in order to synthesize low band-gap organic molecules. These molecules are electron donors which feature in combination with acceptor molecules, typically fullerene derivatives, forming an active blend. This active blend has phase separated bicontinuous morphology on a nanometer scale. The highest recorded power conversion efficiencies for such cells have been 10.6%. Organic semiconductors differ from inorganic ones due to the presence of tightly bonded excitons (electron-hole pairs) resulting from their low dielectric constant ($\epsilon_r \approx$2-4). An additional driving force is required to separate such Frenkel excitons since their binding energy (0.3-1 eV) is too large to be dissociated by an electric field alone. This additional driving force arises from the energy difference between the lowest unoccupied molecular orbital (LUMO) of the donor and the acceptor materials. Moreover, the efficiency of the cells also depends on the difference between the highest occupied molecular orbital (HOMO) of the donor and LUMO of the acceptor. Therefore, a precise control and estimation of these energy levels are required. Furthermore any external influences that change the energy levels will cause a degradation of the power conversion efficiency of organic solar cell materials.

In particular, the role of photo-induced degradation on the morphology and electrical performance is a major contribution to degradation and needs to be understood on a nanometer scale. Scanning Probe Microscopy (SPM) offers the resolution to image the nanometer scale bicontinuous morphology. In addition SPM can be operated to measure the local contact potential difference (CPD) of materials from which energy levels in the materials can be derived. Thus SPM is a unique method for the characterization of surface morphology, potential changes and conductivity changes under operating conditions.

In the present work, I describe investigations of organic photovoltaic materials upon photo-oxidation which is one of the major causes of degradation of these solar cell materials. SPM, Nuclear Magnetic Resonance (NMR) and UV-Vis spectroscopy studies allowed me to identify the chemical reactions occurring inside the active layer upon photo-oxidation. From the measured data, it was possible to deduce the energy levels and explain the various shifts which gave a better understanding of the physics of the device. In addition, I was able to quantify the degradation by correlating the local changes in the CPD and conductivity to the device characteristics, i.e., open circuit voltage and short circuit current. Furthermore, time-resolved electrostatic force microscopy (tr-EFM) allowed us to probe dynamic processes like the charging rate of the individual donor and acceptor domains within the active blend. Upon photo-oxidation, it was observed, that the acceptor molecules got oxidized first preventing the donor polymer from degrading.

Work functions of electrodes can be tailored by modifying the interface with monomolecular thin layers of molecules which are made by a chemical reaction in liquids. These modifications in the work function are particularly attractive for opto-electronic devices whose performance depends on the band alignment between the electrodes and the active material. In order to measure the shift in work function on a nanometer scale, I used KPFM in situ, which means in liquids, to follow changes in the work function of Au upon hexadecanethiol adsorption from decane.

All the above investigations give us a better understanding of the photo-degradation processes of the active material at the nanoscale. Also, a method to compare various new materials used for organic solar cells for stability is proposed which eliminates the requirement to make fully functional devices saving time and additional engineering efforts.

Contents

1

Introduction

The search for alternate sources of energy has gained a lot of importance these days with the depletion of fossil fuels that are non-renewable and their use contributes to a global change in climate. Also, these fossil fuels have environmentally damaging retrieval techniques and increasing costs. Out of the renewable sources of energy that include wind, sunlight, water and geothermal heat, photovoltaics have been the fastest growing industry in energy technology since 2004 due to the decreasing cost of installation as reported by the Lawrence Berkeley National Laboratory. Solar photovoltaic cells convert sunlight to electricity and their production has been increasing by an average of more than 20% each year [1].

The field of photovoltaics began with the discovery of photocurrent by Becquerel in 1839 when he took platinum electrodes covered with silver bromide and illuminated them in aqueous solution. The first practical photovoltaic cell was developed by Daryl Chapin, Calvin Souther Fuller and Gerald Pearson in 1954 at Bell Laboratories [2]. It was made from diffused silicon and reached a power conversion efficiency (i.e. the ratio between useful power output and the input) of 6%. In 1958, these photovoltaics were used outside the Vanguard I satellite which enabled the extension of the mission time without major changes to the spacecraft. The mission was a huge success and solar cells were quickly used in many new satellites. The prices of these cells started coming down by various improvements in the production techniques starting in the late 1960s with Elliot

Berman, who, while working in Solar Power Corporation in New Jersey, came up with the idea of sandwiching a silicon wafer between a circuit board in the back and acrylic plastic in the front.

Photovoltaic devices based on organic materials dramatically reduce the price since such materials are very easy and inexpensive to fabricate compared to inorganic semi-conductors. In 1977, Hideki Shirakawa, Edwin J. Louis, Alan G. MacDiarmid, Chwan K. Chiang and Alan J. Heeger published a paper on the synthesis of electrically conducting organic polymers [3]. These materials were ideal for making photovoltaics instead of inorganic materials such as Si since not only were they readily available but also had very low processing costs and were very simple to prepare. In addition, the solar cells prepared from these materials were very light weight as compared to the inorganic ones and could be processed into rolls as they could be made on flexible substrates. In 2000, the nobel prize was awarded for the discovery of organic photovoltaics to Alan Heeger, Alan MacDiarmid and Hideki Shirakawa. The highest efficiencies reported with these cells is 10.6% [4] which is way below the inorganic ones which have attained an efficiency of 40% in research labs. Inspite of this, the above mentioned advantages make organic materials very attractive in the field of photovoltaics which is the reason why organic photovoltaics is an emerging field of research these days.

Other than ensuring high efficiency and low cost of manufacturing for these solar cell devices, another important challenge is to prevent their degradation. In 1977, David L. Staebler and Christopher R. Wronski observed a rapid decrease in the performance of a Si solar cell when it was illuminated. The observed rapid decrease of performance came to be known as the Staebler-Wronski effect [5]. This effect was an unpleasant surprise at that time and scientists started investigating in this area to find a cure for this problem. Early reports on degradation of organic photovoltaics began to appear around 1990 [6]. Since then a lot of techniques have been used to study the degradation processes which not only occur due to exposure to sunlight but also due to the environment in which these solar cells are kept. In a review article on degradation of organic photovoltaics, Krebs et al. [7] reported that ***"The polymer solar cell is currently the ultimate in terms of complexity and presents enormous variability in all aspects.***

It is therefore not unexpected that polymer solar cells present the most uncontrollable situations in terms of stability." In my thesis, I will focus on the degradation of organic solar cell materials. However, to study the degradation, we first have to understand the various processes occuring inside these solar cells.

1.1 Basics of Solar Cells

An inorganic solar cell is basically a p-n junction diode with a photogenerated current (Figure 1.1a). Absorption of photons creates minority carriers which diffuse towards the junction. If these minority carriers can drift across the junction without recombination then a photocurrent is created.

The ideal diode characteristics for an illuminated cell is shown in Figure 1.1c. The equation for the IV characteristics is given by

$$I = I_S(e^{\frac{qV}{K_BT}} - 1) - I_L \tag{1.1}$$

where I_S is the saturation current in reverse bias at zero illumination, q is the charge of the carrier, V is the applied voltage and K_B and T are the Boltzman constant and the temperature, respectively. I_L is the photogenerated current. In an ideal cell, at V = 0 we obtain the short circuit current (I_{SC}).

The power extracted from the device is determined from the product of IV at the operating point as determined by the load. The maximum power corresponds to the operating point that gives the largest IV area. The equation for the maximum power is given by

$$P_m = I_mV_m = I_L[V_{OC} - \frac{K_BT}{q}ln(1 + \frac{qV_m}{K_BT}) - \frac{K_BT}{q}] = I_L(\frac{E_m}{q}) \tag{1.2}$$

Here, V_{OC} is the open circuit voltage, or the voltage across the terminals when no current flows throught the system and E_m is the maximum energy that can be extracted per photon. The fill factor (FF) is defined as the ratio of the maximum

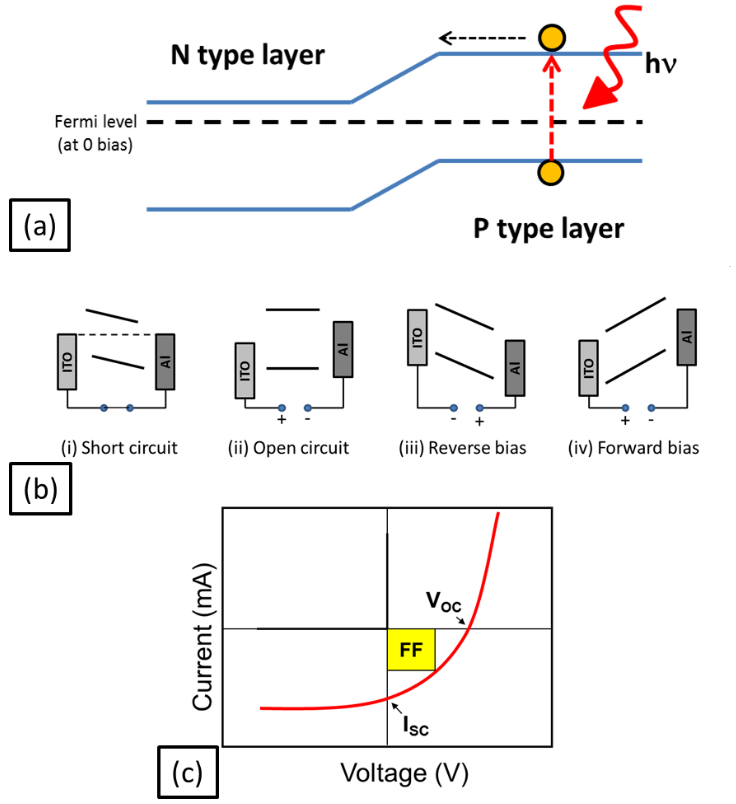

Figure 1.1: (a) Schematic of an energy band diagram for a p-n junction (b) Different working regimes of a p-n juction device (c) IV curve showing ideal diode characteristics

power to the product of the V_{OC} and I_{SC}. This is a key parameter for determining the performance of the solar cells.

The efficiency of the cells is limited by two fundamental parameters:

(1) The fraction of solar photons absorbed by the cell. This can be calculated by integrating over the whole solar spectrum and including the cutoff wavelength of the absorber layer.

$$\eta_{abs} = \frac{\int_{E_g}^{\infty} n_E(E)dE}{\int_{0}^{\infty} n_E(E)dE} \tag{1.3}$$

where n_E is the number of photons having energy E and E_g is the energy band gap.

(2) The electrical energy created per photon. Since not all the photon energy gets converted into electrical energy, the maximum power is the product of the absorption rate and the mean electrical energy created per photon. Ideally, E_m is proportional to the bandgap. For narrow bandgap materials, although a larger proportion of photons will be absorbed, however, there will be less electrical energy per photon.

1.2 Organic Solar Cells

The name "organic" comes from the use of carbon-based materials, e.g. polymers, as opposed to traditional electronics which relies on inorganic conductors like silicon or copper. The first organic solar cell device was described by Tang et al. in 1986 [8]. They reported devices achieving power efficiencies of nearly 1% under simulated solar illumination. The device consisted of a 25 nm thick layer of copper phthalocyanine (CuPc) on an ITO coated glass substrate. This layer was followed by a 45 nm thick layer of 3,4,9,10-perylenetetracarboxylic-bis-benzimidazole (PTCBI). A silver electrode was then evaporated on top of the structure. This organic solar cell device had an I_{SC} of 2.3 ± 0.1 mA/cm^2 and V_{OC} of 0.45 ± 0.02 V. Furthermore, the lifetime of these devices was very low. These organic materials degraded very quickly in presence of oxygen and various other factors. To increase the lifetime of these devices one needs to understand the basics of the degradation mechanisms. Before I go into the details of degradation mechanisms, we first need to understand the working of organic photovoltaics.

1.2.1 Working of Organic Solar Cells

Organic photovoltaics have an active light absorbing region consisting of two materials, namely, electron donor and electron acceptor. Semiconducting polymers, which act as the donor material, consist of sp^2-hybridized carbon atoms which form a system of conjugated double bonds. These double bonds lead to delocalized π-systems with a large electrical polarizability. Furthermore, the

$\pi - \pi^*$-transition due to the excitation of an electron between the bonding and antibonding p_z-orbitals causes an absorbance within the visible range of light spectra. All electrons in the p_z -orbitals of every sp^2-hybridized carbon atom form collectively the π-band. Due to the Peierls instability the half filled p_z-orbitals split up into the bonding π-band and the antibonding π^*-band which are equivalent to the HOMO (highest occupied molecular orbital) and LUMO (lowest unoccupied molecular orbital) energy levels. The optical band gap between these two levels is approximately $\Delta E \approx 2$ eV for most conjugated polymers [9]. This value corresponds to an absorption up to a wavelength of $\lambda = 650$ nm. In comparison, the silicon band gap is around $\Delta E \approx 1.1$ eV, which allows an absorption in a larger wavelength range up to $\lambda = 1100$ nm. Apart from the semiconducting polymer which serves as an electron donor, an electron acceptor is needed for a working solar cell device. This acceptor component can either be another polymer or a fullerene compound.

The active region, consisting of the electron donor and acceptor, is sandwiched between the two electrodes (Figure 1.2a). One of the electrodes has to be transparent so that light can fall on the active region. The transparent electrode is usually made of indium-tin-oxide (ITO) and the other electrode is usually made from aluminium. The ITO is the hole collecting electrode and Al is an electron collecting electrode. Unlike inorganic solar cells, where the photocarriers are generated by the absorption of light within the bulk of the intrinsic layer and are transferred to the electrodes by a built-in potential due to the difference in the fermi level relative to the bands of the p-type and n-type layers; light absorption in an organic photovoltaic generates a neutral excited state similar to a tightly bound Frenkel exciton.

When light falls on the active region, a photon excites an electron from HOMO to the LUMO forming an electron-hole pair (typically in the donor material) (Figure 1.2b). The charges remain bound in the form of an exciton. The formation of an exciton is favourable in organic solar cells since they have a small Bohr radius of carriers (r_B), given by,

$$r_B = r_0 \epsilon \frac{m_e}{m_{eff}} \tag{1.4}$$

where r_0 is 0.53 Angstrom (radius of H-atom), m_e is the mass of free electron in vacuum and m_{eff} is the effective mass of electron in the device. A charge becomes free from its Coloumb attraction to an opposite charge if the energy of attraction becomes less than $K_B T$ which is the average thermal energy of the carrier. This occurs when

$$E = \frac{q^2}{4\pi\epsilon_0\epsilon}\frac{1}{r_C} = K_B T \tag{1.5}$$

r_C is the critical distance between the 2 charges.

Excitonic behaviour occurs when $r_C \geq r_B$. In this regime, excitons are formed rather than free electrons and hole pairs. It is usually difficult to separate the excitons into free charges since they have a low dielectric constant and high degree of localization which leads to binding energies of the order of 0.1-1 eV. [10, 11]. These excitons diffuse through the donor material to the donor-acceptor interface. At this interface, the exciton dissociates and the electron goes to one electrode and the hole to the other. The exciton dissociation is achieved due to the difference in work function of the two materials which is greater than the binding energy of the excitons. The photoinduced charge transfer takes place within less than 50 fs. Certain processes counteract this exciton dissociation and thereby lead to efficiency loss. Some of the processes are geminate, non-geminate and trap assisted recombination. In geminate recombination, the electron and hole merge back because the field is not strong enough for separation. When electron and hole from different excitons recombine it is known as non-geminate recombination. Trap assisted recombination occurs when an electron falls into a trap caused by the presence of a structural defect [12]. All the other competing processes like photoluminescence (ns) and charge recombination (μs) take place on a much larger timescale compared to the above mentioned processes [9].

The electochemical potential energy (E) is a powerful driving force for carrier separation. $E = U + \mu$, where U is the electrical potential energy and μ is the chemical potential energy. ∇E is the fundamental force that drives the charge carrier fluxes. In equilibrium, $E = E_F$ and $\nabla E = 0$. Away from equilibrium, the Fermi levels for electrons and holes are different. The spatial gradients of these

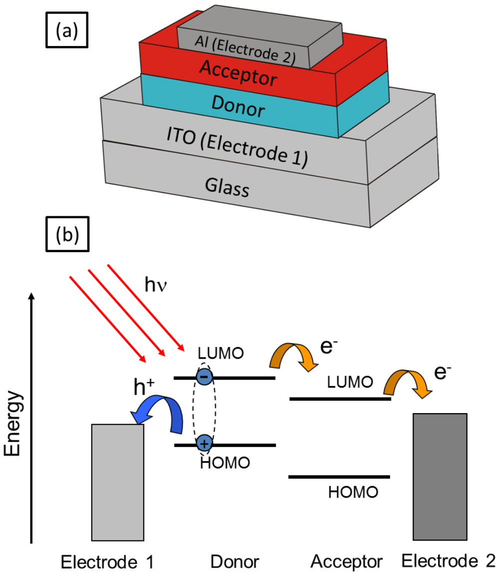

Figure 1.2: (a) Schematic of the different layers of an organic solar cell. (b) Energy level diagram representing the different layers

'quasi' Fermi levels, given by, ∇E_{Fn} and ∇E_{Fp} drives the fluxes of electrons and holes. The general expression for the current density is given by

$$J_n(x) = n(x)\mu_n[\nabla U(x) + \nabla \mu(x)] = n(x)\mu_n[\nabla E_{Fn}(x)] \tag{1.6}$$

where n(x) is the electron concentration and μ_n is the electron mobility. In organic solar cells, $\nabla \mu$ is the dominant driving force as compared to the inorganic solar cells where ∇U is more dominant. This results in higher V_{OC} in organic solar cells since V_{OC} is determined by the driving forces [13, 14].

The distance d travelled by the charge carriers within a device is a product of the charge carrier mobility μ, charge carrier lifetime τ and the internal electric field F. This internal electric field F originates from the difference in the electrode work functions.

$$d = \mu \cdot \tau \cdot F \tag{1.7}$$

Hoppe et al. calculated the value of the drift length d as 100 nm in short circuit conditions from the above equation assuming charge carrier mobilities of $10^{-4} cm^2/Vs$ and charge carrier lifetimes of 1 μs. The two electrodes were made of gold ($\phi = 5.2\ eV$) and aluminium ($\phi = 4.3\ eV$) which results in an electric field of $10^5\ V/cm$ for an active layer thickness of 90 nm. However, an exciton can travel a distance of 10 nm as reported by Yang et al. [15]. For this reason, very thin layers of donor material are required. Having an exteremely thin donor layer results in less light gathering which then results in less exciton creation. To overcome the conflict between thin films required for good exciton diffusion and thick films for good light harvesting, the concept of bulk heterojunction was introduced.

Bulk Heterojuction

In a bulk heterojunction, the electron donor and acceptor materials are blended together and cast as a mixture which then phase separates. Typically, regions of each materials are separated only by several nm, a distance optimized for carrier diffusion. This enables short exciton ways to the interface and much thicker layers can be made to harvest more light. The first polymer bulk heterojunction was made by Yu [6] in 1994 by spin coating on ITO covered glass from a solution of MEH-PPV and C_{60} in a 10:1 wt-ratio. A photosensitivity of 5.5 mA/W was observed for this cell which was an order of magnitude higher than of the pure polymer. Major developments in the polymer fullerene bulk heterojunction photovoltaics were reported by Shaheen et al. [16] where for the first time efficiencies up to 2.5% were recorded.

However, in this architecture the problem comes with the connectivity to the correct electrode. To improve the electron and hole transport, a hole blocking layer and an electron blocking layer are introduced on either side between the active layer and the electrodes (Figure 1.3).

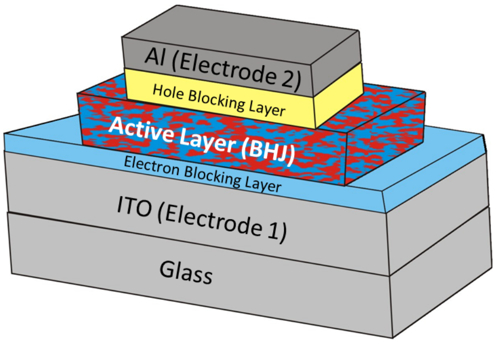

Figure 1.3: The bulk heterojuction architecture of the active layer

1.3 Degradation of Organic Solar Cells

Organic solar cells are not as well understood as compared to inorganic ones and present a complex selection of degradation phenomena. Some of these processes are reversible upon annealing while others decrease the cell efficiency irreversibly. When organic materials are exposed to sunlight they can react via photochemical reactions. These reactions are affected by the presence of other components in the atmosphere like oxygen and water and inevitably lead to the deterioration of the performance of the cell. The degradation of other layers also contribute to the overall deterioration of the performance which includes oxidation of the electrodes, diffusion of metals through the blocking layers etc (Figure 1.4). However, in the context of my thesis I will discuss only the degradation of the active layer material.

One of the most important reactions is the photo-degradation in the presence of oxygen. In 2009, Seeman et al. [18] reported studies on degradation of poly(3-hexylthiophene) (P3HT) : [6,6]-phenylC61butyric acid methyl ester (PCBM) solar cells by determining the changes in the I_{SC} and V_{OC}. They used gas permeable electrodes so that the active material gets exposed to light and oxygen simultaneously. The cells were kept in dark for the first 60 min and then exposed to light. IV characteristic curves were taken after 5, 10, 30, 60 and 120 min (Figure 1.5). In dark, the IV characterization in dry nitrogen environment as well as synthetic air showed only a little change. When the light was turned on, in

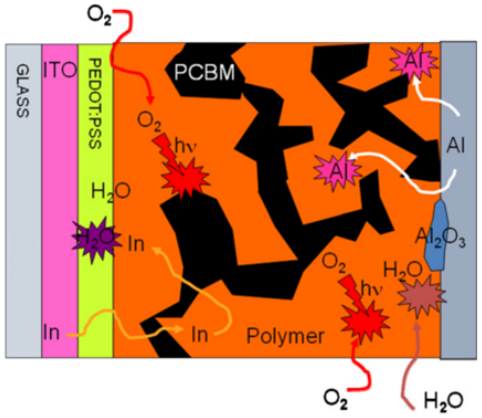

Figure 1.4: Cross section view of a solar cell device with typical degradation processes that can take place in a bulk heterojunction and lead to decrease in efficiency [17]

dry nitrogen environment, again only small changes were observed. However, in oxygen environment in the presence of light, a dramatic decrease in the performance parameters was observed. The short circuit current showed the maximum change by decreasing down to 50% of its original value. The open circuit voltage droped by 15% and the fill factor droped by 20% which resulted in a decrease in efficiency by 60%.

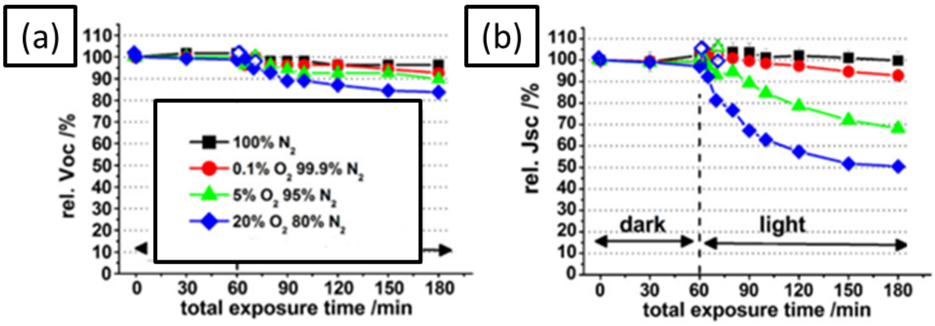

Figure 1.5: Relative changes in the performance parameters as a function of time in different environments of nitrogen and oxygen (a) open circuit voltage (b) short circuit current [19]

In early stages of degradation (for small oxygen concentrations and short illumination periods), the observed changes were reversible upon annealing. For longer illumination periods, significant irreversible changes were observed. These irreversible changes were attributed to photo-oxidation of the polymer and fullerene [19].

Reversible degradation

The reversible changes in the electrical properties of the solar cells have been attributed to (photo-) doping of the photoactive layer by oxygen. The doping process can be reversed by annealing the samples under nitrogen at sufficiently high temperatures. This doping process results in the formation of a charge-transfer-complex between the polymer and oxygen. Seeman et al. [19] summarized these processes in the following schematic (Figure 1.6). The diffusion coefficient of oxygen was given by Luer et al. [20] as $3\times10^{-8}\text{cm}^2\text{s}^{-1}$ from which we can estimate that 100 nm of active layer can be equilibrated with oxygen within milliseconds.

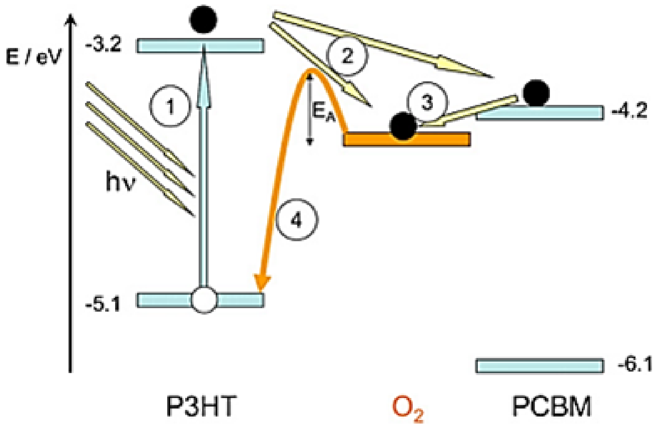

Figure 1.6: Oxygen doping in a P3HT:PCBM blend (1) Excitation of the electron in P3HT (2) Electron transfer to PCBM (3) Trapping of electron in oxygen (4) Recombination. E_A is the activation barrier for charge carrier recombination [19]

Charge extraction through linearly increasing voltage (CELIV) measurements also showed an increase in the concentration of free charge carriers [19, 21]. The doping process in the dark was quite slow and led to an increase in charge carrier concentration by 30% within 60 mins. The charge carrier concentration increased by an order of magnitute on illumination of the sample which increased the formation of mobile charge carriers (Figure 1.7).

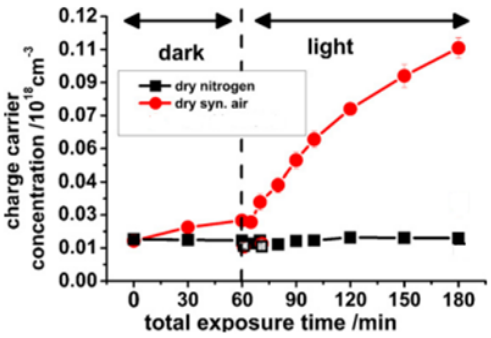

Figure 1.7: Increase in charge carrier concentration observed from CELIV measurements [19]

Irreversible degradation

The irreversible part of the degradation is assigned to photo-chemical oxidation and finally fragmentation of the molecules. In 2009, Manceau et al. [22] explained the mechanism of photo-oxidation of P3HT. They took thin films of regioregular P3HT and exposed them to UV-visible light irradiation in the presence of air. The samples were characterized by infrared (IR) spectroscopy and the oxidation products were identified. They claimed that the degradation involved a radical oxidation of the hexyl side-chains and then the thiophene rings. The bleaching of the sample was attributed to the breaking of the molecular backbone which resulted in a loss of π-conjugation.

In addition, it was found that the main products of degradation could be classified into carbonyl and sulfur containing moieties (Figure 1.8). They claimed that the oxygen attacks the alkyl side chain at the carbon atom which was in the α-position of the thiophene ring. This attack led to a hydrogen abstraction and the formation of a microalkyl radical. After this step, the formation of α-unsaturated hydroperoxides was observed which then decomposed yielding alkoxy and hydroxy radicals.

Oxidation of the backbone results from oxidation of the sulfur atom of the thiophene ring which changes into sulfinate esters (Figure 1.9). The formation of the esters are characteristic for ring opening and chain scissions. Due to these

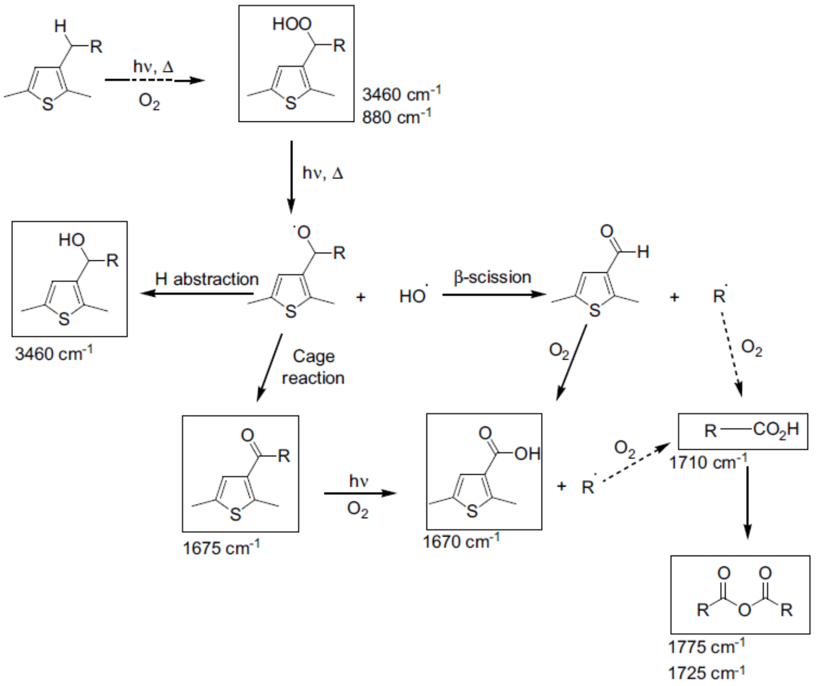

Figure 1.8: Oxidation mechanism of the P3HT alkyl chain [22]

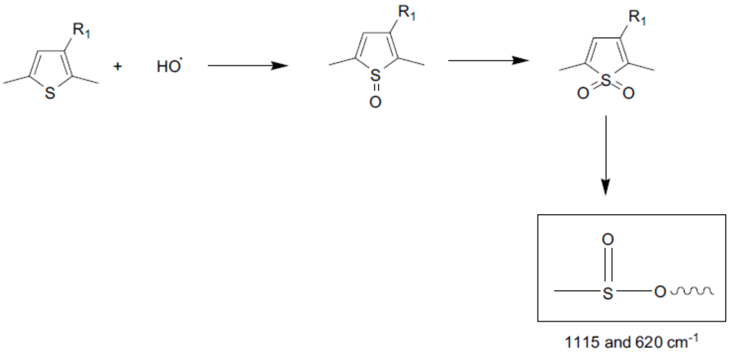

Figure 1.9: Oxidation mechanism of the sulfur atom of the thiophene ring [22]

processes a collapse of the layer is expected.

Several studies have also been done on the oxidation of fullerenes. In 1994, Juha et al. [23] observed the formation of fullerene-oxygen adducts when fullerene samples were exposed to oxygen and ultraviolet or visible light. These adducts were said to have an epoxide structure. Spectroscopic analysis by Creegan et al. [24] also supported this epoxide structure (Figure 1.10). Taliani et al. [25]

described the photo-oxidation of fullerene which gave rise to $C_{60}O_2$ and $C_{60}O_4$. In this process, one of the C=C bonds of the C_{60} was broken via a reaction with electronically excited molecular oxygen and addition of oxygen takes place. Therefore, photo-oxidation of fullerene should lead to an increase in the size of the molecule which in turn should lead to an increase in the thickness of the active layer.

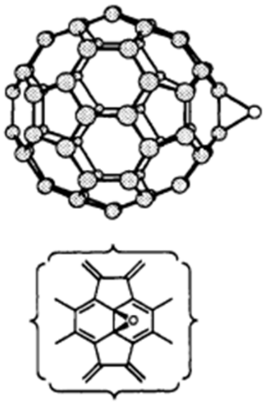

1

Figure 1.10: Photo-oxidation of C_{60} leads to an epoxide structure by breaking of C=C bonds and addition of oxygen [24]

Scanning probe microscopy (SPM) is an ideal tool to probe the nanoscale morphology and also the various processes taking place in these organic photovoltaics. Since its invention in the 1980s with the scanning tunneling microscopy (STM), this tool has played a fundamental role in the development of nanotechnology. Soon after, the invention of the STM, which could only be applied to conducting samples, the field of application was extended to non-conducting samples with the invention of the **Atomic Force Microscopy (AFM)**. These AFM methods can be applied to samples in various environments like vacuum, air and liquids. Several groups have used these AFM methods to characterize solar cell materials. The most common studies have been on changes in morphology when these materials are annealed [26, 27] or the effect of polymer molecular weight on the morphology [28].

1.4 Motivation

AFM has also been used to study the degradation of solar cell materials. However, most of these studies have been limited to observing changes in morphology on degradation [17]. AFM has also been used to study the microscopic holes in the outer electrodes which create a channel for oxygen and water resulting in oxidation of the underlying organic material [17]. The changes in morphology on photo-oxidation occur only after long hours of degradation. Early stages of degradation involve changes in the open circuit current (V_{OC}) and short circuit current (I_{SC}) as discussed earlier. To study these kind of changes in the solar cell materials on degradation, we go to electrical modes of AFM.

The electrical modes of the AFM give information about the electrical properties of organic solar cells. A very common mode of characterization of electrical properties is the Kelvin probe force microscopy (KPFM) which maps the contact potential difference between the tip and the surface. In 2002, Yamada et al. [29] mapped the surface potential of molecular films of oligothiophene molecules deposited on platinum substrates using KPFM. In dark, a surface potential of 190 mV was observed on the film which they claimed was caused due to the charge transfer at the molecule-substrate interface. They also investigated photoinduced potential of the film under ultraviolet light shown in Figure. Conductive-AFM (c-AFM) was first used by Alexeev et al. [30] in 2006 for the characterization of polymer blends. Besides morphology, the internal structure was studied by measuring the current distribution with nanoscale spatial resolution. Nowadays it has become a common technique of characterization of electrical properties of organic photovoltaics [31, 32, 33]. To investigate photo-induced charging inside solar cells, Coffey et al. developed a method known as time-resolved electrostatic force microscopy (trEFM) [34]. Furthermore, they correlated the charge accumulation rates with the external quantum efficiencies (EQEs) as measured on completed devices.

The excellent lateral and height resolution of AFM and its ability to map electrical properties of photovoltaic materials make it a suitable choice for degradation studies of the individual components in the active layer blend and also the blend as a whole. However, up until now, very few studies using AFM have been made on degradation of organic photovoltaics [32, 35, 36] and its application has been limited to the characterization of the nanostructure of the materials in order to optimize the efficiency of the cells [17]. In the present work I will focus my studies on the degradation of organic photovoltaic materials with the use of AFM and its different electrical modes, namely, the KPFM and c-AFM. These methods have been used extensively in my studies to determine changes in the local surface potential and conductivity of the active layer upon photo-degradation. In addition to AFM, which is only surface sensitive and can only give us a speculation about the chemical reactions happening inside the active layer, complementary techniques like nuclear magnetic resonance (NMR) and UV-Vis spectroscopy have been used to gain specific chemical information on the degradation products. A more detailed description of all these methods is given in **Chapter 2: Experimental Methods** which includes the sample preparation and degradation as well.

The photo-oxidation of the active layer is one of the major causes of degradation of solar cell devices. Abad et al. [36] observed a decrease in the thickness of the active layer (consisting only of the donor material) when exposed to UV irradiation. The only explanation given for this decrease is the removal of the material. In my work I compared the changes in the thickness of thin layers of donor, acceptor and the blend as a whole when exposed to light in presence of oxygen **(Chapter 3: Photo-oxidation of P3HT:PCBM)**. Irradiating the active layer through a grid mask allowed us to do relative measurements between the degraded and the non-degraded areas within the same scan image. Together with NMR and UV-Vis spectroscopy studies, these experiments allowed us to identify the chemical reactions occuring inside the layer between the materials and the oxygen.

Photo-degradation not only changes the morphology of the active layer but also causes changes in the electrical properties. These changes start appearing much earlier than the morphological changes. The most common way to study this kind of degradation is to determine the open circuit voltage (V_{OC}) and the short circuit current (I_{SC}) for complete devices. The changes in the V_{OC} and I_{SC} arise from the changes in the energy levels of the molecules in the active material. The values measured with the KPFM can be correlated to V_{OC} and that of c-AFM to I_{SC}. In this way, we were directly able to study the various shifts in the energy levels and quantify the degradation of the active layer and the construction of the entire device was not required (**Chapter 4: Electrical modes of AFM**).

The above studies were followed with the investigations on new materials used in organic photovoltaics **(Chapter 5: Investigations of new low bandgap materials)**. These materials have a low optical bandgap and therefore are excellent candidates for light harvesting devices. Using our method described in the previous chapters we can very easily compare the stabilities of these materials to the earlier known materials. The materials were partially received from Konarka GmbH as a part of a collaboration funded by the BMBF (contract 03SF0334).

Up until now, I have discussed steady state measurements, where KPFM or c-AFM images were taken in dark and then under illumination. These methods can't be used to probe dynamic processes like, charging rates and charge recombination, since their time resolution is not sufficient ($\geq$ 1ms). The technique of trEFM, developed by Coffey et al. [34], gives information on photogenerated carrier accumulation and surface potentials in a time resolved fashion. Having implemented this technique with our setup, I was able to determine changes in the charging rates of the individual donor and acceptor domains in the active layer blend with degradation. The measurements gave us direct information of the dynamic processes occuring at the nanoscale which can't be probed by any other technique. **(Chapter 6: Time resolved studies)**

Any changes in the AFM tip, like contamination of the tip, changes the values measured by KPFM or c-AFM. Therefore, it is very important to do relative measurements, e.g. partially degraded samples (chapter 3 - chapter 5). Another approach would be to use different environments like vacuum or liquid instead of air which has a lot of unknown impurities. Measurements in liquids ensures the removal of water and other organic adsorbates from the surface thereby reducing shielding effects. This motivated us to start exploring the electrical modes of AFM in liquids. We used an electrically insulating and non-polar liquid (decane) which allowed us to perform standard KPFM without the risk of spurious forces acting on the tip. As a proof of principle, we investigated the work function change of an Au substrate upon hexadecanethiol adsorption from decane. **(Chapter 7: KPFM in liquids)** Establishment of this method will enable us to do insitu measurements of the modification of the work function of electrodes which is attractive for opto-electronic devices since there is a better alignment of the energy levels.

2

Experimental methods

2.1 Scanning Probe Microscopy

Scanning probe microscopy (SPM) is a powerful tool to characterize the surface of a material with nanoscale resolution. This technique was founded with the invention of the scanning tunneling microscopy (STM) in 1981 by Gerd Binnig, Heinrich Rohrer, Christoph Gerber and Edmund Weibel at the IBM Zurich Research Laboratory, Switzerland [37] In STM, a tip is moved above a sample surface and the tunneling current is measured between them. Any changes in the tip-sample distance caused by changes in the sample height results in changes in the tunneling current. The height of the tip above the sample is kept constant by maintaining a constant current. However, this techniue can only be used for electrically conducting samples. In 1986, Gerd Binnig and Heinrich Rohrer received the Nobel prize in physics for their work using this technique.

The next development was made by Gerd Binnig along with Calvin Quate and Christoph Gerber with the Atomic Force Microscopy (AFM) [38]. This technique uses the concept of a probe scanning over the sample surface, much like a finger being run over a surface to feel its properties. The feedback loop works based on the forces acting between the tip and the sample surface and therefore works even for electrically insulating samples. Preliminary results using AFM in air gave a lateral resolution of 30 Å and a vertical resolution of less than 1 Å. In contrast to optical microscopy methods which provide just an image of the surface, this technique can be used to determine mechanical, thermal as well as electrical properties of the surface.

Basic Principles

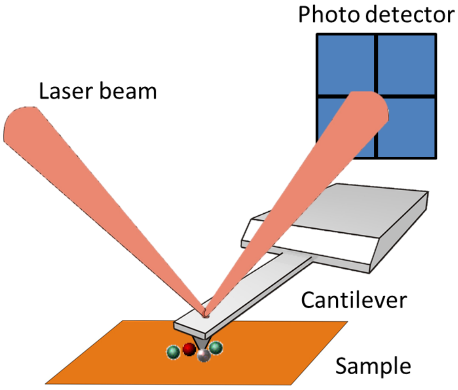

Figure 2.1: The basic AFM setup

An atomic force microscope consists of an atomic sharp tip mounted on a cantilever which is scanned across the surface in the x-y plane (Figure 2.1). The cantilever is typically made of silicon or silicon nitride and the tip apex lies in the range of 5-50 nm. A laser beam is focussed on the backside of the cantilever which gets reflected into a photodiode. Any movement of the cantilever is detected by changes in the spot position of the laser on the photodiode which is divided into four quadrants. When the tip is brought close to the sample surface, it experiences forces (such as van der Waals forces, electrostatic forces) which lead to a deflection of the cantilever. For small cantilever deflections (Δz), the cantilever can be considered to be a spring following the Hooke's law, where the force is given by

$$F = -k\Delta z \tag{2.1}$$

where k is the spring constant of the cantilever.

The atomic force microscope can be operated in a number of modes, depending on the application. The basic imaging modes are divided into static (also called contact) mode and the dynamic (also called the intermittent or tapping) mode. These modes are categorized based on the interaction of the AFM tip with the sample surface depending on the tip-sample distance. This interaction having both repulsive and attractive parts is described by the Lennard-Jones potential (Figure 2.2)

$$U_{LJ} = [\frac{A}{r^{12}} - \frac{B}{r^{6}}] \tag{2.2}$$

where r is the distance between the tip and the sample, A and B are constants. The repulsive part is described by r^{-12} and arises due to the overlapping of the electron orbitals and the attractive forces is described by the r^{-6} term and comprises of the short range van der Waals forces. The following section describes these modes in further detail.

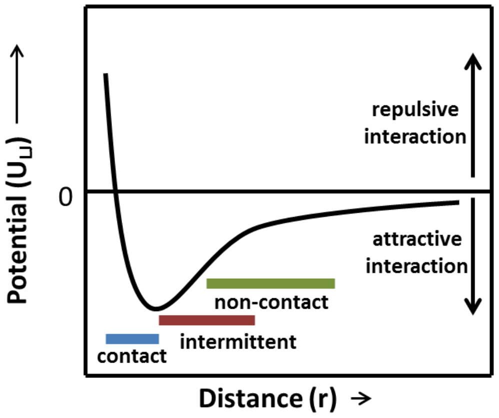

Figure 2.2: Schematic of Lennard-Jones potential describing the tip-sample interaction with distance between tip and sample

Imaging modes

In the **contact mode**, the deflection of the cantilever is used as a feedback signal. As the tip scans over the surface with feedback on, the distance of the cantilever to the surface is adjusted such that the deflection of the cantilever remains constant. The value of the constant deflection is chosen by the user and is known as the set point. The z piezo moves the back end of the cantilever up or down and the calibrated z piezo position is recorded as the height data. If the deflection signal is higher than the set point, the z voltage is decreased which moves the tip away from the surface. Similarly, to get the tip in contact with the surface the z voltage should be increased.

However, this mode has a few drawbacks. Since the tip is always in contact with the sample surface, both the tip and the sample surface may get damaged during scanning. It is even worse for imaging soft samples than hard samples, where even low forces (nN) can cause deformations on the surface.

To overcome wear of surface and/or tip , the **intermittent mode** of imaging can be used. The basic setup stays the same consisting of a cantilever with a tip, the sample on an xyz stage moved by a piezo and the detection system with a laser and a position sensitive photo detector. In addition, there is a piezo element driving the cantilever also. In this mode, the cantilever is vibrated near or at its resonance frequency. This movement of the cantilever results in oscillations of the deflection signal as well. The amplitude as well as the frequency of the oscillation changes as it moves over the sample surface depending on the topography of the sample and other interactive forces between the tip and the sample. The equation of motion of the cantilever is given by considering it to be a spring :

$$m\ddot{z} + \frac{m\omega_o}{Q}\dot{z} + kz = F_{ts} + F_o cos(\omega_d t) \tag{2.3}$$

where k is the spring constant, Q is the quality factor, F_{ts} is the tip-sample interaction, F_o and ω_d are the amplitude and angular frequency of the driving force.

A change in the tip sample distance leads to a change in the force gradient, which shifts the resonance peak as well. The change in the force gradient results in a change of the oscillation amplitude at the driving frequency. A feedback loop is used to maintain a constant amplitude by adjusting the tip-sample distance. This kind of imaging mode is known as the amplitude modulation (AM) mode and is usually applied in air, where the quality factor of the cantilever is of the order of 1-100.

In vacuum, the quality factor increases drastically due to the reduced damping which results in a very slow response time of the system. In this case, the frequency modulation (FM) mode is used which was introduced by Albrecht et al. [39]. Here, the change in resonance frequency is directly measured. Through an automatic gain control (AGC) the oscillation amplitude is kept constant and the resonance frequency is measured using a frequency demodulator. A constant frequency shift with respect to the free resonance frequency is maintained by adjusting the tip-sample distance.

2.1.1 Kelvin Probe Force Microscopy

A combination of AFM with the Kelvin probe technique [40] gives the Kelvin Probe Force Microscopy (KPFM). In the Kelvin probe technique, the contact potential difference of the sample is measured by assuming the sample to be one plate of a parallel plate capacitor with a known metal forming the other plate. The latter is vibrated at a frequency ω. Due to the changing distance between the plates, the capacitance changes, resulting in an alternating current in the circuit. This current is nullified by applying a DC-voltage to one of the plates. The voltage applied corresponds to the contact potential difference (CPD) of the two materials.

KPFM was first developed by Nonnenmacher, O'Boyle and Wickramashinge in 1991 [41]. In this method, the CPD between a reference tip and the sample is measured with high spatial resolution. It employs the same principle as the Kelvin probe technique by applying a DC-voltage to compensate the CPD between the tip and the sample. However, in this method, instead of nullifying the current, the electrostatic force between the tip and the sample is used as a controlling parameter. High sensitivity of the CPD measurement is achieved as the cantilever is very sensitive to forces acting on it.

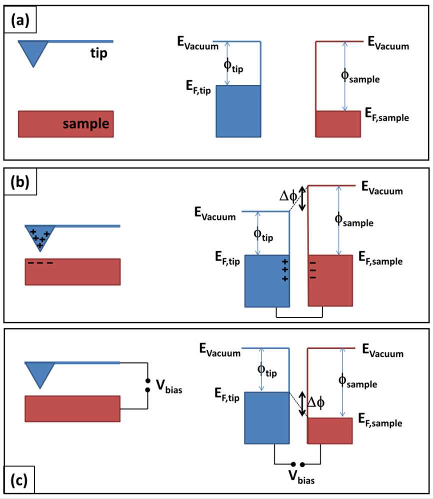

Figure 2.3: Schematic of the tip sample interaction and the corresponding energy levels. (a) tip and sample are separated, (b) tip and sample are electrically connected, (c) on applying additional external DC potential

Working Principle

The conducting tip and the sample having different work functions (given by ϕ_{tip} and ϕ_{sample}) are placed near each other (Figure 2.3a). When both elements are brought in contact, a net electric current flows between them until the Fermi levels are aligned (Figure 2.3b). This alignment results in the contact potential difference (V_{CPD}) which equals to the difference in the work functions of the tip and sample ($\Delta\phi$). A bias voltage is applied to the cantilever which consists of an alternating AC-voltage $V_{ac}\sin(\omega t)$ and a constant DC-voltage V_{dc}. Due to the resulting oscillating electrostatic force, the cantilever starts oscillating at the frequency ω. This electrostatic force can be expressed as:

$$F = -\frac{1}{2}\frac{dC}{dz}[V_{dc} - V_{CPD} + V_{ac} sin(\omega_{ac} t)]^2 \tag{2.4}$$

Here, V$_{CPD}$ is the work function difference between the sample and the tip, given by :

$$V_{CPD} = \frac{\Delta\phi}{e} = \frac{(\phi_{tip} - \phi_{sample})}{e} \tag{2.5}$$

Separating the frequency components of equation (2.4), we get

$$F_{dc} = -\frac{dC}{dz}[\frac{1}{2}(V_{dc} - V_{CPD})^2 + \frac{V_{ac}^2}{4}] \tag{2.6}$$

$$F_{\omega_{ac}} = -\frac{dc}{dz}(V_{dc} - V_{CPD})V_{ac}sin(\omega_{ac}t) \tag{2.7}$$

$$F_{2\omega_{ac}} = \frac{dC}{dz}\frac{V_{ac}^2}{4}cos(2\omega_{ac}t) \tag{2.8}$$

The $F_{\omega_{ac}}$ component becomes zero when $V_{dc} - V_{CPD} = 0$. A lockin amplifier is used to detect the cantilever oscillation at ω and the V_{dc} is adjusted such that the electrostatic forces between the tip and the sample become zero. This value of V_{dc} is equal to the V_{CPD}.

From equation (2.5), the absolute work function of the sample can be calculated if the work function of the tip is known. However, the work function of the tip may change during scanning due to contamination of the tip. Therefore, it is very important to have a known reference within the scan area to get reliable values.

Similar to the topography measurements, there are two modes for the KPFM too. In the amplitude modulation technique (AM-mode), a zero amplitude of the cantilever oscillation is maintained by adjusting the V_{dc} to match the V_{CPD}. In the frequency modulation technique (FM-mode), the change in the oscillation frequency induced by the tip-sample interaction is monitored and is minimized by adjusting the V_{dc}. In the FM-mode, the change in the frequency is proportional to the force gradient and is therefore much more sensitive than the AM-mode. We used the dual pass (or lift mode) KPFM in which the topography is recorded in intermittent contact mode during the first pass. Then the mechanical excitation is switched off and the tip is lifted up (typically 10-100 nm) above the surface. It then follows the topography and determines the surface potential in the second pass.

KPFM on Organic Photovoltaics

The KPFM measurements do not require a direct contact between the tip and the sample [42]. Therefore, fragile and soft samples like organic materials can be well studied with this method. KPFM allows the study of surface potential distributions on thin films of organic materials even if the samples have poor conductive properties. Also, it does not require any kind of sample treatment which may change any sample properties.

After the first study of surface potential on organic solar cells using KPFM by Yamada et al. [29], several groups have used KPFM to study the effect of illumination on the surface potential of these organic materials. Under illumination, the working conditions of a solar cell can be simulated. Spadafora et al. [43] could spatially resolve the surface photovoltage in high efficiency photovoltaic blends of poly(3-hexylthiophene)(P3HT) and [6,6]-phenylC61butyric acid methyl ester (PCBM) using KPFM in UHV conditions. They were able to directly visualize the charge generation at the donor-acceptor interfaces and their transport through the percolation pathways in the nanometer range. Several studies have also been done in ambient conditions. Hoppe et al. studied organic solar cell systems consisting of MDMO-PPV:PCBM blends using KPFM in dark and under illumination with a 442 nm cw laser. They reported that toluene-cast blends have lower power conversion efficiencies as compared to chlorobenzene-cast blends and related this effect strongly to the nanomorphology in the bulk heterojunction. Maturova et al. [44] did KPFM on phase separated active layer of MDMO-PPV:PCBM bulk heterojunction solar cells in the dark and under illumination and reported a significant density of free photogenerated electrons in both the donor and acceptor rich phases.

Degradation of conjugated polymer solar cells have also been studied using KPFM. The local photooxidation and trap formation in all-polymer bulk heterojunction organic photovoltaics were studied by Reid et al. [45] using the conventional KPFM and time-resolved electrostatic force microscopy (trEFM). The latter method was used to determine charging rates of organic materials. They compared the local photovoltage shifts measured via KPFM and the changes in local photoinduced charging rates measured via trEFM. The details of trEFM will be explained in detail in chapter 6.

2.1.2 Conductive Atomic Force Microscopy

Another electrical mode frequently used to study organic photovoltaics is the conductive atomic force microscopy (c-AFM). In this mode, a conductive tip is scanned in contact with the sample surface (Figure 2.4). A voltage is applied between the tip and the sample which generates a current flow between the tip and the sample which is recorded as a current image. A topographic image is recorded simultaneously using a feedback loop which maintains a constant tip deflection. This method is in contrast to scanning tunnelling microscopy where a constant current is adjusted by the feedback control. This difference makes c-AFM more attractive to study heterogeneous materials such as conductive-non-conductive composites without the tip crashing into the non-conductive areas of the sample. Typical current values are recorded in the 1 pA to 1 nA range.

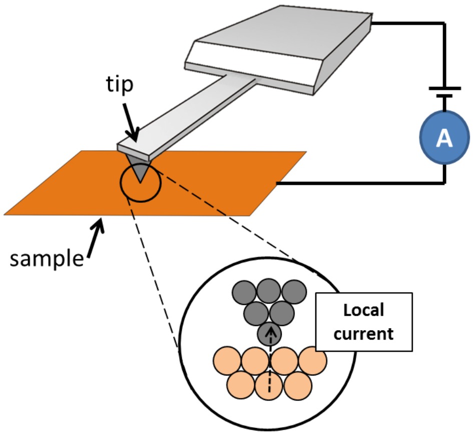

Figure 2.4: Schematic of conductive atomic force microscopy

This mode was first reported by Murrell et al [46] in 1993 where they investigated the dielectric strength of SiO_2 gate oxide films with a lateral resolution better than 20 nm.

As in the case of KPFM, the tip characteristics also play a major role in the current images that are produced. The amount of current flowing between the tip and the sample depends on the area of contact. If the tip is sharp, the contact area is very small and the amount of current flowing will be less (Figure 2.5a). While scanning in contact mode, the tip might undergo changes like broadening (Figure 2.5b) which results in a larger contact area between the tip and the sample which results in a higher current flow. Therefore, it is very necessary to have reference areas within the same scan image while doing c-AFM.

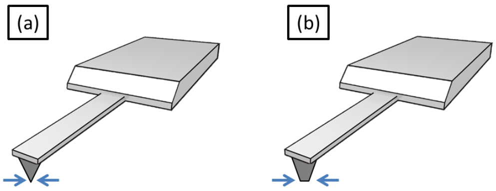

Figure 2.5: (a) Sharp tip allows a small amount of current flow between tip and sample (b) Broadening of the tip by constant scanning or contamination results in larger current flow

c-AFM on Organic Photovoltaics

c-AFM has been used to study the local conductivity of organic films since the late 90s [31, 47, 48, 49]. The first time the local electrical characteristics of a donar-acceptor blend were studied with c-AFM by Alexeev et al. in 2006 [30]. In 2007, Coffey et al. [32] used c-AFM to map the local photocurrents with 20 nm resolution in donor/acceptor blend solar cells of MDMO-PPV:PCBM spin coated from various solvents. They measured photocurrent maps under short-circuit conditions and for different applied voltages. Figure 2.6 shows their results obtained from MDMO-PPV:PCBM (1:4) spin coated from xylene. The photocurrent map measured with zero external bias under illumination is shown in Figure 2.6b. They acquired local current-voltage data for three locations marked in the image with and without illumination (Figure 2.6c).

In 2008, Leever et al. [50] developed an atomic force photovoltaic microscopy (AFPM) technique (based on c-AFM) to characterize spatially localized inhomogeneities in organic photovoltaic devices. In this technique they used a biased

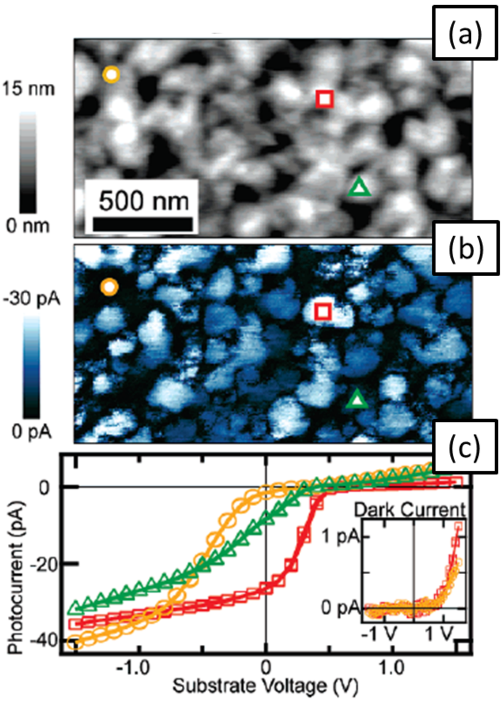

Figure 2.6: (a) Topography of MDMO-PPV:PCBM film spin coated from xylene (b) Photocurrent map measured with 0 bias under illumination at 532 nm (c) local IV characteristics at three points on the film [32]

c-AFM tip to raster scan over an array of illuminated solar cells, thereby, simultaneously generating topographic and photocurrent maps. In 2010, Dang et al. [51] performed photoconductive AFM (pcAFM) to study the nanoscale morphology and optoelectronic properties of bulk heterojunction based on small molecules which were reported to have had efficiencies 4.4%. The electron and hole collection networks were visualized for blends having different mixing ratios.

2.2 Nuclear Magnetic Resonance Spectroscopy

Nuclear magnetic resonance (NMR) was first described and measured in molecular beams by Isidor Rabi in 1938 for which he was awarded the Nobel prize in 1944. This technique was expanded for uses in liquids and solids by Felix Bloch and Edward Mills Purcell in 1946.

2.2.1 Basic Principle

NMR spectroscopy is a technique to obtain physical, chemical and structural information about molecules from the magnetic properties of certain atomic nuclei inside them. Most frequently this technique is used to investigate the properties of organic molecules and is applicable to any kind of sample that contains nuclei possessing spin. To understand this technique, we first start with the spin of a nuclei.

All nucleons in an atomic nucleus have an intrinsic quantum property called spin and the overall spin of the nucleus is given by the spin quantum number S. A nucleus having a non-zero spin is associated with a non-zero magnetic moment (μ) which is associated with S as $\mu = \gamma \cdot S$. Here, γ is called the gyromagnetic ratio. Only nuclei having an odd number of nucleons exhibit an NMR absorption spectra. Such a nucleus has two possible spin states : $m = \frac{1}{2}$ or $m = -\frac{1}{2}$. These states are degenerate, i.e. they have the same energy. When placed in a magnetic field, the degeneracy of the states is removed (Figure 2.7). The energy of a state is given by

$$E = -\mu \cdot B_0 \tag{2.9}$$

where μ is the magnetic moment and B_0 is the external magnetic field. The difference in energy between the two levels is therefore,

$$\Delta E = -\gamma h B_0 / 2\pi \tag{2.10}$$

When electromagnetic radiation is applied such that it matches the energy difference between the nuclear spin levels in a constant magnetic field, resonant absorption takes place. Hence, a magnetic resonance absorption will occur only when $\Delta E = h\upsilon_0$ where $\upsilon_0 = \gamma B_0 / 2\pi$. Such magnetic resonance frequencies typically correspond to the radio frequency range of the electromagnetic spectrum for magnetic fields upto 20 T. For a constant magnetic field, different nuclei have different energy splitting values. Figure 2.7b, shows the frequencies of different nuclei when kept in an external magnetic field of 2.35 T. The magnitude of

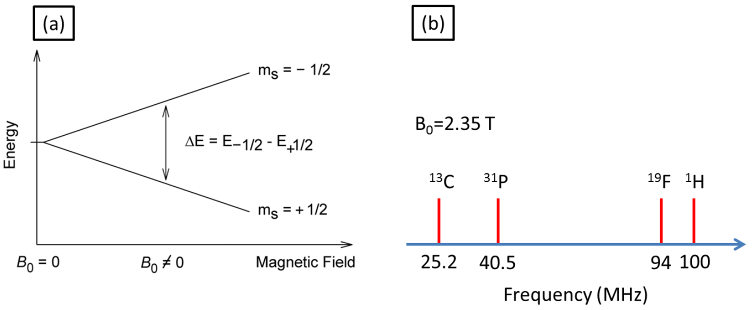

Figure 2.7: (a) Splitting of the energy levels when a nucleus is placed in a magnetic field (b) The approximate frequencies that correspond to the spin state energy separations for each nuclei when kept in a magnetic field of 2.35 T

these resonance signals is displayed along the vertical axis of the spectrum and is proportional to the molar concentration of the sample.

The most commonly used form of NMR spectroscopy is the ^{1}H proton NMR spectroscopy. Radio frequency of appropriate wavelength is incident on the sample to excite the protons in the sample. The signal caused by a proton is different for each sample in the same magnetic field range due to the effect of the atoms surrounding the ^{1}H and the kind of bonding they have. The proton spectra from different compounds is shown in Figure 2.8. This type of NMR spectroscopy is very useful for determining structures of organic compounds.

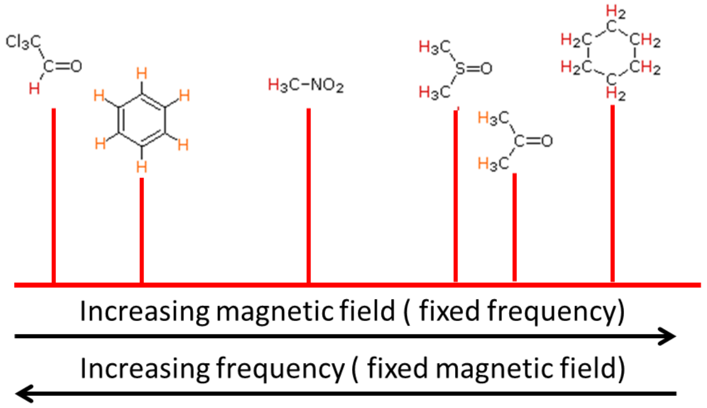

Figure 2.8: ^{1}H resonance signals from various compounds

Another form of NMR spectroscopy which is commonly used for organic compounds is the ^{13}Carbon NMR spectroscopy. This is used when significant portions of the molecule do not have C-H bonds. However, the presence of ^{13}C is very low (1.1%), so higher sample concentrations are required.

2.2.2 Solid state NMR

NMR spectroscopy characterized by the presence of directionally dependent (anisotropic) interactions is known as solid state NMR. The anisotropic interactions modify the spin energy levels and therefore, result in a line broadening effect of the NMR spectra. Originally, solid state NMR focussed only upon the measurement of ^{1}H spin-lattice relaxation times as a function of temperature in order to investigate methyle group rotations. To improve the resolution in solids, magic angle spinning (MAS) was introduced by E.R. Andrew and I.J.Lowe. They simulated artificial motion on the solid by spinning the sample which was finely powdered and packed tightly into rotors (at a frequency of 1 to 70 kHz) at the magic angle (approx. 54.74°) with respect to the direction of the magnetic field. Other methods to improve the resolution are dilution, multiple-pulse sequences and cross polarization. In cross polarization, polarization from abundant spins such as ^{1}H or ^{19}F is transferred to dilute spins such as ^{13}C. The overall effect enhances the signal to noise ratio.

2.2.3 NMR studies on organic photovoltaics

Solid state NMR spectroscopy has been used to characterize organic solar cells by measuring the nanoscale structure of the polymer blends. In 2006, Yang et al. [52] did NMR spectroscopy on regioregular P3HT and PCBM (Figure 2.9). They inferred the local structure within the interface from the chemical shift data which was obtained from composite films fabricated at room temperature. They reported that in the composite films, the long alkyl chains of rrP3HT are close to and wrap the C_{60} ball in the interfaces with the bicontinuous interpenetrating network. However, in the annealed films, the alkyl side chains of rrP3HT self-assemble in a way that the rrP3HT and PCBM molecules are separated from each other.

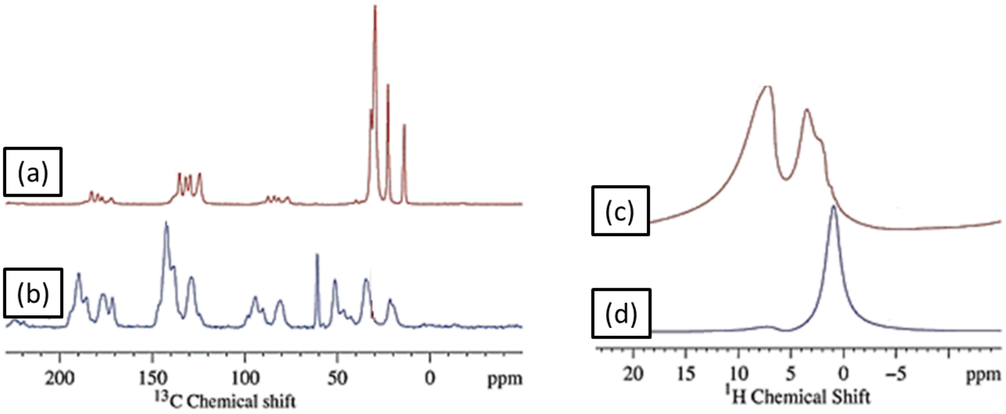

Figure 2.9: 1D ^{13}C NMR spectra of (a) P3HT (b) PCBM and 1D ^{1}H spectra of (c) PCBM and (d) P3HT [52]

More recently studies have been performed on small band gap polymer Poly[2,1,3-benzothiadiazole-4,7-diyl[4,4-bis(2-ethylhexyl)-4H-cyclopenta[2,1-b:3,4-b']dithio phene -2,6-diyl]] (PCPDTBT) and PCBM to provide insights into the local order and packing arrangements of the functional organic materials inside [53]. They reported the influence of additives on the morphology of the blend materials. On using additives, larger polymer rich domains were formed which resulted in the occurence of diffusion-limited exciton dissociation. The increase in the domain size was proven by 2D ^{13}C solid state NMR spectroscopy.

2.3 UV-Vis spectroscopy

Spectroscopic techniques that measure the absorption of radiation as a function of frequency are often used to characterize photovoltaic materials. The absorption spectrum for a material is the fraction of incident radiation absorbed by the material over a range of frequencies. It is used to determine the presence of a particular substance in a sample or to quantify the amount of the substance present. Infrared and ultraviolet-visible (UV-Vis) spectroscopy are particularly common in analytical applications.

Other than being used for determining the absorption spectrum for newly designed organic photovoltaic materials for the purpose of increasing efficiency, this technique is useful for mapping the relative material stabilities by measuring the loss of absorption caused by degradation. A common feature of all coloured compounds is a system of extensively conjugated π electrons. On photo-oxidation of active organic photovoltaic materials, there is a loss in conjugation which destroys the chromophores responsible for the colour and hence reduces absorption. This phenomenon is also called photo-bleaching.

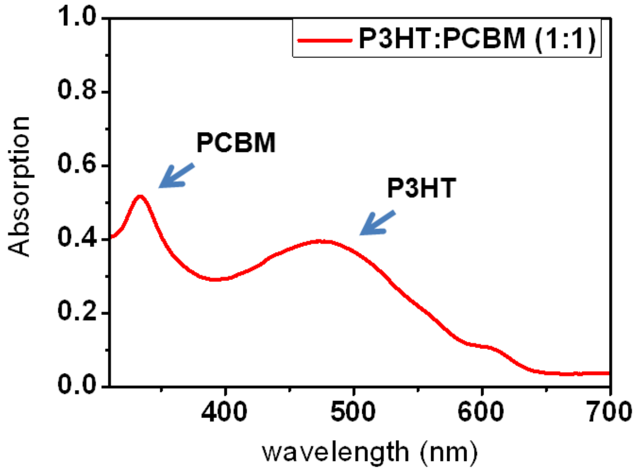

Figure 2.10: The UV-Vis spectra of P3HT:PCBM with absorption peaks at 330 nm (for PCBM) and 470 nm (for P3HT)

For the materials used in photovoltaics, the absorption spectrum lies in the UV-Vis region. In the P3HT:PCBM blends, light is absorbed due to the excitation of electrons from the HOMO level to the LUMO level of the conjugated π system. This happens when the wavelength of the incident light equals the energy gap between the HOMO and the LUMO levels. A typical absorption spectrum of P3HT:PCBM has absorption peaks at 330 nm and 470 nm for the PCBM and P3HT respectively (Figure 2.10).

Several groups have investigated the degradation of organic photovoltaics by UV-Vis spectroscopy. Hintz et al. [54] determined the decay kinetics of photo-oxidation and photo-ozonization of P3HT. They observed that on exposing thin

P3HT layers to photo-oxidative conditions, a decay of the optical absorption in the range of 330-650 nm is seen. This decay shows several distinctive differences between exposure to photo-oxidative conditions and ozone conditions. From their results it can be concluded that this method is very useful for following different degradation mechanisms.

2.4 Experimental Setup

2.4.1 Sample preparation

We used regioregular P3HT, PCPDTBT and Si-PCPDTBT as electron donors and PCBM as electron acceptor material. P3HT was used as received from Sigma-Aldrich: molecular weight MW = 15,000-45,000 g/mol, bromine end groups, electronic grade of 99.995%. PCPDTBT and Si-PCPDTBT were provided by Konarka Technology, Inc. (MW = 34,000 g/mol, PD = 2.0). PCBM was ordered from Sigma-Aldrich: electronic grade 99%. All solutions were prepared in a nitrogen glovebox. P3HT:PCBM was mixed in the ratio 1:1 and dissolved in o-dichlorobenzene (2% wt, Sigma-Aldrich), while PCPDTBT:PCBM was mixed in the ratio 1:3 and dissolved in o-dichlorobenzene (2% wt). Si-PCPDTBT:PCBM was mixed in the ratio 1:2 and dissolved in o-dichlorobenzene (2% wt). Pure P3HT and PCBM solutions were also made by dissolving them in o-dichlorobenzene (2% wt). These solutions were stirred overnight at 90°C and filtered with a Millipore filter with a pore size of 0.45 μm to remove the residual particles.

Thin films of the polymer/PCBM mixture, P3HT and PCBM, were obtained by spin-casting [55, 56] the solutions on glass substrates which were coated with 100 nm of ITO (99.9%, MaTeck GmbH). Spin-casting of the active layer was done at 500 rpm for 360 s inside the nitrogen glovebox. The films we obtained were around 100 nm thick as measured with a profilometer (KLA Tencor -16+). The samples were then thermally annealed at 140°C for 5 min inside the nitrogen glovebox.

2.4.2 Mask preparation

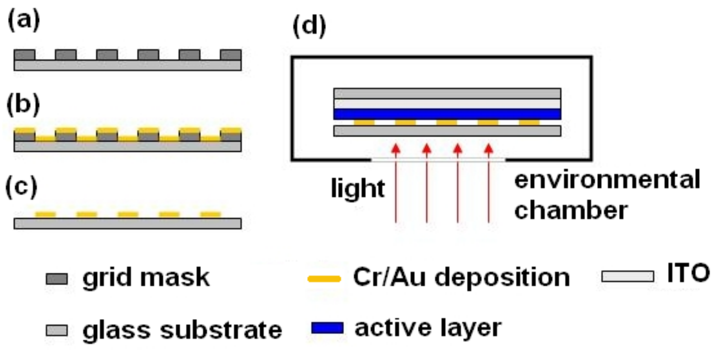

Figure 2.11: Schematic showing the preparation of the grid mask

The electrical modes of AFM are relative methods, i.e., the measured values such as surface potential or conductivity are not absolute. These parameters depend on the cantilever properties and hence it is very important to have an internal reference withing the scanning area. To obtain such an internal reference and to study the local degradation in the films, we prepared a micrometer-scale shadow mask. First, a transmission electron microscope (TEM) grid (Athene 400 mesh, diameter 3 mm, hole width 45 μm, bar width 10 μm) was placed on a UV transparent glass slide with a thickness of 0.5 mm (Heraeus Quarzglas GmbH & Co. KG, Hanau, Figure 2.11a). Then 5 nm of chromium followed by 150 nm of gold were evaporated (Figure 2.11b). Afterward, the TEM grid was removed from the top of the glass (Figure 2.11c), and the patterned glass was attached to the sample with the Au structures facing the film.

2.4.3 Degrading the samples

To degrade the samples, a solar simulator was used at AM 1.5 g (100 mW/cm^2, LOT). Accelerated degradation studies of P3HT:PCBM solar cells at higher light intensity have been studied by Tromholt et al. [57]. These authors reported a strong increase in the degradation rate at higher intensities. The degradation mechanisms, however, were shown to remain very similar to the nonaccelerated degradation for the P3HT:PCBM active layer. Furthermore, the accelerated degradation studies revealed that the adjacent electron transport layers of ZnO could significantly influence device performance owing to oxygen desorption and adsorption [58, 59]. In our studies, for longer degradation times, we illuminated our samples at 2 sun. The environment inside the chamber was changed for different samples to study the effect on the degradation. Four different environmental conditions were taken, i.e., (i) synthetic air (20.5% O_2, rest N_2, Westfalen AG) + 20% relative humidity (r.h.); (ii) synthetic air + 0% r.h.; (iii) pure nitrogen (99.999% N_2, 2 ppm O_2) + 80% r.h.; and (iv) pure nitrogen + 0% r.h. A maximum temperature of 40°C was measured by the temperature sensor in the chamber during illumination.

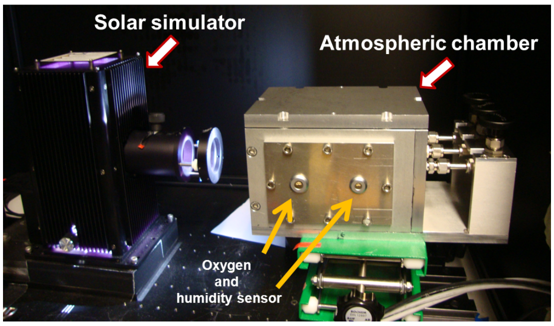

Figure 2.12: For degradation of the samples, they were kept inside an atmospheric chamber where the amount of oxygen and humidity can be controlled. This setup is kept in front of a solar simulator (AM1.5 g, 100 mWcm^2, LOT)

2.4.4 AFM measurements

The surface potential and photoconductivity mapping was performed by Kelvin probe force microscopy (KPFM) and conductive scanning force microscopy (c-AFM) at room temperature. The standalone version of Molecular Force Probe 3D (MFP3D) from Asylum Research was placed inside an acrylic glass glovebox (type P10R180T2, GS Glovebox Systemtechnik GmbH). The box was flushed with dry N_2 to avoid degradation and contamination of the samples while measuring them. The oxygen and humidity sensors indicated an atmosphere with less than 0.1% humidity and less than 0.01% oxygen. The microscope was placed on an active vibration isolation table (Halcyonics Nano 30). To avoid acoustic noise, the whole setup was placed in an acoustic chamber. Furthermore, the whole setup was placed on a massive marble plate supported by foam concrete blocks to protect the experiments from vibrations of the building.

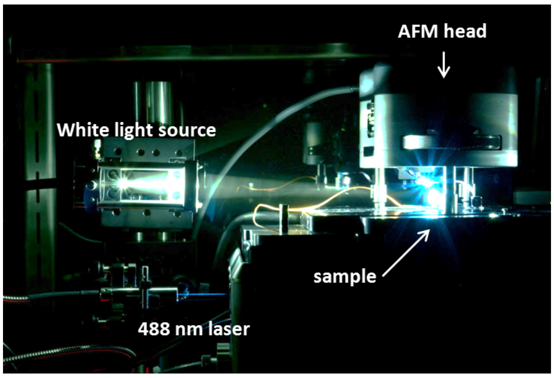

Figure 2.13: To generate photoinduced charge carriers, two light sources are assembled next to the atomic force microscope which illuminate the sample. The 488 nm laser beam is directed on the sample from underneath

Photoinduced charge carriers were generated by illuminating the samples with a diode laser light (wavelength 488 nm, Point Source, iFLEX2000) with a nominal output power of 15 mV coupled into a glass fiber. After the glass fiber, the laser light was directed on the sample having a spot diameter of 640 μm. At the sample position, the power of the laser was measured to be 13.3 mW (Newport Optical power meter, model no. 835 with a detector model no. 818-SL). All samples were transferred via an air lock into the glovebox. For KPFM measurements, we used a standard electrical holder (Asylum Research, Santa Barbara, USA). The samples were mounted on a holder with a hole in the middle to allow illumination from underneath. The samples were connected to the ground via a little drop of conductive silver paste (Sigma Aldrich, Steinheim). Pt-Ir-coated cantilevers were used for the analysis (nominal resonance frequency 70 kHz and 2 N/m spring constant, Nanosensors PPP-EFM). KPFM investigations were performed at a lift height of 20 nm [60].

For the c-AFM measurements, we used an ORCA holder (Asylum Research, Santa Barbara, USA) and Ti-Pt coated cantilevers (nominal resonance frequency 12 kHz and 0.15 N/m spring constant, μmasch CSC17/Ti-Pt). The measurements were performed in the contact mode at a normal force of 3 nN. At this normal force, we have not observed changes in surface topography after zooming out.

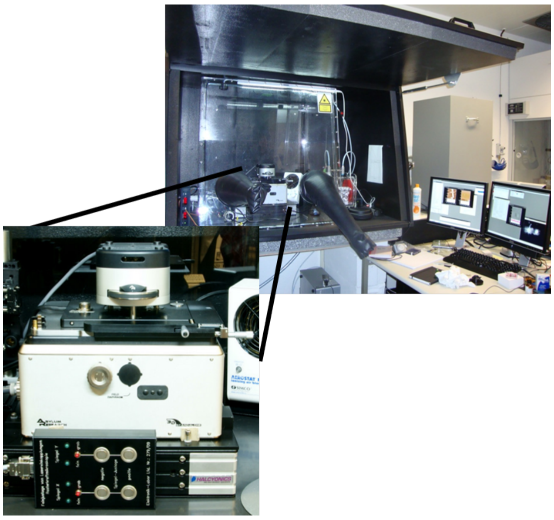

Figure 2.14: MFP3D in a glove box. To protect the experiment from noise, humidity and oxygen, the AFM is placed in an acrylic glove box inside an acoustic chamber. The air lock in the side is used to transfer additional equipment into the glove box. A zoom into the atomic force microscope shows that it is placed on an active vibration isolation table

Analysis of images

The KPFM and c-AFM images were analyzed by plotting histograms of the degraded and the non-degraded areas separately. A schematic of such a measurement analysis is shown exemplarily (Figure 2.15). Here, the degraded part is the area within the cross (orange) whereas the non-degraded part is the area outside the cross (blue). Histograms corresponding to the degraded and non-degraded areas have been plotted (Figure 2.15b). The average value of a histogram obtained from the potential/current values measured in the degraded and non-degraded areas were used in further calculations. The spread/distribution of values around this average value was a result of the inhomogeneities of the surface and also unequal degradation due to scattering near the edges of the grid mask. Another reason for such a distribution comes from the contribution of the different energy levels of the different materials present inside a blend.

For the c-AFM images, an offset current of 50 pA was added to all measured current values in order to account for the zero error of the instrument.

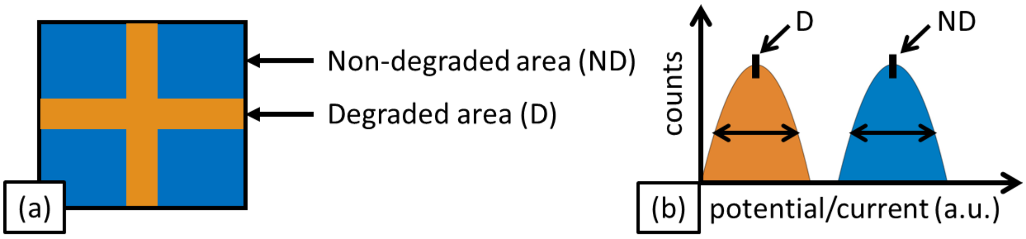

Figure 2.15: Histogram analysis of the KPFM and c-AFM images

2.4.5 UV-Vis measurements

A spectrophotometer consists of a light source, a monochromator and a detector. The light source is usually a xenon or deuterium arc lamp depending on the wavelength that is required. The beam of light from this source is passed through the sample and the detector, e.g. a CCD (charged-coupled device) or a photomultiplier is used to measure the intensity of the transmitted light.

The absorption spectra of the P3HT:PCBM blends coated on ITO glass substrates were investigated using a Perkin Elmer Lambda 900 UV/vis/NIR spectrophotometer in the wavelength range of 200-800 nm. At first, a background spectrum was measured with a clean glass substrate. This background spectrum was then subtracted from the absorbance spectrum of the sample. By doing this the absorbance due to air and the glass substrate was accounted for.

2.4.6 NMR measurements

Solid-state ^{1}H and ^{1}3C spectra were acquired on a Bruker DSX-500 spectrometer employing a Bruker 2.5 mm double resonance magic-angle spinning (MAS) probe. All spectra were recorded using a spinning frequency of 25.0 kHz. The single-pulse ^{1}H MAS NMR spectra were recorded using a $\pi/2$-pulse length of 2.5 μs and a recycle delay of 3 s for a total of 16 scans. The ^{13}C^{1}H cross-polarization (CP)/MAS NMR spectra were recorded at $\upsilon_L(^{13}\text{C}) = 125.77$ MHz with a CP contact time of 2.0 ms, a recycle delay of 3 s, and co-adding up to 50.000 scans. For some of the samples not enough of the blend material was available after degradation to fill the entire 2.5 mm rotor. In these cases we have used Teflon tape to fill the rotor to achieve stable spinning conditions. All spectra were referenced to TMS using adamantane as a secondary standard (δiso = 1.85 ppm for ^{1}H, δiso= 38.484 for ^{13}C) [61, 62]. Identical processing conditions were used for all spectra.

3

Photo-oxidation of P3HT:PCBM

3.1 Introduction

P3HT:PCBM is a well understood material system that acts as a model for polymer based solar cells (Figure 3.1). P3HT acts as an electron donor and PCBM as the acceptor. As stated in chapter 1, one of the main factors responsible for the degradation of the active layer is the combination of oxygen and light. Hintz et al. reported from their XPS studies that thiophene-based polymers become strongly p-doped upon interaction with O_2 and light [54]. As a result of this photo-oxidation, fragmentation of the polymers takes place [22] which ultimately results in the evaporation of the material. Abad et al. [36] observed a decrease in the thickness of the active layer made of donor material on photo-oxidation and attributed this to the afore mentioned evaporation.

Photo-oxidation of the PCBM results in incorporation of oxygen in the fullerene [63]. Studies have been performed on the photo-oxidation of C_{60} molecules previously by Xia et al. [64] where they have reported that interaction between oxygen and C_{60} molecules, induced by irradiation, may occur and can be described as

$$C_{60} \overset{light+O_2}{\rightarrow} C_{60}O_n + O_2, (n = 1 - 5) \tag{3.1}$$

Previous attempts at observing photo-oxidation of C_{60} furnished a single monox-

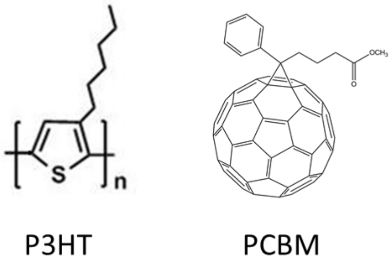

Figure 3.1: Molecular structure of P3HT (electron donor), PCBM (electron acceptor)

ide $C_{60}O$ having an epoxide structure [24, 65]. C_{60} has a diameter of 0.7 nm and oxidation results in an increase in diameter of 0.12 nm corresponding to a bond length of C=O (143 pm). Thus, after oxidation the diameter of C_{60} changes by 17% (Figure 3.2). Within a film, the photo-oxidation of C_{60} thus leads to an increase in thickness.

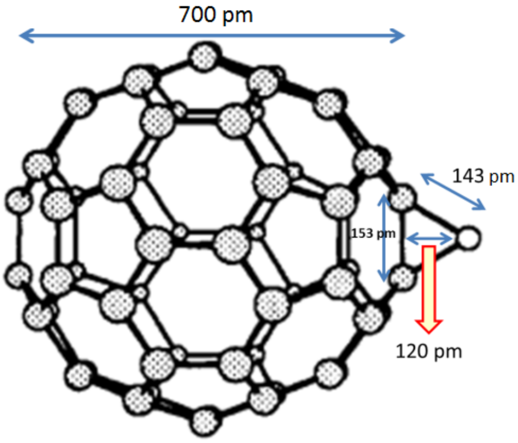

Figure 3.2: Photo-oxidation of C_{60} furnishes a single monooxide, $C_{60}O$ [24]

Accounting for the above effects, on one hand photo-oxidation of PCBM and on the other fragmentation of P3HT, we obtain two competing processes in a blend. The fragmentation of the polymer leads to a decrease in the film thickness whereas the photo-oxidation of the fullerene leads to swelling. Other studies on blends suggest that the fast electron transfer from the polymer to fullerene after excitation, accompanied by the formation of polarons on the polymer chain, decreases strongly the reactivity of the polymer against oxygen. This decrease occurs by quenching the triplet formation on the polymer and avoiding a triplet-triplet annihilation reaction with oxygen under formation of reactive singlet oxygen [66]. Lloyd et al. [67] reported that higher charge transfer rate between the donor and acceptor results in lesser photo bleaching and hence less degradation.

In the rest of the chapter, I will report our findings on how the thicknesses of thin layers of donor, acceptor and the blend change on photo-oxidation. From these observations, we were able to determine which process was dominant during the various stages of degradation. For a sample with the thickness of the order of a 100 nm, we expect thickness changes in the nm range. AFM is frequently used to investigate the change in the surface morphology at the nanoscale on degradation [68, 69, 70, 36]. Other groups have observed changes in layer thickness of the blend on photo-oxidation [45], however, it has not been investigated in detail.

3.2 Results and Discussion

Thin films of the donor, acceptor and the blend were taken and irradiated through the grid mask to obtain photo-oxidized and unoxidized parts on the sample surface. Using the AFM in tapping mode, we measured relative changes in the active layer topography between photo-oxidized and unoxidized parts (Figure 3.3). To study the effect of the amount of oxygen in the environment on the degradation of these materials, the samples were exposed to different concentrations of oxygen. Since AFM is only surface sensitive, from the above measurements we can only speculate about the chemical reactions happening inside the active layer.

To complement the AFM studies and gain chemical specific information on the degradation products for the individual components (P3HT and PCBM) and their blends, we have used solid-state NMR spectroscopy. This was done in collaboration with Christoph Kins and Michael Hanssen from the group of Prof. Spiess at MPIP. The chemical specificity relies on the fact that each NMR active isotope can be probed selectively due their different Larmor frequencies at high magnetic fields, and that the observed isotropic chemical shifts (δ_{iso}) are sensitive to the specific bonding environments of the nucleus [71]. In addition, the NMR resonance line width is sensitive to structural order/disorder of the different chemical moieties in the probed material, i.e., a narrow line width is indicative of order whereas a broad resonance point towards a disordered material [72, 73, 74]. Here, we utilize the broad δ_{iso} range of ^{13}C to follow the formation of different photo oxidation products related to oxygen and those of the conjugated polymer carbons, while changes in the aliphatic moieties were identified from ^{1}H and ^{13}C NMR spectroscopy [72]. To achieve a spectral resolution and sensitivity comparable to that obtained in liquid-state NMR, we have utilized magic-angle spinning (MAS) in combination with cross- polarization (CP) [75, 76]. These studies enabled us to follow the photo-oxidation at different stages of degradation allowing us to verify our afore mentioned speculations about the chemical reactions happening inside the active layer.

Calculation of photon dose

To compare the results from AFM and solid-state NMR, the degradation levels are indicated by the amount of photon dose the samples were exposed to. At 1 Sun intensity, the photon dose is given by

1 Sun = $100\times10^{-3}\ W/cm^2 = 0.1\ J/scm^2$

Therefore, photon dose for 1 hour

$= 0.1 \times 3600\ J/cm^2 = 360\ J/cm^2$

For the NMR studies, the samples were degraded to 20%, 50% and 80% decrease in the loss of absorption. In order to understand the loss in absorption, UV-Vis spectras were required. These values of absorption loss correspond to the following photon doses:

For P3HT,

50% loss in absorption ↔ 35 hours of illumination at 2 Sun (25.2 kJ/cm^2)

For PCBM,

50% loss in absorption ↔ 45 hours of illumination at 2 Sun (32.4 kJ/cm^2)

For P3HT:PCBM blends,

20% loss in absorption ↔ 12 hours of illumination at 2 Sun (8.64 kJ/cm^2)

50% loss in absorption ↔ 45 hours of illumination at 2 Sun (32.4 kJ/cm^2)

80% loss in absorption ↔ 92 hours of illumination at 2 Sun (66.24 kJ/cm^2)

3.2.1 Degradation of PCBM

In case of a pure PCBM layer, no change in the topography of the illuminated areas was observed compared to the non-illuminated ones in oxygen environment upto 20 hours. After 20 hours (14.4 kJ/cm^2) the thickness of the illuminated area increased relative to the non-illuminated one. The topography image of the partially degraded PCBM layer exhibited an increase of 16 ± 3 nm at a dose of 32 kJ/cm^2 (Figure 3.3). For illumination time of more than 45 hour, we did not observe any further changes in the thickness of the PCBM layer.

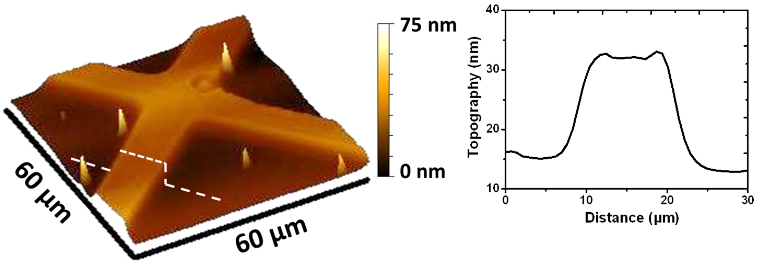

Figure 3.3: The AFM image of locally degraded PCBM layer after exposure for 45 hours at 2 Sun intensity in 20% oxygen. Changes in layer thickness between the degraded and the non degraded parts are observed. The increase in the layer thickness is measured by making a line profile through the image

Solid-state NMR studies on photo-degraded PCBM are summarized in Figure 3.4a and b, where the chemical changes are monitored at zero degradation (black) and after 25.2 kJ/cm^2 (orange) degradation using ^{1}H MAS and $^{13}C^{1}$H CP/MAS

NMR spectroscopy. From the ^{1}H MAS NMR spectrum of non-degraded PCBM (Figure 3.4a) two broad resonances are observed with intensity maxima at 3.2 and 8.0 ppm. These resonances can be assigned to the aliphatic and aromatic parts of the "handle" [77] for PCBM [78]. After photo degradation the aromatic signals display a strong intensity increase accompanied with a shift to lower frequency. Although the representation in Figure 3.4a might suggest a decrease in intensity for the aliphatic signals, these are in fact at approximately the same intensity level as before degradation. This fact is also apparent from a comparison of the ^{13}C^{1}H CP/MAS NMR spectra in Figure 3.4b, where the signals from the handle of PCBM have similar intensities before and after degradation (at 25.2 kJ/cm^2) . More importantly, Figure 3.4b gives evidence for the presence of significant amounts of carbonyl groups after degradation. These are predominantly located at lower chemical shift with respect to the carbonyl signal of non-degraded PCBM, where the resonances from sp^2-substituted acids (R-COOH) or (R_1-COO-R_2) appear [72]. Another important structural change is the intensity increase of the signal at ≈130 ppm. Signals located at this position are typically related to proton bearing carbons in extended aromatic systems [79, 80, 81]. Collectively, these chemical changes demonstrate that the fullerene part of PCBM is fragmented into various aromatic pieces [82], due to the shift of the aromatic ^{1}H signals to lower frequencies and the increase of proton bearing carbons.

It is well known that oxygen may undergo a radical reaction with aliphatic C-H groups to form a complex mixture of reaction products, especially under UV irradiation, where excited species are formed. As shown above from solid-state NMR, the fullerene part of the PCBM is especially prone to radical attacks. Thus, it is reasonable to assume that oxygen present in the atmosphere is consumed by the aliphatic PCBM chains first. This process is related with no significant topography changes even though the NMR measurements indicate that the aliphatic side chains were not present any more in the sample. Once a major part of the aliphatic side chains are gone (approx. after 20 hours), oxygen radicals start to react with the aromatic carbon. At this point, some kind of complex (C=O etc.) is formed with the aromatic bucky ball residue, leading to the observed 10% macroscopic increase in thickness. This change is in agreement with the measured thickness increase of the layer as measured before by AFM (Figure 3.2).

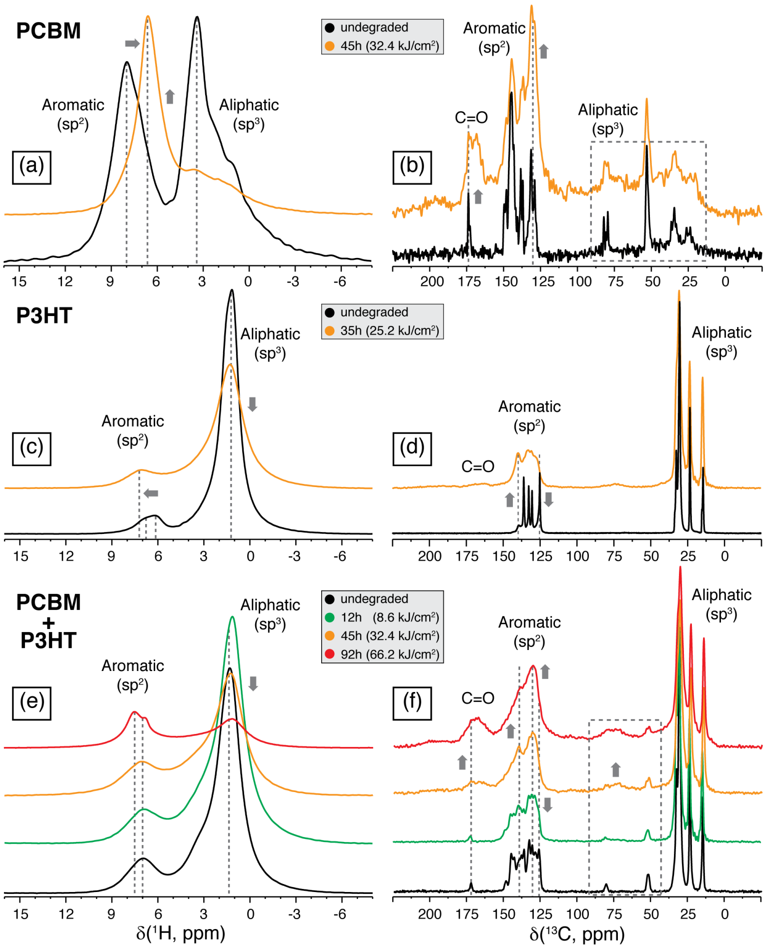

Figure 3.4: Chemical changes upon photo degradation observed using solid-state ^{1}H MAS and ^{13}C^{1}H CP/MAS NMR spectroscopy. Left column: ^{1}H MAS NMR of (a) PCBM, (c) P3HT, and (e) P3HT:PCBM blend. Right column: ^{13}C^{1}H CP/MAS of (b) PCBM, (d) P3HT, and (f) P3HT:PCBM blend. All spectra were recorded at 11.75 T using a spinning frequency of 25.0 kHz. Note that the ^{1}H and ^{13}C spectra are scaled relative to the maxium intensity of the aromatic signals and the aliphatic signal at 24 ppm, respectively. In each part the dashed lines/boxes and arrows indicate the chemical changes as discussed in the main text.

From the UV-Vis data (Figure 3.8a), we observe a peak at 334 nm. This peak is an indication of the presence of mono-substituted fullerene (in this case the side-chain). After exposure to a photon dose of 8.64 kJ/cm^2, this peak goes down indicating the gradual loss of the side-chain. However, nothing can be said about the oxidation of the PCBM from this data.

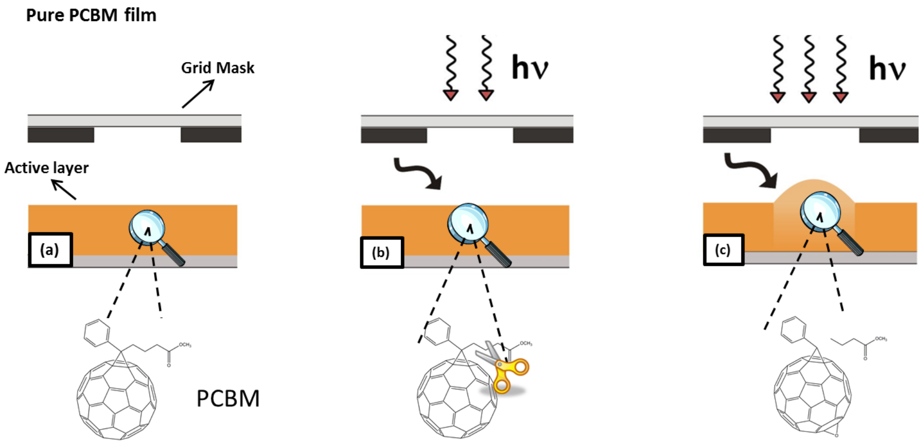

Figure 3.5: Schematic of the processes inside the pure PCBM sample, (a) a zoom into the active layer shows the intact fullerene structure. (b) In the initial stages of degradation, the side chain of the PCBM is first lost. This leads to no change in topography. (c) In the next stages, the oxygen gets incorporated in the C_{60} forming an epoxide structure thereby increasing the layer thickness.

To verify the role of the aliphatic chains of PCBM, thin films of BisIndene C60 (ICBA) were prepared and degraded in a similar way. Since in ICBA no aliphatic side chain is present we expect that oxygen radicals can directly react with the bucky ball. Thus, thickness changes should appear at shorter illumination times. Our measurements indeed revealed an increase in thickness after an exposure to a photon dose of 4.32 kJ/cm^2 (Figure 3.6). The maximum thickness change is in a similar range as the one measured for PCBM (12.4% increase).

In conclusion, the AFM and NMR measurements on PCBM and ICBA suggest that the aliphatic side chain of PCBM can be considered as radical scavengers that protects photo-oxidation of the bucky ball. This is also in accordance to work done by Lloyd et al. [67] where they claim that a decrease in the donor-acceptor charge transfer rate for ICBA results in an increase in the degradation of P3HT as compared to P3HT:PCBM where PCBM significantly enhances resistance to photo-degradation of the P3HT donor polymer.

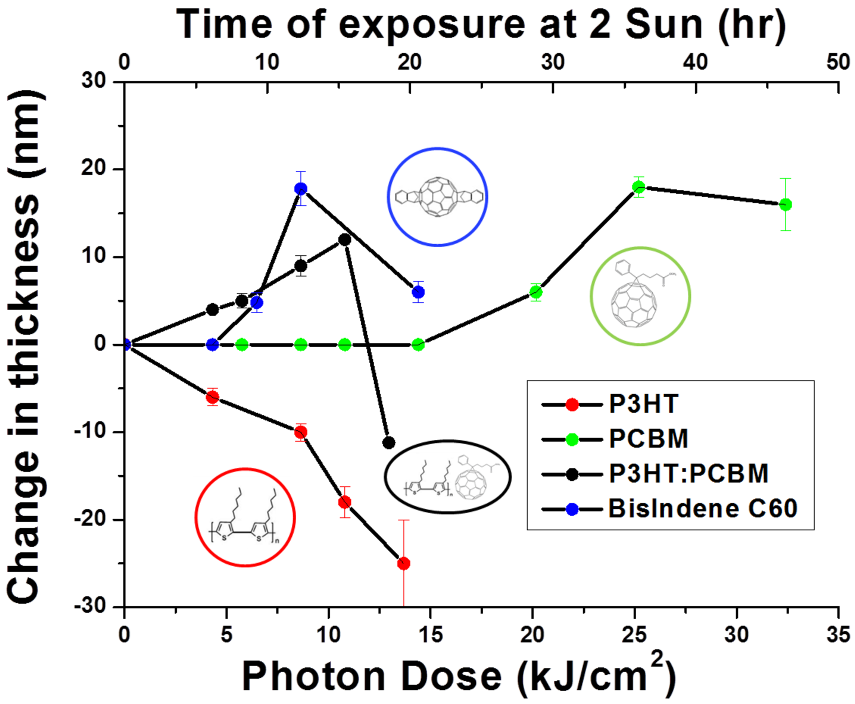

Figure 3.6: The changes in the layer thickness for individual components and the blend in 20% oxygen for different exposure times. The error bars correspond to the measurements done at different positions on the same sample

3.2.2 Degradation of P3HT

In case of pure P3HT, the film thickness started decreasing right from the beginning of the degradation experiment(Figure 3.6). This decrease was attributed to the fragmentation of the polymer chains on photo-oxidation and finally evaporation of the material.

In the UV-Vis spectra, a decrease in the absorption maxima at 510 nm is also observed (Figure 3.8b) which indicates the loss of the intact thiophene ring. Also the shoulder at 610 nm and 560 nm disappears, which indicates the loss of its crystalline domains during degradation.

The degradation for P3HT was observed using ^{1}H and ^{13}C solid-state NMR of a pure P3HT film (Figure 3.5c and d). From the ^{1}H MAS NMR spectrum of

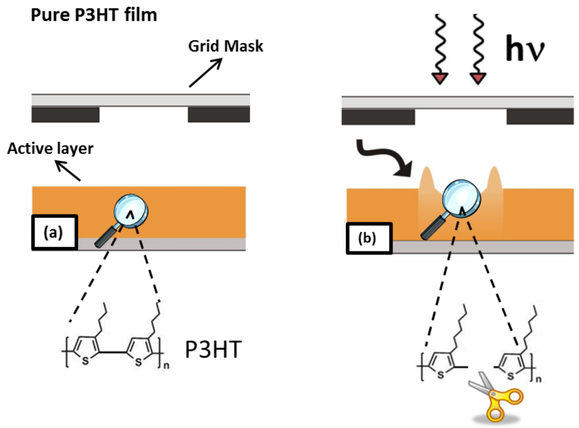

Figure 3.7: Schematic of the proccesses occuring inside the pure P3HT layer (a) A zoom into the layer shows intact P3HT chains. (b) On photo-oxidation, the chains get fragmented and evaporate resulting in a decrease in the layer thickness

non-degraded P3HT (Figure 3.5c) three resonances can be identified at 1.3, 6.1, and 6.8 ppm . Based on their chemical shifts, these resonances can be assigned to those of the hexyl side chains and the thiophene backbone protons [83]. Further, the resonances at 6.0 and 6.8 ppm are related to the crystalline fraction with π-stacked P3HT polymer chains and the amorphous fraction where the P3HT polymer chains are non-stacked, respectively. The presence of crystalline and non-crystalline regions in the P3HT film is also observable in the $^{13}C^{1}H$ CP/MAS NMR spectrum (Figure 3.5d). Here, the narrow and broad resonances originate from crystalline and amorphous fractions, respectively. On degradation for an exposure of 25.2 kJ/cm^2, the ^{1}H MAS NMR spectrum (Figure 3.5c) displays a shift of the signal associated with the π-stacked thiophene groups of P3HT to higher chemical shift along with a decrease in intensity for the aliphatic hexyl side chains. Similarly, the $13C^{1}H$ CP/MAS NMR spectrum in Figure 3.5d shows an increase in the amorphous fraction, in particular the resonance at 138 ppm, and a decrease in the signals from the hexyl side chains. Together these observations demonstrate that the π-stacked fraction of the P3HT film is broken down into smaller P3HT polymer fractions that do not include π-stacking and thereby contribute to the amorphous part of the film. The signal decrease for the aliphatic part demonstrates that the hexyl side chains can be detached and they

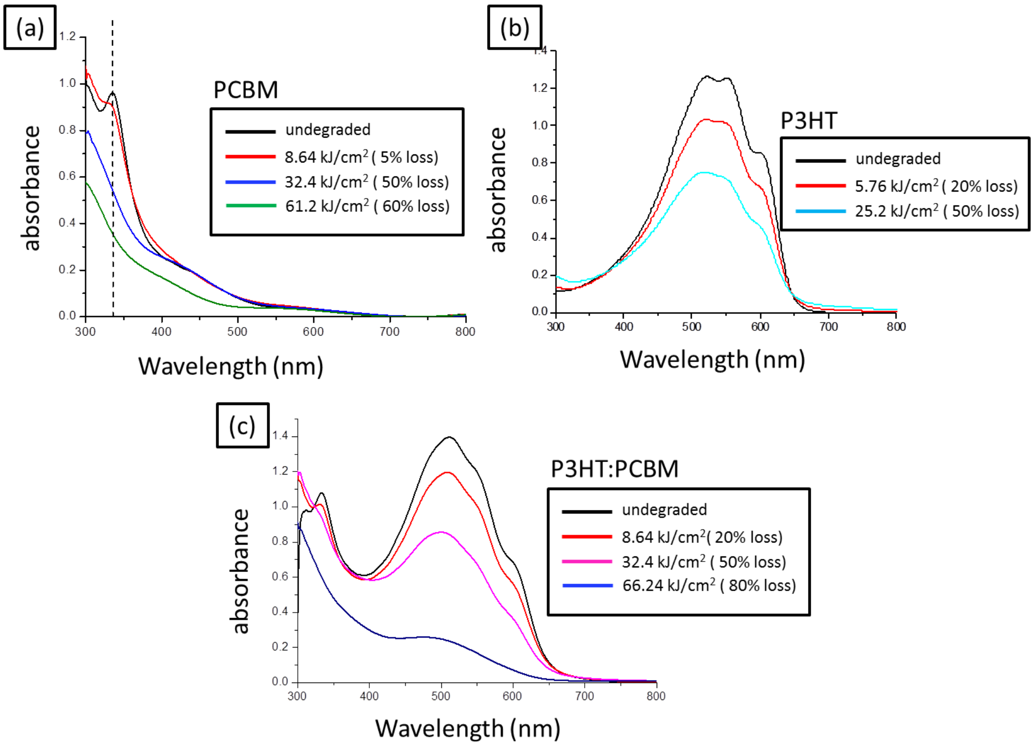

Figure 3.8: (a) Degradation in absorbance of P3HT films in the presence of oxygen and light. The degradation is defined as the loss of absorbance at its maximum (at 510 nm) and is plotted for different time intervals. (b) In case of PCBM films, the loss is defined at the maximum (at 340 nm). (c) In the blend, the degradation is defined as the loss of absorbance at the maximum of P3HT (at 505 nm)

escape as small volatile molecules.

3.2.3 Degradation of P3HT:PCBM blends

In case of the P3HT:PCBM blend, we observed the film thickness starts increasing instantaneously with exposure to light and oxygen (Figure 3.6). This is because the P3HT chain is protected by the aliphatic chain of the PCBM resulting in a direct incorporation of oxygen at the bucky ball making the active layer swell (Figure 3.9). After reaching a maximum value of thickness, the film starts collapsing indicating the fragmentation of the components and finally evaporation of the material.

In the UV-Vis spectra (Figure 3.8c), the degradation was defined as the loss of absorbance at the maximum of P3HT (at 505 nm). Here, one can also see that also the PCBM is degrading. But in the case of PCBM, it is quite difficult to quantify degradation, because only one side peak is visible in this region (334 nm). This peak is an indication of a mono-substituted fullerene (in that case the side-chain). If a second species is attached to the fullerene cage, e.g. oxygen, the peak at 334 nm vanishes, but the spectra itself is hardly affected. That means if one oxygen is attached to the fullerene, this peak drops a little bit and the region left from the peak goes up, so that the peak is no longer visible.

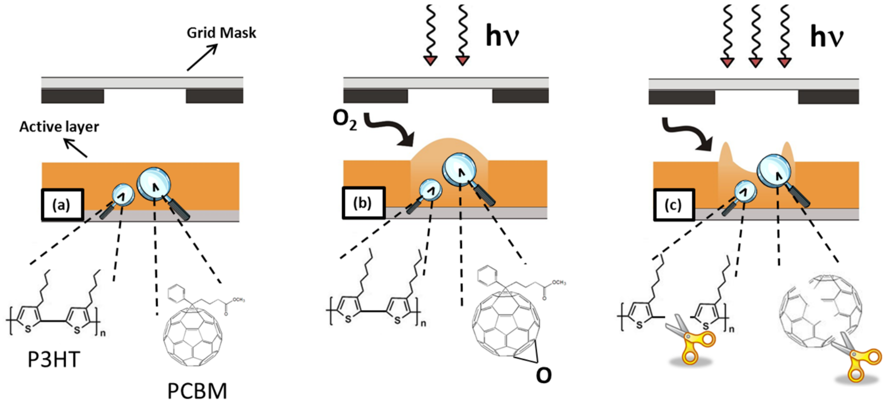

Figure 3.9: Schematic of the proccesses occuring inside the P3HT:PCBM blend. (a) a zoom into the active layer shows the P3HT and PCBM molecules. (b) On photo-oxidation, incorporation of oxygen into the PCBM results in swelling of the layer. (c) On illuminating the sample for a longer time, the P3HT and the PCBM both get fragmented and evaporate, resulting in the collapse of the layer.

Figure 3.4e and f show the solid-state NMR spectra of the P3HT-PCBM films degraded from 0 to 80% (with a photon dose from 8.64 to 66.24 kJ/cm^2). Compared to the NMR spectra of the pure and degraded P3HT and PCBM samples in Figure 3.4a-d, it is clear that the spectra of the P3HT-PCBM blend include a signficant overlap between the two components. However, with the information derived from the pure components it is possible to obtain a qualitative description of the structural changes in the P3HT-PCBM blend upon degradation. From the ^{1}H MAS NMR spectra in Figure 3.4e, the aromatic region (sp^2) includes a broad ^{1}H resonance centered at 7.0 ppm. At 80% (66.24 kJ/cm^2) degradation this resonance shows a small splitting and a shift of the main intensity to low field at

≈7.5 ppm. This observation indicates that the aromatic fragments in the blend at high levels of degradation are present as small substituted aromatic moeties in conjugation with carbonyl groups. For the aliphatic region (sp^3) in Figure 3.4e, the broad ^1H signal centered at ≈1.5 ppm decreases and shifts to high field (lower ppm values) on increasing the level of degradation. This feature is similar to that observed for pure P3HT (Figure 3.4c) and shows that the hexyl side chains are cleaved from the P3HT main chain at high levels of degradation and can escape the P3HT-PCBM blend as small volatile molecules.

The most striking feature of the $^{13}C^1H$ CP/MAS NMR spectra in Figure 3.4f is the increase in linewidth for all ^{13}C resonances in the aromatic and carbonyl region from 120-200 ppm. This increase results in very broad ^{13}C resonances for the aromatic moieties with severe overlap and the introduction of broad carbonyl resonances at higher levels of degradation (≥50%). However, a comparison with the $^{13}C^1H$ CP/MAS NMR spectra in Figure 3.4b and d allows for an assignment of characteristic signals from the P3HT and PCBM domains. This includes the signals at ≈125 and ≈138 ppm, related to the crystalline and amorphous fraction of P3HT, respectively, and the signal at ≈130 ppm from the fragmented PCBM molecules associated with proton bearing carbons in extended aromatic systems. The transformation of well-ordered and crystalline P3HT into fragmented and amorphous domains appears to occur simultaniously with the fragmention of PCBM moeties in the P3HT-PCBM blend. The ^{13}C resonances in the aliphatic region of Figure 3.4f show a slightly increased linewidth with increasing degradation. In particular, the signals from the “handle” [77] of PCBM show this feature, pointing towards disordered regions of the fragmented PCBM molecules. Moreover, the aliphatic signals from 10-40 ppm decrease in intensity, as also observed in Figure 3.4e, and include a very broad underlying resonance. The broad underlying ^{13}C resonance shows that the side chains can possibly crosslink, forming a dense disordered network.

3.3 Effect of different oxygen concentrations

To study the effect of the amount of oxygen in the environment on the degradation, the blend samples were next exposed to different concentrations of oxygen for different time intervals. From Figure 3.10, we can say that when there is more O_2 in the environment, the increase in the thickness is faster. However, the maximum thickness attained in all three cases is the same. This suggests that only after the film is saturated with oxygen, it starts fragmenting.

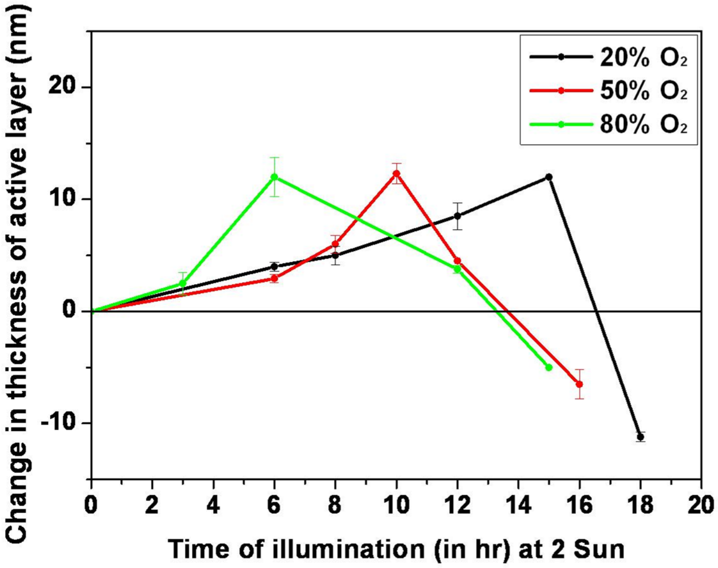

Figure 3.10: The changes in the layer thickness plotted against the time of exposure for 3 different oxygen environments

3.4 Summary

1. Photo-oxidation of PCBM

    a) In early stages of degradation (upto a photon dose of 14.4 kJ/cm^2), no change in topography was observed, after which the topography of the degraded area increased.

    b) From the NMR data we concluded that the oxygen is first consumed by the aliphatic chains of the PCBM. This process does not result in any changes in the topography. However, after a photon dose of 14.4 kJ/cm^2, the oxygen radicals start to react with the aromatic carbon, forming a kind of a complex leading to the observed macroscopic increase in the thickness.

   c) The UV-Vis data also suggested the gradual loss of the side chain indicated by the disappearance of the peak at 334 nm.

2. Photo-oxidation of P3HT

   a) The film thickness started decreasing from the beginning of exposure to light and oxygen. This decrease was attributed to the fragmentation of the polymer and eventually evaporation of the material. This was verified using NMR spectroscopy by observing a decrease in the signal for the aliphatic part which indicates fragmentation of the hexyl side chains.

   b) From the UV-Vis data, we observed a decrease in the absorption maxima at 510 nm which indicated the loss of the intact thiophene ring.

3. Photo-oxidation of the P3HT:PCBM blend

   a) The film thickness started increasing from the beginning of exposure to light and oxygen.

   b) The UV-Vis and NMR data indicate the oxidation of PCBM in the beginning of the degradation. This is followed by the fragmentation of the components present inside the blend.

4

Electrical modes of AFM

4.1 Introduction

Photo-degradation not only changes the morphology of the active layer but also causes changes in the electrical properties. For the measurement of degradation of photovoltaic devices, the device parameters such as the short circuit current I_{SC} and the open circuit voltage V_{OC} are determined. A decrease in I_{SC} and V_{OC}, after exposure to various environmental conditions, indicates quantitatively whether the particular device degrades. However, for the determination of I_{SC} and V_{OC} devices need to be prepared. In order to avoid engineering efforts connected with device preparation, direct characterization methods of the active layer become attractive. In bulk hetero-junction solar cells donor and acceptor materials are phase separated on the nanometer scale. Furthermore, in photovoltaic devices 50 nm to 100 nm thin layers are used as hole or electron blocking layers. As these layers form an interface with the conjugated polymer they might influence the degradation chemistry at their interface. Thus, methods allowing to electrically characterize materials and interfaces at a length scale of nanometers could lead to new insights in degradation processes.

The electric properties of thin films and devices can be investigated on a nanometer scale using a variety of different modes [84, 85, 42, 86]. Using Kelvin probe force microscopy (KPFM) one can measure the local variations of contact potential differences between an AFM-tip and a surface. In particular, the local surface potential of active layers was investigated in dark and upon illumination. These measurements allowed simulation of the working conditions and enabled Hoppe et al. to visualize the photo induced charge carrier generation in a blend material. Wu et al. reported on surface potential changes upon illumination of poly (3-hexylthiophene)/TiO_2 (P3HT/TiO_2) nanorod bulk heterojunction thin films using KPFM. Differences in the contact potential between a non-illuminated and illuminated sample were related to the device performance of the bulk heterojunction materials.

However, while measuring the work function difference between the sample surface and the tip, tip-changes can occur between measurements. In the case of P3HT:PCBM, scanning the same area a second and third time with the same tip revealed changes in the measured potential values. These changes in the measured potential are typical for tip changes, e.g. tip contamination [43, 87, 88]. The difference between degraded and non-degraded areas was almost constant (Figure 4.1). These measurements demonstrate the necessity of using a relative method to study surface potentials by KPFM, which was implemented in our case by using a grid mask while photo-degrading the active layer (as explained in chapter 2). The non-degraded part was used as a reference and the contribution of the tip was accounted for.

In addition, short circuit current conditions can be measured by AFM using the electrical conductive AFM (c-AFM) mode. Coffey et al. used c-AFM to map local photocurrents in the donor/acceptor blend solar cells of the conjugated polymer MDMO-PPV with PCBM. They found that the average photocurrent measured with c-AFM agreed well with the photocurrents for bulk devices with Al contacts and can therefore be correlated with the device performances as well [32].

4.2 Electrical modes of AFM to study degradation

The topography of the spin coated P3HT:PCBM blend was investigated using intermittent contact mode AFM. The surface was found to be smooth having an rms roughness of 0.15 nm for a 10 × 10 μm^2 area. Such roughness values are

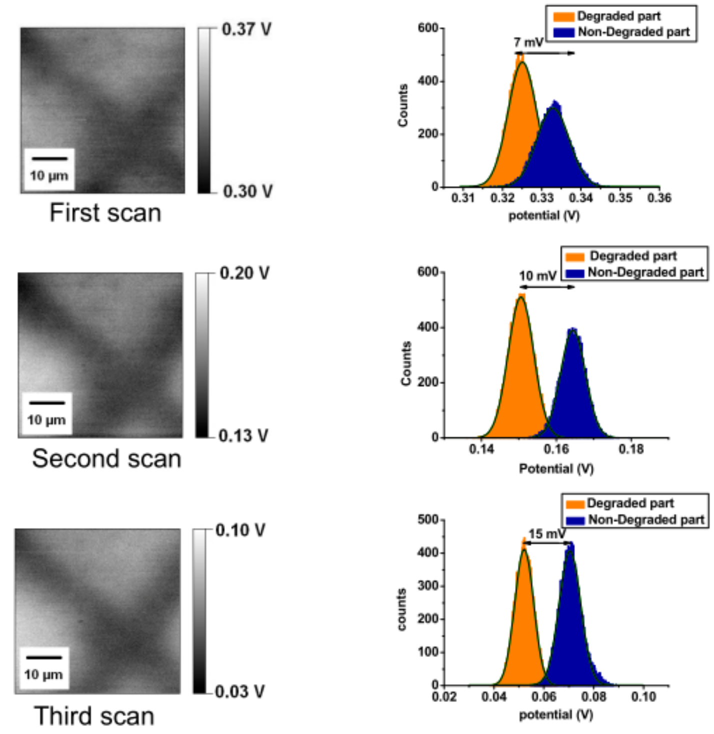

Figure 4.1: The above figure shows 3 scans over the same area in dark conditions. From one scan to another, we see a decrease in the absolute values in potential. This change in potential can be attributed to the tip changes while scanning. However, the difference between the degraded and the non degraded parts remains the same (approx. 10 mV)

in accordance with the literature [43, 59]. Degrading the P3HT:PCBM samples under illumination for 1 hour under synthetic air and 20%. r.h. inside the environmental chamber resulted in no measurable change of the topography (rms roughness $\leq$ 0.2 nm for 10 $\times$ 10 μm^2). Thus, we do not expect a significant influence of the topography on surface potential or conductivity measurements.

4.2.1 Reversible degradation

The KPFM measurement on our sample revealed a difference of surface potential between the degraded and the non-degraded areas even in darkness (Figure 4.2). The degraded area (D) was measured to have a surface potential of 0.325 V

(Figure 4.2a, dark area, labeled with D_{OFF}; OFF stands for 488 nm laser switched off). This value was determined from the average value of a histogram obtained from the potential values measured in the degraded areas. The non-degraded (ND) part corresponded to a surface potential value of 0.332 V (brighter area in Figure 4.2a, labeled with ND_{OFF}). The latter area corresponds to the part which was protected by the mask. The difference between both (ND_{OFF}-D_{OFF}) was calculated to be 0.007 V (Figure 4.2c).

Illumination of the patterned blend in-situ by the 488 nm laser light resulted in a shift in the overall surface potential (Figure 4.2b). We determined a shift of the surface potential by a magnitute of 0.200 V (ND_{ON}-ND_{OFF}) for the non-degraded and 0.215 V (D_{ON}-D_{OFF}) for the degraded areas. Switching off the laser illumination for the consecutive scan showed that the surface potential decreased again. Thus, the potential shifts are attributed to the photo-generation of charges in the P3HT:PCBM blend [89]. Furthermore, under illumination, the surface potential of the degraded area became slightly higher (0.540 V) than the non-degraded area (0.530 V) (Figure 4.2c).

Probing the energy levels using KPFM: An explanation

For the non-degraded part, measured in the dark, the potential of the sample is a combination of the HOMO levels of the P3HT and PCBM (Figure 4.3a) and lies in between the two levels (as indicated by the blue “virtual” level). KPFM measures the contact potential difference between the sample and the probe. In case of the degraded part (Figure 4.3a), the oxygen forms a charge-transfer complex with the P3HT and shifts the level towards the vacuum level[54]. This shift was concluded from XPS studies that showed a decrease of the electron binding energies. Thus, the CPD that is measured lies in between the perturbed P3HT level and the PCBM level (as indicated by the orange “virtual” level). This shift of the CPD between the sample and the probe to lower values was seen in our KPFM studies (Figure 4.2c).

Under illumination, the electrons get excited from the HOMO of the P3HT to its LUMO leaving behind holes. These electrons are transfered to the LUMO

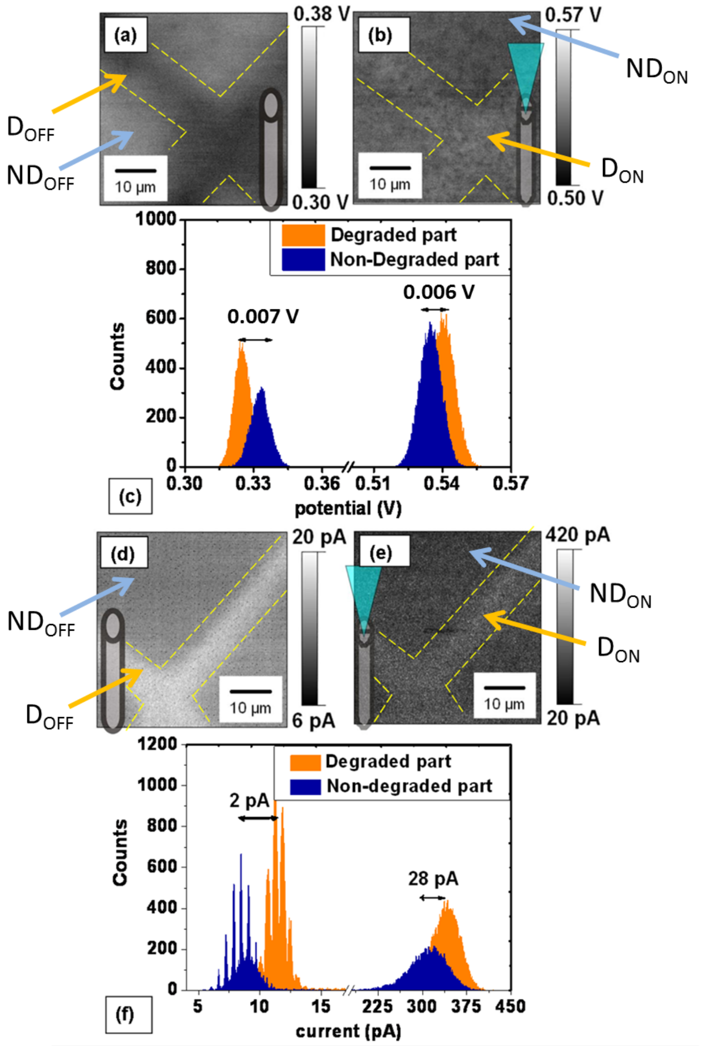

Figure 4.2: (a) KPFM image under dark conditions of the locally degraded sample (1 h, 1 sun, in synthetic air). (b) KPFM image under illumination with a 488 nm laser of a locally degraded sample. (c) Histogram analysis of the KPFM images. (d) c-AFM images under dark conditions of locally degraded sample (1 h, synthetic air). (e) c-AFM image under illumination of the locally degraded sample. (f) Histogram analysis of the c-AFM images. The dashed lines show the boundaries between the degraded and the nondegraded parts.

of the PCBM from where they are lost into the ITO. Measurements under illumination revealed an overall shift towards higher CPD values (Figure 4.3b). This corresponds to an increase in the hole density at the surface. This effect was also observed by Hoppe et al. for toluene-cast MDMO-PPV:PCBM blends, where they claimed that the polymer layer on top of the PCBM clusters was enriched with holes as compared to the pristine films or the blend in the dark [85]. Furthermore, in the degraded area (Figure 4.3c), the CPD was slightly higher than the non-degraded one. This can be associated with the increase in the equilibrium concentration of charge carriers in the degraded areas. Oxygen doping increases the charge carrier concentration in P3HT:PCBM for degraded samples (synthetic air and white light exposure) as reported by Seeman et al. [18] and Schafferhans et al. [21]. Therefore, in these regions a higher concentration of holes is left behind which in turn increases the CPD.

In order to prove the influence of charge carrier concentration, the current through the film was measured by conductive scanning force microscopy [32]. At a bias voltage of 4 V, the c-AFM measurements showed that the degraded part corresponded to a higher current compared to the non-degraded part in darkness (Figure 4.2d). This finding is in agreement with an increase in the charge carrier concentration for the degraded areas. Upon illumination of the locally degraded sample, the measured current increased to 312 pA and 340 pA for the non-degraded and degraded areas respectively (Figure 4.2e and f). This shift in current is associated with the additional charge carriers that were photo-generated. Even under illumination the non-degraded areas exhibited a lower current and reflected the differences in local charge carrier concentration.

Seeman et al. [18] reported that the degradation for illumination under our conditions (1 h, 1 Sun, synthetic air + 0% r.h.) was partially reversible. Device measurements have shown that after exposure for 1 hour in 20% O_2 and 80% N_2 the V_{OC} decreased to 86% of the intial value. After annealing for 5 min at 140°C, V_{OC} increased again to 89% of the original V_{OC}. The reason behind this partial reversibility was attributed to the formation of charge transfer complexes with oxygen, which is reversible [18, 21]. Also, reversible degradation was studied by Tromholt et al. [58] where they exposed inverted P3HT:PCBM solar cells at 5 suns for 30 mins. Then, instead of annealing the degraded samples, they kept them in dark for 30 minutes and observed a partial recovery of the lost performance. To investigate the reversibility of the degradation, we annealed

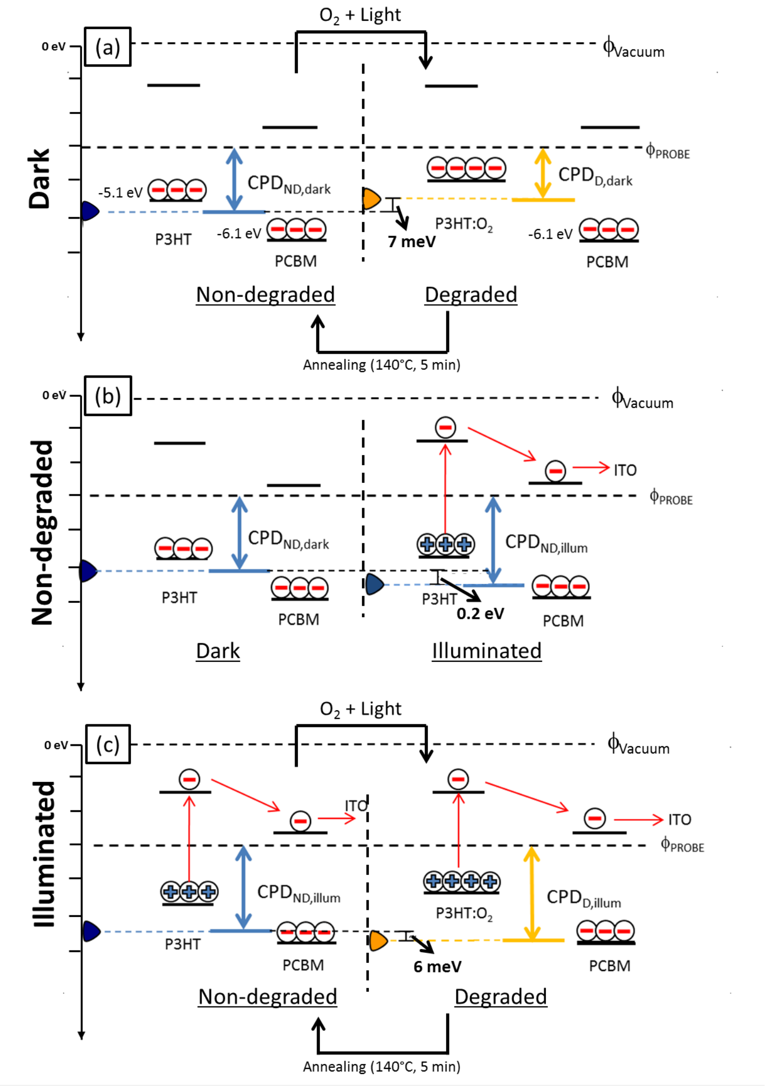

Figure 4.3: Energy levels of P3HT:PCBM as probed by KPFM under dark and illuminated conditions. (a) Comparison between the non-degraded and degraded areas in dark conditions (b) Comparison of the non-degraded area under dark and illuminated conditions and (c) Comparison between the non-degraded and degraded areas under illumination. ϕ_{Vacuum} and ϕ_{PROBE} represent the vacuum levels and the work function of the AFM probe respectively

our sample for 5 min at 140°C and measured again using KPFM and c-AFM (Figure 4.4). After annealing, any variation on the measured surface potential measured by KPFM disappeared. This finding indicates that the degradation was completely reversible at least to the depth that KPFM could probe. Furthermore, no contrast was observed under illumination at 488 nm.

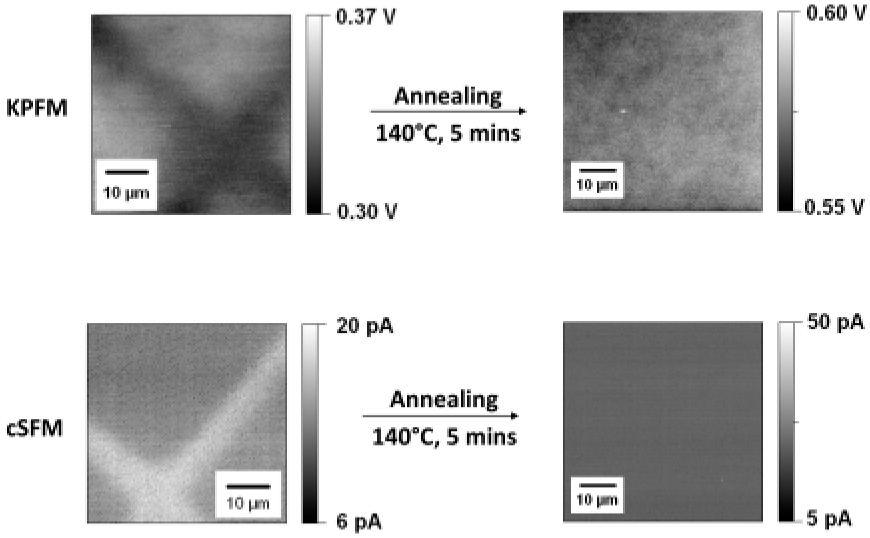

Figure 4.4: After degrading the sample (P3HT:PCBM) for 1 hour in 20% synthetic air, KPFM and c-AFM measurements (bias voltage 3 V) showed partial degradation. On annealing these samples for 5 mins at 140°C, the degradation was found to be completely reversible (as seen in the images above). The difference in the absolute values of potential is attributed to the changes in the tip.

4.2.2 Irreversible degradation

Degradation of organic solar cell materials consists of a fast component which was fully reversible and a slow component which was only partly reversible [20]. In order to study irreversible degradation, we degraded the P3HT: PCBM layer in synthetic air and 20% r.h. for longer times, i.e. 18 hours at 2 Sun intensity. Again, the samples were measured using KPFM and c-AFM (Figure 4.5).

The KPFM characterization of the degraded sample under dark conditions revealed an average surface potential of -0.700 V (Figure 4.5, D_{OFF}). For the non-degraded part a surface potential value of -0.790 V was measured (Figure 4.5, ND_{OFF}). We noted two main observations from the KPFM characterization. First, this measurement showed a shift in the absolute values of the degraded and

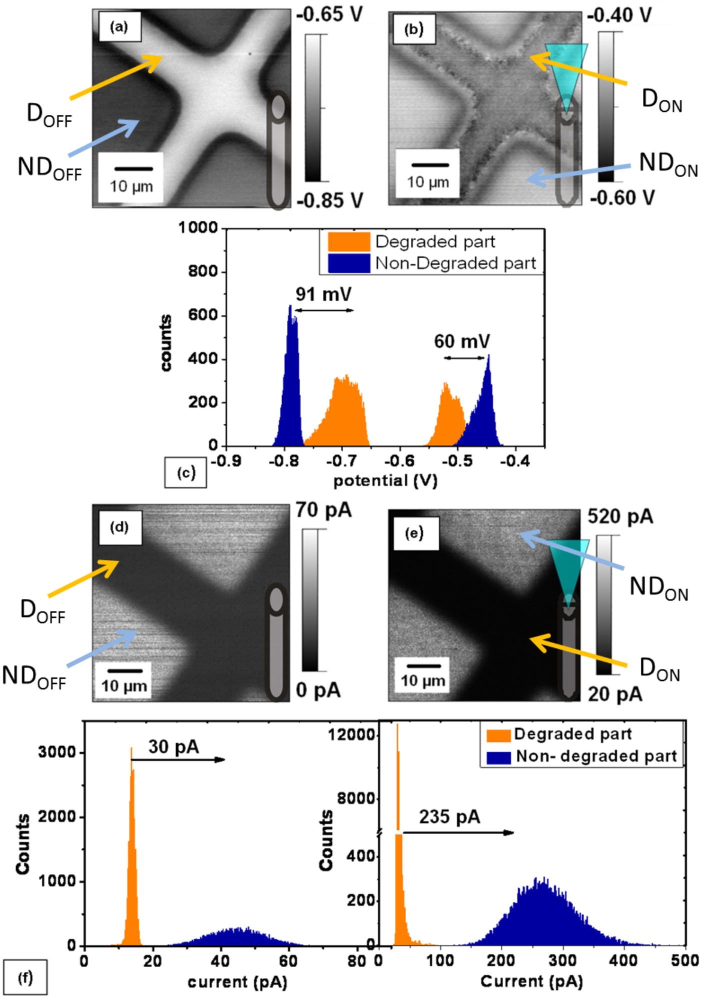

Figure 4.5: (a) KPFM image under dark conditions of locally degraded sample (18 h, 2 Sun, synthetic air, 20% H_2O). (b) KPFM image under illumination with a 488 nm laser of locally degraded sample. (c) Histogram analysis of the KPFM images. (d) c-AFM image with a bias voltage of 3 V images under dark conditions of locally degraded sample (18 h, 2 Sun, synthetic air, 20% H_2O). (e) c-AFM image under illumination of the locally degraded sample. (f) Histogram analysis of the c-AFM images.

the non-degraded part compared to the measurement done for 1 h (Figure 4.2a). We associate these shifts to differences in the tip work function (e.g. contamination) since the samples were prepared using the same procedure. Second, the degraded part had a higher surface potential than the non-degraded part. This observation is in accordance with the XPS studies reported by Hintz et al. [54]. At longer exposure times to light and oxygen, the XPS signals corresponded to shifts of the C and S peaks towards higher binding energies than pristine P3HT.

Next, the same area was measured under illuminated conditions. The average value of the surface potential of the degraded area shifted to -0.510 V (Figure 4.5b, D_{ON}). In addition, the surface potential of the non-degraded area shifted to -0.450 V (Figure 4.5b, ND_{ON}). Here the surface potential of the non-degraded area shifted significantly more (0.060 V) than the one of the degraded area. Thus, the KPFM result suggests less positive charge formation in the degraded area. We attribute this decrease also to the decreased light absorption in the degraded area, which is in the order of 50% (Figure 4.6). Furthermore, on annealing the sample for 5 mins at $140°C$ no changes were observed implying that the degradation was non-reversible.

From the above results, we can conclude that illuminating the sample for longer times results in irreversible degradation. This is attributed to the fragmentation of the polymer chains and photo-oxidation which changes the chemical structure of the molecules present inside, and this observation also agrees well with our discussion in chapter 3.

4.3 Quantifying degradation

To quantify the extent of degradation and to compensate the contribution of the tip and therefore the errors due to possible contaminations and differences in the tip work function, we took the difference between ND_{OFF} and D_{OFF} within the same KPFM image. Then, under illumination, we again calculated the difference between ND_{ON} and D_{ON}. In this kind of differential analysis, differences and changes in the tip work function cancel out. Finally, in order to quantify the effect of illumination (i.e. photo carrier generation, charging of surfaces), we subtracted these two differences to get a measure of the degradation $K_{(ON-OFF)}$ of the active layer (Equation4.1)

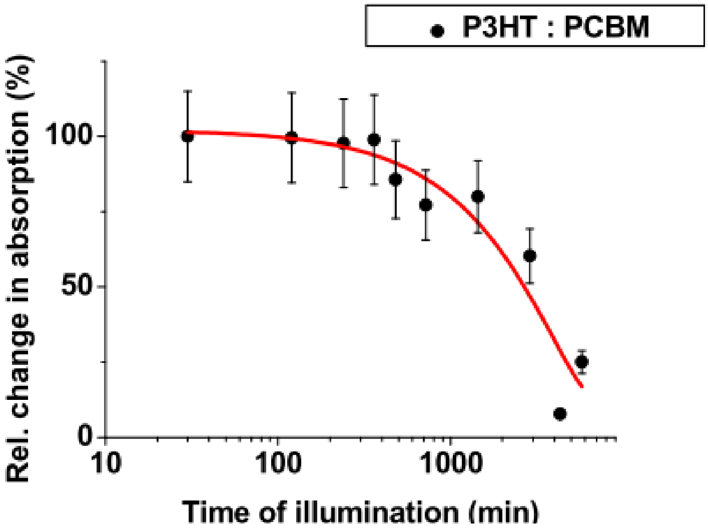

Figure 4.6: The P3HT:PCBM active layer was degraded in ambient conditions for different time intervals at 1 Sun. Then the UV-Vis absorption spectra for samples were measured and the relative decrease of the absorption peak at the P3HT maximum (at ≈500 nm) and for PCBM (at ≈340 nm) was determined. The above figure shows the relative decrease in the absorption peaks with increasing time of degradation for P3HT:PCBM

$$K_{(ON-OFF)} = (ND_{ON} - D_{ON}) - (ND_{OFF} - D_{OFF}) \tag{4.1}$$

By simply rearranging this equation, we can rewrite as

$$K_{(ON-OFF)} = (ND_{ON} - ND_{OFF}) - (D_{ON} - D_{OFF}) \tag{4.2}$$

Here, $ND_{ON} - ND_{OFF}$ and $D_{ON} - D_{OFF}$ reflect the photo response of the non-degraded area and degraded areas, respectively. For a comparison of samples degraded at different environmental conditions the difference $ND_{ON} - ND_{OFF}$ remains constant while $D_{ON} - D_{OFF}$ is inversely dependent on the degradation. Thus, the value $K_{(ON-OFF)}$ is correlated to the amount of degradation that is associated to the photo response. For the above example (degradation for 18 h in 2 Sun in synthetic air + 20% r.h.), the KPFM study revealed a $K_{(ON-OFF)}$ value of 0.150 V.

In analogy to the KPFM data, we recorded and analyzed the data from c-AFM under dark and illuminated conditions (Figure 4.5d-f). In the dark, the degraded area corresponded to an average current of 14 pA (D$_{OFF}$) and the non-degraded part corresponded to 45 pA (ND$_{OFF}$). Under illumination, the average current shifted to more positive values for the non-degraded area (267 pA, ND$_{ON}$) which is attributed to the additional photo-generation of charges. However, the measured current of the degraded area (30 pA, D$_{ON}$) did not increase much on illumination. These measurements indicate that the active layer degraded significantly corresponding to a difference between $D_{ON} - D_{OFF}$ of 16 pA. Thus, we conclude that the conductivity of the degraded active layer decreased significantly. Using a similar approach as above for the quantification of degradation, we calculate $C_{(ON-OFF)}$ as a measure for degradation, given by

$$C_{(ON-OFF)} = (CND_{ON} - CD_{ON}) - (CND_{OFF} - CD_{OFF}) \tag{4.3}$$

For the irreversibly degraded sample, we obtain a $C_{(ON-OFF)}$ value of 205 pA. For the sample that was degraded only for one hour in synthetic air, we obtained a $C_{(ON-OFF)}$ value of 26 pA. Thus, these values represent the extent of degradation of the active layer as well.

4.3.1 Degradation in different environmental conditions

Light, however, is not the only reason for degradation. In order to find out the role of oxygen, humidity and light for the degradation process, we degraded samples under different environmental conditions. All experiments were done under identical illumination conditions (2 Sun). Then, the extent of degradation for the different environments were compared using the KPFM and c-AFM measurements and analyzed as described above (Figure 4.7).

Illuminating a sample in a pure N_2 environment for 36 hours resulted in no measurable change in the topography of the P3HT:PCBM film. The $K_{(ON-OFF)}$ as well as the $C_{(ON-OFF)}$ values were calculated to be 0 V and 0 pA, respectively (Figure 4.8). As a next step, we degraded the active layer in 80% r.h. and

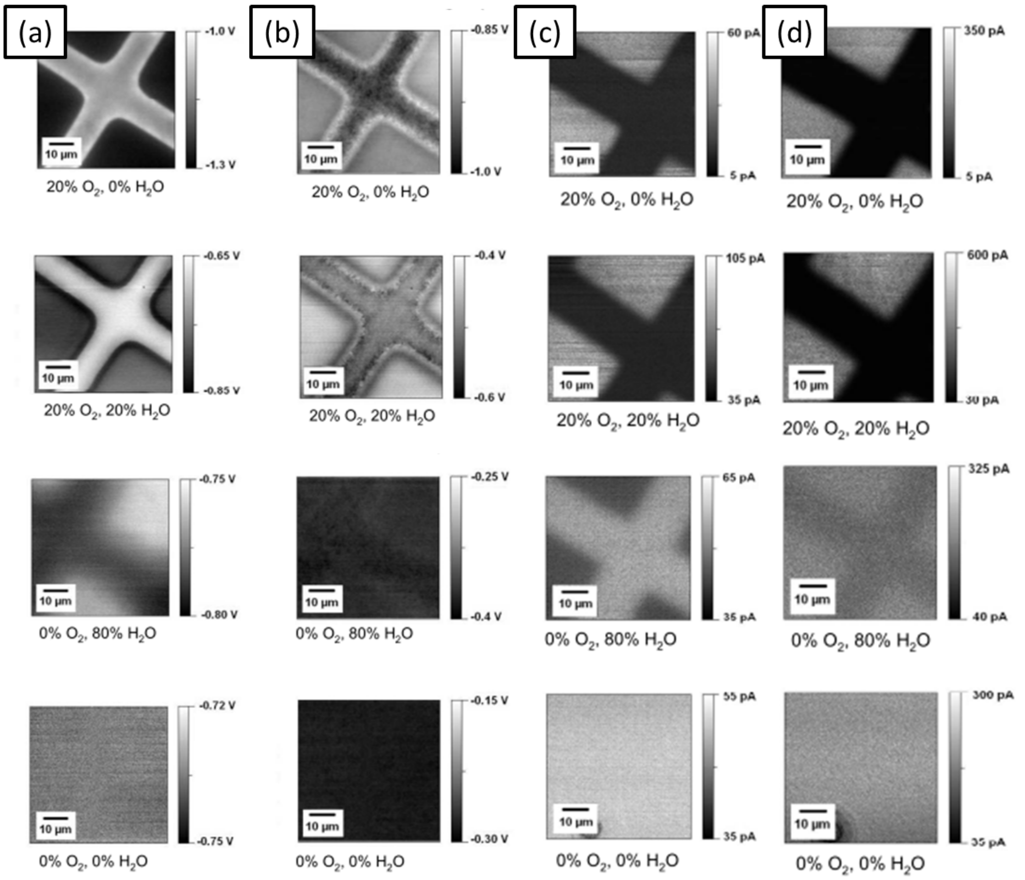

Figure 4.7: Locally degraded P3HT:PCBM under different environmental conditions for 18 hours at 2 Sun, (a) KPFM images taken in dark conditions (b) under illumination with a 488 nm laser (c) c-AFM images taken in dark and (d) under illumination. A bias voltage of 3 V was applied.

0% O2 for 36 hours. No change in topography was observed in this case. Very small values for $K_{(ON-OFF)} = 0.004$ V and $C_{(ON-OFF)} = 37$ pA were determined, respectively. This implies that humidity along with light does not degrade the P3HT:PCBM active layer very much. Subsequently, we degraded the sample in synthetic air and 0% r.h. Here, a change in the topography was observed between the degraded and the non-degraded areas. This change in topography is associated to the fragmentation of the polymer chains and evaporation of the material (as discussed in detail in chapter 3). Also, the $K_{(ON-OFF)}$ and $C_{(ON-OFF)}$ values increased to 0.190 V and 139 pA, respectively (Figure 4.8). The measurement series was completed by the exposure of the sample to synthetic air and 20% r.h.

for 18 hours as presented in Figure 4.8. The topography difference between the degraded and the non-degraded areas is approximately the same as for degradation in pure oxygen. The $K_{(ON-OFF)}$ and $C_{(ON-OFF)}$ values also remain in the same realm within the error range compared with the ones obtained under synthetic air and 0% r.h. (0.150 V and 199 pA).

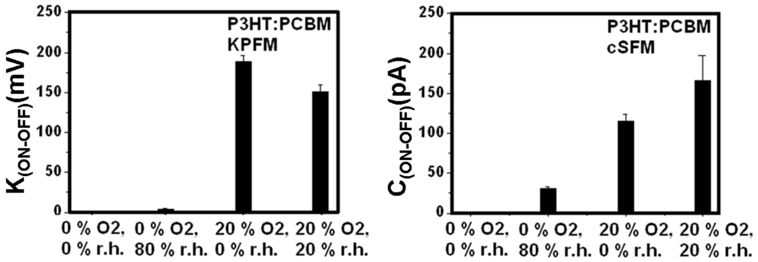

Figure 4.8: $K_{(ON-OFF)}$ and $C_{(ON-OFF)}$ values plotted for different environmental conditions. The error bars correspond to measurements done at different positions on the same sample.

From the above data, we conclude that light alone does not degrade the samples. Oxygen along with light plays the major role in degradation of these materials. Also, keeping these materials in dark in oxygen environment does not degrade the samples.

4.4 Studying degradation of individual component: P3HT

In addition to measuring the degradation of blends, we can use this technique to study degradation of the individual components of the blend, i.e, the polymer P3HT. Thus, a thin layer of P3HT that was spin coated on the conducting substrate was degraded in synthetic air for 6 hours at 2 Sun through the grid mask.

First, the P3HT layer was investigated using KPFM (Figure 4.9). Following the previously described measurement and analysis under dark and illuminated condition,s we calculated a $K_{(ON-OFF)}$ value of 0.060 V for a degradation for 6

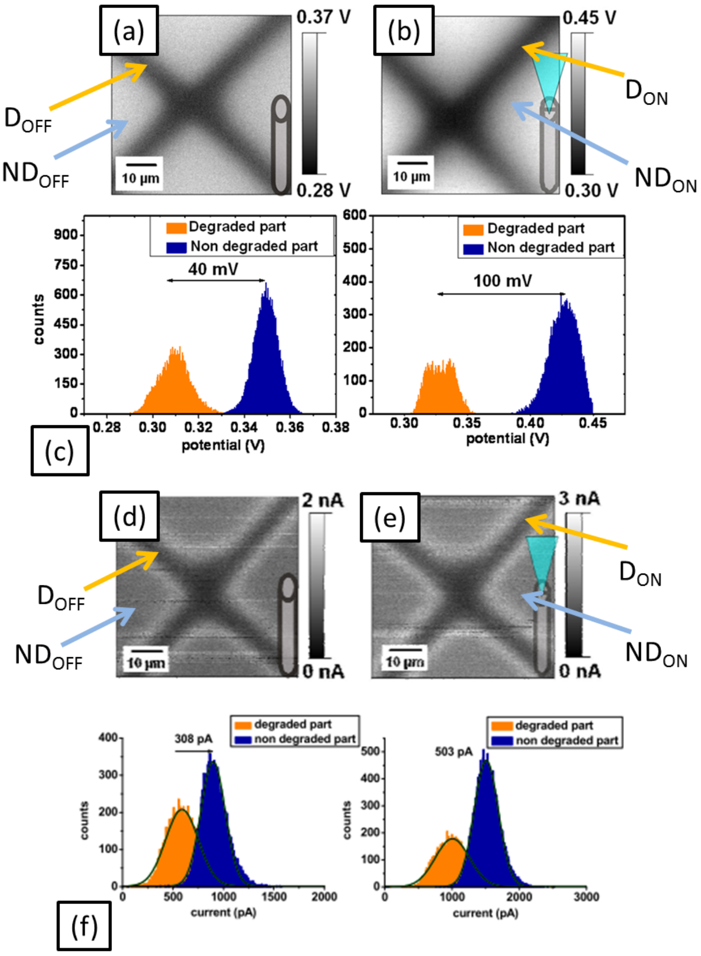

Figure 4.9: (a)KPFM image of locally degraded P3HT sample (6hr, 2 Sun, in synthetic air) in dark and (b) under illumination with a 488 nm laser, (c) histogram analysis of the KPFM image. (d) c-AFM image of locally degraded P3HT in dark and (e) under illumination, (f) histogram analysis of c-AFM image. A bias voltage of 4 V was applied.

hours in synthetic air at 2 Sun. Furthermore, in dark conditions, the degraded area was measured to have a mean current value of 589 pA (dark area, D_{OFF}). The non degraded part corresponded to a current value of 897 pA (bright area, ND_{OFF}). The difference (ND_{OFF} - D_{OFF}) was calculated to be 308 pA (from histogram). Next, the same sample was measured under illumination conditions. The mean value of the current of the degraded area shifted to 1006 pA (dark area, D_{ON}) and that of the non degraded part shifted to 1509 pA (bright area, ND_{ON}). The difference (ND_{ON} - D_{ON}) was calculated as 503 pA. From the above values, we can calculate, $C_{(ON-OFF)} = 195$ pA which gives an estimate of the degradation (Figure 4.9).

Comparison of P3HT with the P3HT:PCBM blend

In order to compare the above values with the blend, we degraded P3HT:PCBM (1:1) in synthetic air for 6 hours at 2 Sun. Following this, KPFM and c-AFM measurements were performed on this sample. On analysing the images with histograms, we calculated, $K_{(ON-OFF)} = 0.02$ V which gave an estimate of degradation. The $C_{(ON-OFF)}$ value corresponded to 500 pA (bias voltage 4 V).

Thus, from the above results we can conclude that when PCBM is blended with P3HT, the photoconductivity is reduced significantly after degradation. This reduction is in accordance with our previous observations in chapter 3 and also with absorption and photoconductive studies done by Reese et al. [63]. They reported that the fullerene cage of PCBM undergoes a series of oxidations that are responsible for the deterioration of the photoconductivity of the blend. The LUMO levels of O_n(PCBM) become deeper as the number of oxygen molecules (n) increases. These oxidized molecules act as deep traps inside the PCBM domains reducing the photoconductivity.

4.5 Summary

1. Early stages of degradation (photon dose of 0.36 kJ/cm^2) result in changes in electrical properties of the solar cell devices. To observe these changes locally on the active materials we used the electrical modes of AFM, namely, KPFM and c-AFM.

2. Thin layers of active blends were degraded through a grid mask under controlled environment. The use of the grid mask allowed us to do relative measurements between degraded and non-degraded areas within the same scan image, thereby, neglecting the effect of tip contributions.

3. Exposing the samples to photon doses of 0.36 kJ/cm^2 resulted in shifting of the energy levels of the polymer due to the formation of charge-transfer-complexes with oxygen.
    a) These shifts could be measured using KPFM which determines the difference in potentials of the tip and the HOMO levels of the active materials.
    b) Due to the oxygen doping an increase in the charge carrier concentration in the degraded areas was observed, compared to the non-degraded ones using c-AFM.
    c) This degradation was reversible on annealing the samples at 140°C for 5 mins due to the reversible nature of charge-transfer-complexes formed between the polymer and oxygen.
4. Degrading the samples for longer time intervals (photon dose of 12.9 kJ/cm^2 in synthetic air) showed irreversible degradation. By analysing the light induced changes on these degraded samples, we were able to quantify the degradation and thus also compare the degradation in different environments.
    a) Studying the samples in different environments showed that light alone did not degrade the samples at all.
    b) Light along with oxygen (ie, photo-oxidation) played a major role in degradation of the active layer.
5. The individual component (eg. P3HT) of the blend was studied for degradation. A faster decrease in photoconductivity of the blend was observed on degradation compared to P3HT. This was attributed to the photo-oxidation of the PCBM in the blend which forms trap states thereby reducing the conductivity of the blend.
6. For our type of degradation studies, the electrical properties of the materials could be inferred without the need to make fully operational devices. This saves additional efforts connected to device preparations.
7. Different materials can be compared for stability to determine the best

candidates for solar cell applications.

5

Investigations of new low bandgap materials

5.1 Introduction

The open circuit voltage (V_{OC}) is given by the difference between the HOMO of the electron donating polymer and the LUMO of the electron acceptor. In order to achieve high photovoltaic performance, this difference should be maximized. In case of P3HT, the optical bandgap (1.9 eV) is not optimized to the maximum photon flux of the solar spectrum, which is around 1.6-1.8 eV [90]. Low-bandgap polymers provide improved light harvesting in the near-infrared region thereby increasing the power conversion efficiency [91, 92, 93]. Due to the intrinsic losses to overcome the exciton binding energy (0.1-1 eV), the optimum bandgap was found to be shifted towards higher values. Therefore, a bandgap of 1.3-1.5 eV is regarded as ideal for polymer-fullerene solar cells [90].

PCPDTBT has an optical bandgap of 1.4 eV and is an excellent candidate for light harvesting devices (Figure 5.1a) [90]. In addition, electrochemical studies indicate sufficiently deep HOMO/LUMO levels that enable a high open-circuit voltage in photovoltaic devices when fullerene derivatives are used as electron transporters. Furthermore, steady state and transient photoconductivity studies have been performed by Soci et al. [94] on this material and they confirmed efficient photogeneration of charges in the PCPDTBT: PCBM blend as compared to P3HT:PCBM blend. They also claim that the combination of the superior transport properties of polythiophene-based materials and the better match of the spectral response to the solar emission spectrum, as exhibited by PCPDTBT, implies that when fully optimized, PCPDTBT:fullerene bulk heterojunction devices should achieve photovoltaic efficiencies well above 5%.

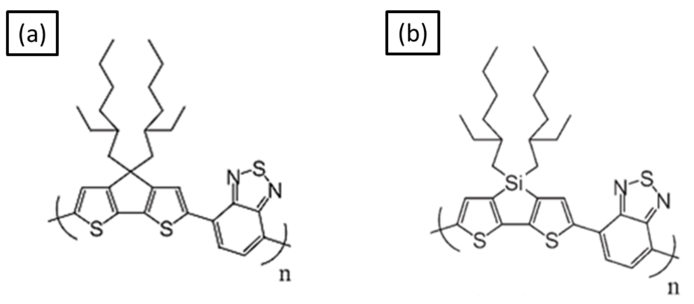

Figure 5.1: Molecular structure of (a)PCPDTBT and (b)Si-PCPDTBT

Another promising class of low bandgap materials include the silicon-bridged (Si-PCPDTBT, chemical structure shown in Figure 5.1b) dithiophene donor-acceptor copolymers [95, 96]. Scharber et al. showed that simply by replacing a carbon atom with a silicon atom on the main chain of the conjugated polymer, a higher crystallinity, improved charge transport properties and a reduced bimolecular recombination and formation of charge transfer complexes is achieved when blended with a fullerene derivative. Replacing the carbon by a silicon atom introduces a small distortion of the cyclopentadithiophene unit. This longer Si-C bond modifies the geometry of the fused dithiophene unit which is enough to achieve a better ordering of the polymer chains leading to the above improvements. This polymer was the first low-bandgap semiconducting polymer to have a certified efficiency of over 5%. Some of the earlier degradation studies include the role of fullerenes [97] and hole transporting layers [98] on the performance of solar cells based on this material. However, this is the first time this material itself is being investigated for stability.

UV-Vis and IR spectroscopy studies done by Manceau et al. [22] reported that the key step of the P3HT degradation mechanism is the H-abstraction in the alkyl side chain at the α position of the thiophene ring. In case of PCPDTBT, this position is protected by another alkyl chain (as shown in Figure 5.1). These alkyl chains don't allow the oxygen to attack the α position thereby making it more stable against oxidation.

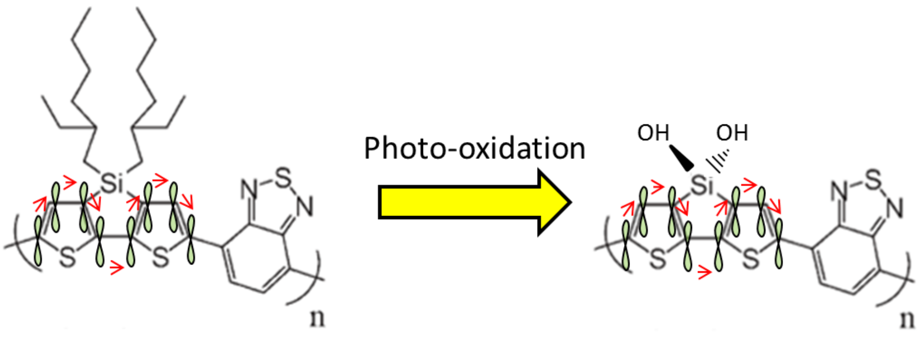

Figure 5.2: Degradation mechanism in Si-PCPDTBT. Red arrows indicate the charge transfer through the π network.

Si-PCPDTBT is a sp^2 hybridized system where p-orbitals of adjacent atoms overlap to form a conjugated system with delocalized electrons. The charge transport takes place through these π bonds in the molecule (Figure 5.2, red arrows). The C-Si bond has a length of 186 pm and is weaker than the C-C bond [99], as in the case of PCPDTBT. On photo-oxidation, the oxygen molecules attack this weak C-Si bond and bind themselves to Si. The Si-O bond is short and extremely strong which makes the molecule very stable. In this case, the attack of oxygen does not interfere with the π system, thereby keeping the charge transport along the polymer backbone as before. Si-PCPDTBT acts as a radical scavenger due to which the process of degradation is delayed. This should make the blend highly stable against photo-oxidation as compared to other polymer-fullerene blends.

5.2 Comparing stabilities of PCPDTBT:PCBM, Si-PCPDTBT:PCBM and P3HT:PCBM

With our method, as described in chapter 4, we were able to compare the stabilities of these new molecules with P3HT:PCBM without having to make an entire solar cell device. To quantify the degradation of PCPDTBT: PCBM, we degraded thin layers of this material in synthetic air for 18 hours at 2 Sun. The KPFM measurement on our sample revealed a difference of surface potential between the degraded and the non-degraded areas in darkness (Figure 5.3a). The degraded area (D) was measured to have a contact potential difference of -1.16 V (Figure 5.3a, labeled with D_{OFF}; OFF stands for 488 nm laser switched off). This value was determined from the average value of a histogram obtained from the potential values measured in the degraded areas. The non-degraded (ND) part corresponded to a surface potential value of -1.25 V (ND_{OFF} in Figure 5.3a). The latter area corresponds to the part which was protected by the mask. The difference between both ($ND_{OFF} - D_{OFF}$) was calculated to be -0.09 V (Figure 5.3c). Similarly, calculating ($ND_{ON} - D_{ON}$) we get a value of -0.01 V. From the equation given below (also described in chapter 4),

$$K_{(ON-OFF)} = (ND_{ON} - ND_{OFF}) - (D_{ON} - D_{OFF}) \tag{5.1}$$

we get a $K_{(ON-OFF)}$ value of 0.08 V. Comparing this value with the P3HT:PCBM sample, we find that the PCPDTBT:PCBM blends are more stable in oxygen environment. Similarly, the $C_{(ON-OFF)}$ value was calculated to be 68 pA (Figure 5.3d,e,f). This value is also less than the P3HT:PCBM sample indicating that PCPDTBT:PCBM blends are more stable in oxygen environments.

Next, the Si-PCPDTBT:PCBM blends were investigated by degrading thin layers (100 nm) of this blend material for 19 hours at 2 Sun in synthetic air. The $K_{(ON-OFF)}$ value was found to be 5 mV (Figure 5.4a,b,c). On performing c-AFM measurements on these samples (Figure 5.4d,e,f), we see that in dark conditions, the degraded part corresponded to a higher current compared to the nondegraded part. This is seen in the early stages of degradation when O_2 doping in the exposed part causes an increase in the charge carrier concentration for the

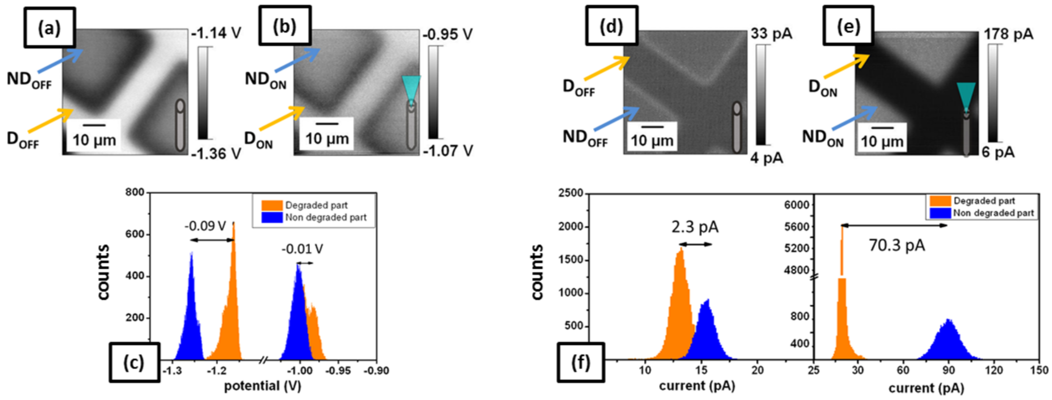

Figure 5.3: KPFM images of locally degraded PCPDTBT:PCBM (18hr, 2 Sun, in synthetic air)sample (a) in dark and (b) under illumination with a 488 nm laser, (c) Histogram analysis of the KPFM images, (d) c-AFM images (bias voltage of 4 V) of locally degraded PCPDTBT:PCBM sample (18hr, 2 Sun, in synthetic air) (d) in dark and (e) under illumination, (f) histogram analysis of c-AFM images.

degraded areas. Upon illumination of the locally degraded sample, the measured current increased to 190 and 243 pA for the non degraded and the degraded areas, respectively. This shift in current is due to the additional charge carriers that were photogenerated. From these values we conclude that even after 19 hours of exposure to 2 Sun, the Si-PCPDTBT:PCBM blend was in the early stages of degradation. This indicates Si-PCPDTBT:PCBM is even more stable against photo-oxidation.

To study the stability of PCPDTBT:PCBM and Si-PCPDTBT:PCBM under different environmental conditions, we compared their degradation with the degradation of P3HT:PCBM blends. In inert conditions, all the blends were stable and did not degrade after 18 hours of illumination at 2 Sun (Figure 5.5). For 80% r.h. conditions, PCPDTBT:PCBM degraded as little as P3HT:PCBM considering the error of the measurement. However, in synthetic air environment, we observed that Si-PCPDTBT:PCBM was the most stable, followed by PCPDTBT:PCBM and P3HT:PCBM. We made a similar observation for synthetic air and 20% r.h.

From these observations, we conclude that by changing the molecule (i.e., using

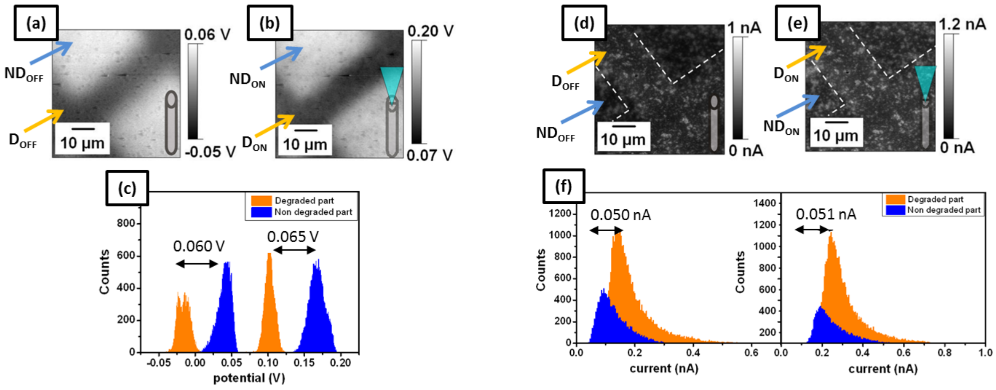

Figure 5.4: KPFM images of locally degraded Si-PCPDTBT:PCBM sample under (a) dark and (b) illumination with a 488 nm laser, (c) Histogram analysis of the KPFM images, (d) c-AFM images (bias voltage of 4 V) of locally degraded Si-PCPDTBT:PCBM sample (19hr, 2 Sun, in synthetic air) under (d) dark and (e) illumination, (f) histogram analysis of c-AFM images.

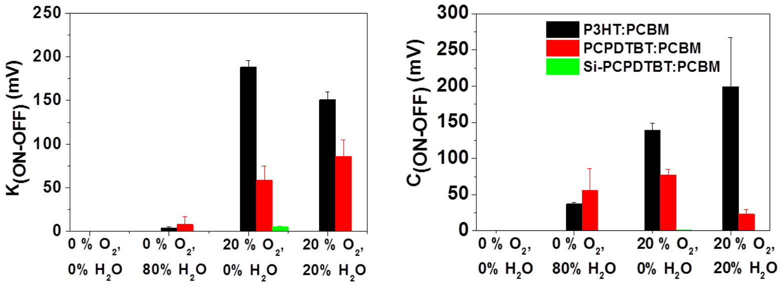

Figure 5.5: Comparison between P3HT:PCBM, PCPDTBT:PCBM and Si-PCPDTBT:PCBM blend stabilities against degradation in different environmental conditions. The P3HT:PCBM and PCPDTBT:PCBM blends were degraded for 18 h at 2 Sun and the Si-PCPDTBT:PCBM blends were degraded for 19 h at 2 Sun.

Si instead of C) at the α position to the thiophene ring makes the whole system very stable against degradation.

5.3 Summary

1. A new class of low bandgap polymers, namely PCPDTBT and Si-PCPDTBT, were blended with PCBM and studied for stability with the method as described in chapter 4.
2. In both cases, oxygen played the major role in degradation. It was observed that the PCPDTBT:PCBM blend was more stable against photo-oxidation than P3HT:PCBM.
3. Si-PCPDTBT blend was the most stable compared to the other two blends.
    a) The Si-PCPDTBT molecule acts as a radical scavenger by forming Si-O bonds, thereby leaving the π conjugated system intact, allowing charge transfer between the molecules.

6

Time resolved studies

6.1 Introduction

In chapter 3, we identified from our AFM results that on degrading the P3HT: PCBM blend, the PCBM gets oxidized first, which in turn stabilizes the P3HT. This result was then verified using the NMR techique on samples which were degraded to the same level under same degradation conditions. However, in the P3HT:PCBM system it is not possible to resolve the donor and the acceptor domains using AFM since they are blended very well. To study the degradation of the donor and acceptor domains separately in a blend, we went to a different system by using poly[2-methoxy-5-(3,7-dimethyloc-tyloxy)]-1,4-phenylene-vinylene (MDMO-PPV):PCBM which shows larger phase separation. MDMO-PPV:PCBM is a very well studied system and several groups have performed degradation studies with various techniques [100, 66, 101, 27]. However, using AFM allowed us to probe the individual components of the blend and monitor their changes in different degradation stages.

A typical topography image of the MDMO-PPV:PCBM blend spin-casted from toluene is shown in Figure 6.1. The red arrows indicate the PCBM domains and the blue arrows indicate the MDMO-PPV region. The phase separation is in the μm range and thus can be resolved very easily with AFM. The efficiency of solar cells made from these materials is relatively low because of this high phase separation, however, for the following studies they are the ideal candidate.

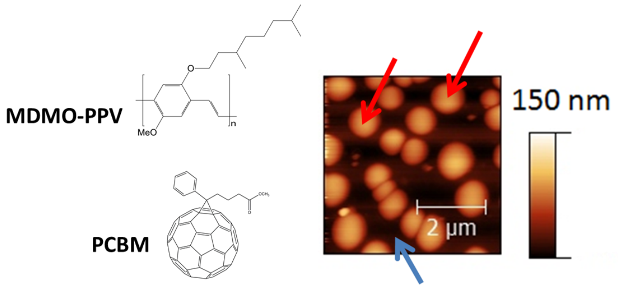

Figure 6.1: Topography image of MDMO-PPV:PCBM spin cast from toluene solution. Red arrows indicate the PCBM domains and the blue arrows indicate MDMO-PPV

Up until now all our studies on organic photovoltaic materials were done in steady state by taking the KPFM or the cAFM images in dark and then under illumination. However, the dynamic processes of charge generation and transport cannot be probed using these methods since their time resolution is not sufficient (ms). Time resolved morphological studies were performed by Paci et al. [102] where they studied the nanoscale morphology of bulk heterojunction organic solar cells using time resolved energy dispersive X-ray relfectometry in synergy with AFM analysis. They detected a reorganization of the organic molecules in the films upon illumination. In 2010, Cermak et al. [103] studied the time resolved photo-induced changes of surface potentials by KPFM. They determined these changes over short (minutes) and long (hours) time periods. Changes in the surface potential by 10-150 mV was attributed to a combination of electron accumulation, trapping and organic material degradation.

Coffey et al. [34] in 2006 came up with a new technique to measure photogenerated carrier accumulation and surface potentials in a time resolved fashion using electrostatic force microscopy (EFM). They correlated the measured EFM charge accumulation rates with external quantum efficiencies of completed devices.

In the MDMO-PPV:PCBM system, oxidation of one component should result in higher charging rates due to O_2 doping. Due to the large phase separation, we expect to observe changes in the individual components in the blend and thus, determine which component degrades faster and how the degradation of one component influences the other. In this chapter, I will discuss this method (time resolved EFM, tr-EFM) in detail and our results on the degradation of MDMO-PPV:PCBM layers after implementing this technique with our setup.

6.2 Basics of tr-EFM

The EFM technique is based on the measurement of electrostatic force gradients. The force $F(z)$ felt by the cantilever hovering at a distance z_0 above the sample can be written in a first order approximation as

$$F(z) = F(z_0) + \frac{\partial F}{\partial z(z_0)}(z - z_0) \tag{6.1}$$

In the above equation, $\partial F/\partial z(z_0)$ is the force gradient acting on the tip.

Next, we consider the tip-sample as an ideal capacitor having a capacitance of $C(z)$ with the tip surface potential V_{tip} and the sample surface potential V_{sam}. The force gradient on the tip can be expressed as

$$\frac{\partial F}{\partial z}(z_0) = \frac{1}{2}\frac{\partial^2 C}{\partial z^2}(V_{tip} - V_{sam})^2 \tag{6.2}$$

In a steady state EFM experiment, the tip is driven at its resonance frequency. When a voltage is applied between the tip and the sample, the tip-sample interactions change which in turn changes the force gradient on the cantilever. This changes the frequency at which the cantilever is vibrating at and this change is directly proportional to the force gradient as given in the equation below. The tip is maintained at resonance by changing the drive frequency.

$$\Delta f = \frac{\partial^2 C}{\partial z^2}(V_{tip} - V_{sam})^2 \tag{6.3}$$

Such a steady state EFM experiment was done on an MDMO-PPV sample spin coated from toluene. Figure 6.2 shows the cantilever frequency shift as a function of the tip voltage which was varied from -10 V to +10 V in dark and under illumination. The data points were fitted with the above equation 7.3

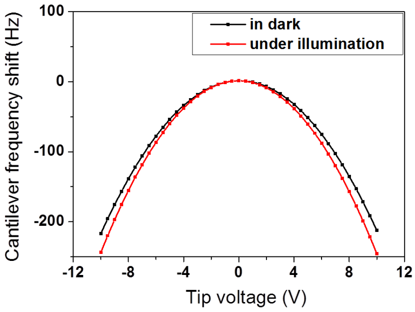

Figure 6.2: Cantilever frequency shift as a function of tip voltage in dark and under illumination

Under illumination (Figure 6.3), the charges in the active material get separated which changes the local surface potential as well as the tip-sample capacitive gradient. An increase in the tip-sample capacitive gradient is due to the movement of photogenerated charges to the film surface beneath the tip caused by the electric field at non-zero tip voltages. When there are enough charges accumulated, the tip-sample capacitor is fully charged. This stops the net charge motion and the local charge recombination balances out the charge separation. Since, $V_{tip} >> V_{sam}$, where V_{sam} depends on intensity and V_{tip} depends on the applied voltage, the total frequency shift is influenced primarily by the applied voltage and not the light intensity.

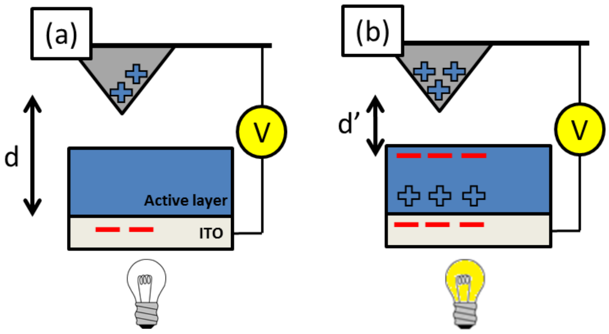

Figure 6.3: Changes in capacitance in (a) dark and (b) under illumination of the sample.

To measure the photo-induced charging of the tip-sample capacitor, the tip was kept at a distance of 50 nm above the sample surface and a +10 V bias was applied to it relative to the ITO substrate. The MFP-3D controller was used to apply this voltage to the AFM tip and also to switch on and off the laser (488 nm) to illuminate the sample. Firstly, a point scan was done in order to determine the charging rate at that point.

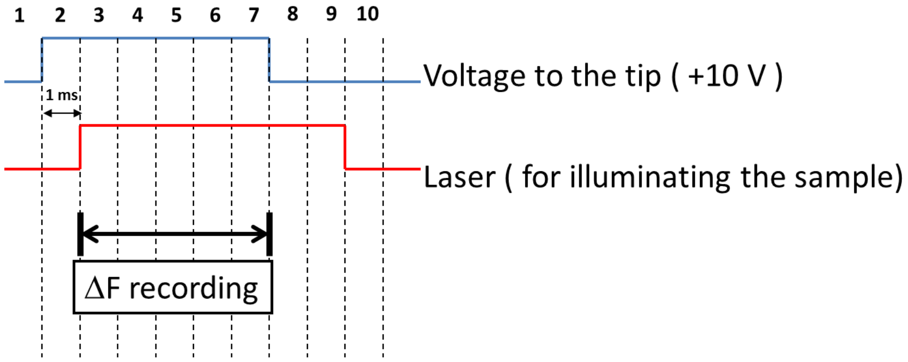

Figure 6.4: Different voltage pulses given to the tip and laser for a point scan and recording of the frequency shift

To determine the charging rate at a point, a voltage of 10 V was applied to the cantilever for 1 ms to stabilize it. In this first 1 ms, most of the charges were created due to the voltage applied to the tip and we observed an instantaneous change in the frequency shift . Afterwards, the laser was switched on for 5 ms keeping the voltage on and the frequency shift (Hz) was recorded. This frequency shift was due to the photo-generated charges and followed an exponential decay with time. Fitting this curve with an exponential function $e^{-t/\tau}$ allowed us to calculate the rate of charging (τ) of the tip-sample capacitor at that point. Then, the voltage applied to the tip was switched off while keeping the laser on for another 2 ms. This allowed the collected charges to dissipate. Figure 6.4 shows a schematic of the various voltage pulses applied to the tip and the laser with time. The changes in the frequency shift is shown in Figure 6.5 as a function of time from which we calculated the charging rate (τ).

For charging rate images, this procedure was repeated 3 times at each pixel and

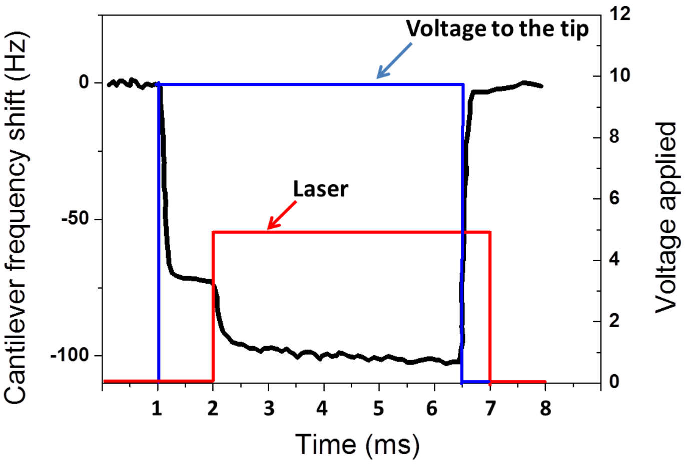

Figure 6.5: Changes in the frequency shift as a function of time with simultaneous application of voltage and light pulses

averaged. For each line, first the topography was scanned in the tapping mode and then the tip was raised 50 nm above the sample surface and the charging rate was measured following the topography.

6.3 Changes in charging rate on photo-oxidation

For an undegraded MDMO-PPV:PCBM layer, the charging rate image is shown in Figure 6.6. The charging rate of the PCBM domains is lower than the MDMO-PPV areas. In our setup, we use a 488 nm laser for illumination. MDMO-PPV has an absorption maximum at around 500 nm whereas PCBM absorbs around 20% at that wavelength. The charges formed in the polymer due to the absorption of photons are then transfered to the PCBM domains which act as the acceptor. At the donor-acceptor interface, which corresponds to the regions of fastest photoinduced charging, maximum charging rate is observed.

Next, the same sample was degraded for 2 hours in synthetic air at 2 sun. Figure 6.7a shows the charging rate of the degraded sample. In this image, we observe that the charging rate in the PCBM domains is higher than the MDMO-PPV area. This finding can be explained on the basis of oxidation of the PCBM in

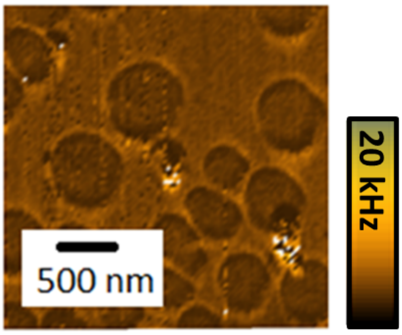

Figure 6.6: Charging rate image of undegraded MDMO-PPV:PCBM (1:4) spin coated from toluene

the blend. During the initial stages of degradation, the PCBM gets oxidized before the polymer, thereby protecting the polymer from degrading. Chambon et al. [100] concluded from IR spectroscopy studies that the presence of PCBM in MDMO-PPV films reduces the degradation kinetics of the polymer in photo-oxidation which is attributed to the scavenging effect of PCBM. Several other groups [66, 101] have reported the same which has been discussed extensively in chapter 3 with regard to PCBM and P3HT. Due to this oxygen doping, the number of charge carriers in the PCBM domains increased thereby increasing the charging rate as observed. Also, the bias at the tip drew up more carriers which added to this charging rate. At this stage of degradation, the MDMO-PPV remained unaffected from oxidation, which can also be seen if we compare Figures 6.6 and 6.7a.

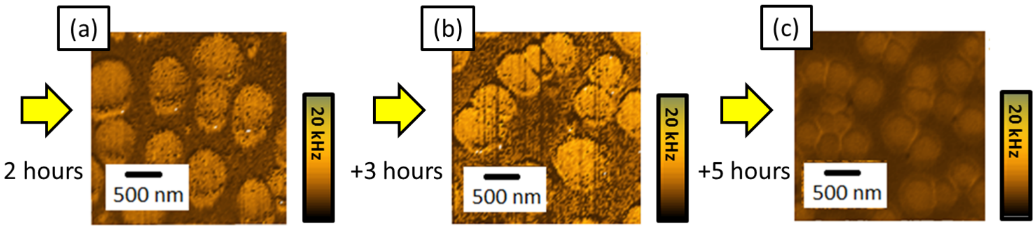

Figure 6.7: Charging rate images of MDMO-PPV:PCBM on degrading samples (2 Sun, in synthetic air) for (a) 2 hours (b) 5 hours (c) 8 hours.

On degrading the sample for 5 hours at 2 sun under same environmental conditions, it was observed that the charging rate increased even further. At this stage of degradation, the charging rate of both the PCBM as well as the MDMO-PPV areas increased. This increase indicated that oxidation takes place for both the donor as well as the acceptor molecules. This finding is in accordance to the studies performed by Chambon et al. [100] where they observed simultaneous degradation of MDMO-PPV and PCBM after 10 hours of irradiation in ambient environment.

On degrading the samples for longer times (8 hours, 2 sun, synthetic air), the overall charging rate of the active layer went down (Figure 6.7c). The decrease in the charging rate happens when both the donor and acceptor chains get fragmented and hence, there is very little charging.

6.4 Topography changes on degradation

In addition, the swelling and collapse of the individual components due to oxidation and fragmentation respectively, were determined from the topography images. A line profile was made through the PCBM domains (Figure 6.8a,b). The difference in the PCBM and the MDMO-PPV height was recorded (Δx) (Figure 6.8c). For an undegraded sample, this difference was 81 nm. The difference increased to 133 nm when exposed to oxygen in the presence of light for 2 hours. This indicated swelling of the PCBM domain due to incorporation of oxygen (as discussed in chapter 3). After 5 hours of photo-oxidation, the domains start collapsing due to fragmentation, thereby, decreasing the difference Δx.

6.5 Summary

1. A different system (MDMO-PPV:PCBM) having a larger phase separation was studied using trEFM. The large phase separation between the donor and the acceptor domains within the blend allowed us to analyse both the components individually, and their effect upon each other on degradation.

2. TrEFM gave us the charging rates of the sample on illumination. The rates

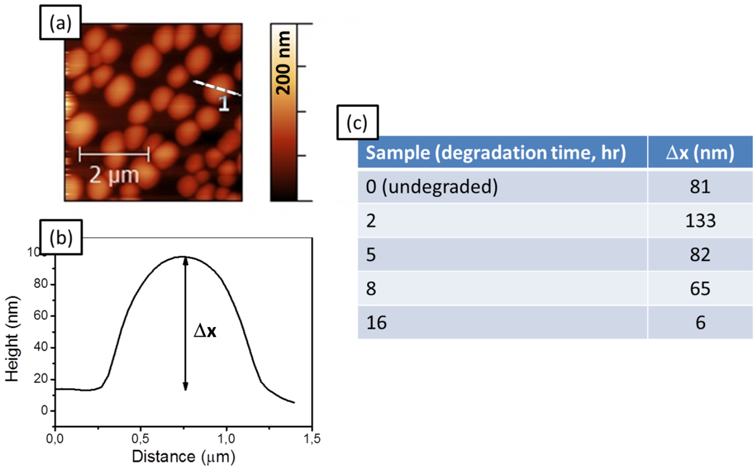

Sample (degradation time, hr)	Δx (nm)
0 (undegraded)	81
2	133
5	82
8	65
16	6

Figure 6.8: (a) Topography image of MDMO-PPV:PCBM blend (b) Line profile through PCBM domain [shown by white line in (a)] (c) Changes in height of PCBM domains on degradation

were determined by calculating the charging up of the capacitor formed between the tip and the sample.

3. For non-degraded samples, a lower charging was observed for PCBM compared to MDMO-PPV. This was attributed to the less number of charges created in the acceptor phase than the donor.

4. On degrading the sample in the presence of oxygen and light, the PCBM domains got oxidized. This increased the number of charge carriers and resulted in a faster charging of the capacitor.

5. At later stages of degradation, the charging rates of both the donor and acceptor domains went down indicating fragmentation of the chains and hence irreversible degradation.

6. From this chapter we conclude that in a blend, the PCBM gets oxidized thereby acting as a radical scavenger and protecting the polymer in the early stages of degradation. This is also in good agreement with our previous studies.

7

KPFM in liquids

7.1 Introduction

In the previous chapters, I discussed the use of the electrical modes of AFM to characterize polymer-fullerene solar cells. These measurements were done in N_2 environment which might have a lot of unknown impurities. This may result in contamination of the tip and the sample surface which may then change the measured values. To avoid this issue we took relative measurements by always taking the difference between degraded and non-degraded parts. Another approach would be perform the experiments in cleaner environments, like liquids. Measurements in liquids ensure the removal of water and other organic adsorbates from the surface and the tip thereby reducing shielding effects. In the following work, we used electrically insulating liquids which allowed us to perform standard KPFM without the risk of spurious forces acting on the tip. As a proof of principle, we investigated the effect of hexadecanethiol adsorption from decane on the work function of Au substrate.

Establishment of this method will enable us to do in-situ measurements of the modification of work functions of metal electrodes which is attractive for optoelectronic devices such as organic solar cells [104, 105, 106] or light-emitting diodes. A control of band alignment between a metal electrode and an organic semiconductor is crucial for the performance of organic solar cell devices. Earlier studies also show that on changing the surface energy of a buffer layer, on top of which a photoactive layer is formed, increases the efficiency and the photocurrent of the solar cells. Bulliard et al. [104] investigated this effect by controlling the surface energy of a zinc oxide (ZnO) buffer layer on top of which a polymer-fullerene derivative bulk heterojunction was formed. They saw an increase in efficiency from 3.27% to 3.70%. This improvement was attributed to (i) a better alignment of the lowest unoccupied molecular orbital (LUMO) level of the ZnO layer to the LUMO level of the photoactive layer (Figure 7.1) and to (ii) a better morphology of the photoactive layer. The control of the surface energy was done by incorporating a mixed self assembled monolayer (SAM) in between ZnO and the photoactive layer. The mixed SAMs were prepared by dipping the ZnO thin film in an anhydrous toluene solution containing aminopropyltrimethoxysilane and octyltrimethoxysilane in different molar ratios.

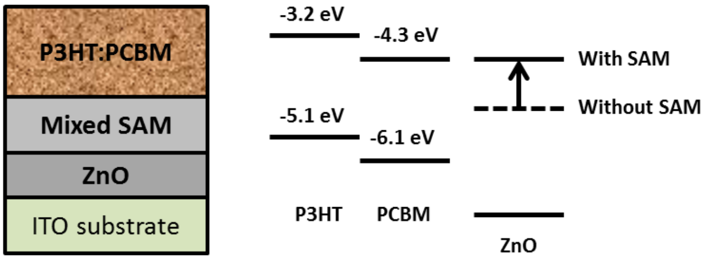

Figure 7.1: Schematic of device with a layer of mixed SAM along with the energy level diagram showing the change in work function of the ZnO layer [104].

The first KPFM measurements on SAMs were reported by Lü and coworkers [107] in dry nitrogen atmosphere. Monolayers of alkanethiols with chemically different terminal ω-groups on an Au substrate were studied. The surface potential difference between regions of hexadecanethiols and mercaptohexadecanoic acid molecules was reported to be 0.4 eV. The self-assembly of alkanethiols to monolayers from different solvents and for different substrates has been studied extensively [108, 109]. In particular, the molecular order on Au(111) surfaces is known in detail [110]. Furthermore, the work functions of alkanethiol monolayers are well known for solid-gas interfaces, as measured, for example, by de Boer and coworkers using Kelvin probe [111] in N_2 gas environment or by Alloways and coworkers with ultra-violet photoemission spectroscopy (UPS) [112] in ultra-high vacuum. The methods revealed a decrease in work function of $\Delta\Phi$ = -0.8 eV and $\Delta\Phi$ = -1.35 eV respectively upon formation of a hexadecanethiol monolayer on clean Au surfaces. The latter value is consistent with the work function shifts obtained by theoretical calculations [113, 114].

In liquids, additional contributions to the CPD from the physisorbed liquid and subsequent chemisorption of molecules to the AFM tip and the sample surface have to be taken into account. For inferring the work function shift of Au coated with a monolayer of alkanethiols from the measured CPD is based on taking the AFM tip as reference surface (constant tip work function). Here, only the Au surface is exposed to the alkanethiol solution whereas the AFM tip is kept ex-situ to prevent adsorption of alkanethiols. This is important because the KPFM is a relative technique as already discussed in chapters 2,3.

7.2 Experimental section

7.2.1 Preparation of Au substrates

For the study of the self-assembly of alkanethiols on Au(111) by KPFM in decane, we used commercial Au substrates (Arrandee, 11×11 mm, glue free type). These substrates were made on a borosilicate glass by deposition of 2.5 nm ± 1.5 nm Cr as adhesion layer followed by 250 nm ± 50 nm of Au. In order to obtain 100 nm × 100 nm large islands of Au(111) on the surface, the Au substrates were flame annealed with a butane flame until the Au glowed with a reddish color. Afterwards, they were allowed to cool down for around 40 s on a copper plate. This procedure was repeated for three times. The substrates were cleaned with plenty of ethanol, dried under nitrogen flow and directly used afterwards.

7.2.2 KPFM measurements

The KPFM measurements were performed on a Bruker MultiMode (NanoScope IIIa controller, extender box). For the measurements in decane, we used a standard liquid cell which was modified for KPFM measurements with an electrical connection to the cantilever (Figure 7.2). We used conductive Pt/Ir coated cantilevers (Nanosensors PPP-EFM, nominal vertical resonance frequency of 70 kHz). The measurement in decane led to a damping of the amplitude of the cantilever and thus to a reduced Q factor. As the measured contact potential difference depends on the distance between tip and the sample surface, it was crucial to perform all measurements and calibrations at the same lift height. Thus, we performed all the measurements at a lift height of 5 nm and applied an AC voltage of 3 V to the AFM tip. The decane ($\geq$ 99% for synthesis, Merck) was dried with molecular sieve (4A, 8 to 12 mesh, Acros Organics) and degassed in an ultrasonic bath for approx. 10 min before its insertion into the liquid cell.

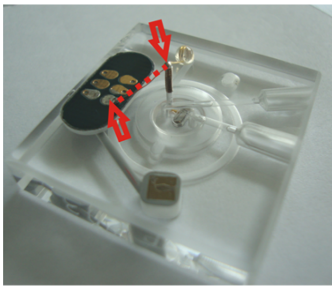

Figure 7.2: Image of the liquid cell used for KPFM: a copper wire was soldered from one pin to the clamp that holds the cantilever (red arrows).

For the investigation of the work function shift in decane upon hexadecanethiol adsorption on the Au samples, we first calibrated the Pt/Ir coated AFM tip on freshly cleaved highly ordered pyrolytic graphite (HOPG) in air. The work function of AFM tip can be determined by using the following equation

$$CPD = \frac{\Delta\Phi}{e} = \frac{(\Phi_{tip} - \Phi_{sample})}{e} \tag{7.1}$$

which is valid for the case that the AC potential is applied to the cantilever. Here, e is the elementary charge. A solution of hexadecanethiols (Aldrich, 92%) in decane with a concentration of $c = 4.45 \times 10^{-2}$ mol/l was used.

7.3 Results and Discussion

The work functions of the Pt/Ir coated tip and Au sample, involved in this KPFM measurement are outlined in an energy level diagram (Figure 7.3). The Pt and the Au materials are characterized by their respective Fermi levels ($E_{F,Pt}$ and $E_{F,Au}$), their vacuum level close to the surface ($E_{Vac,s}$) and the vacuum level at infinite distance from the surface ($E_{Vac,\infty}$). As the AFM tip and the Au sample are electrically connected and a DC bias is applied to compensate for their contact potential difference, the Fermi levels remain at their original energies whereas the vacuum levels ($E_{Vac,s}$) align at the same energy. The work function of the respective material is defined as the difference between their Fermi and the vacuum levels. The work function $\Phi_{Au,air}$ of the Au surface in ambient air is calculated by

$$\Phi_{Au,air} = \Phi_{tip,air} - eCPD_{Au,air} \tag{7.2}$$

Upon filling decane into the liquid cell (Figure 7.3c) both the AFM tip and sample are immersed. Undefined adsorbates such as hydrocarbons and water on the surface (Figure 7.3a, green ellipsoids) are dissolved and thus are removed from the surface. In addition, several studies demonstrated that decane interacts with noble metal surfaces like Au and Pt. For example, Uosaki and coworkers showed by in-situ scanning tunneling microscopy (STM) measurements that even numbered alkanes, like hexadecane, physisorb on Au(111) with their molecular axis parallel to one of the crystalline orientations [115]. Owing to this physisorption the HOMO (H) and LUMO (L) levels of the decane molecules need to be considered for both the Pt and the Au surface in the corresponding energy level diagram (Figure 7.3d, levels in blue). According to Koch [116], this weak interaction between organic molecules and the metal surface leads to a reduced metal work function due to the so-called " push-back effect ". The electron density of a metal surface is shifted inside the metal upon contact with organic molecules due to Pauli repulsion between the electron orbitals of the solvent molecules and the metal surface. This reduction of the so-called surface dipole [117] leads to a decrease in the vacuum level close to the metal surface ($E_{Vac,s}$ in Figure 7.3d) by

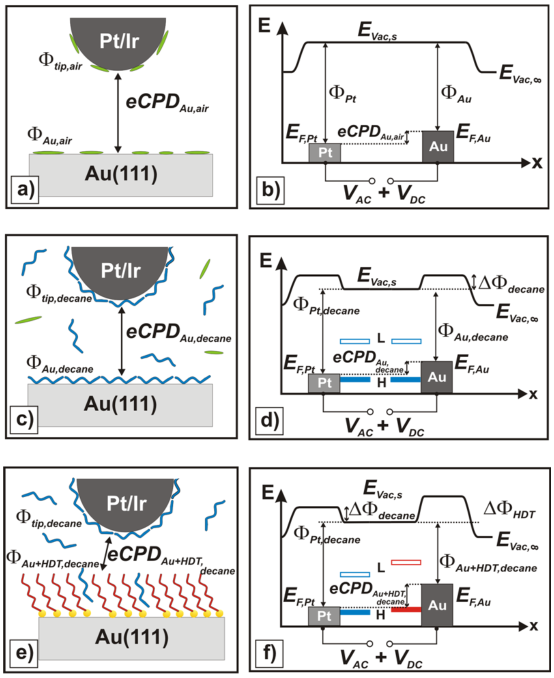

Figure 7.3: Scheme of the experimental setups and their corresponding energy diagrams: (a) KPFM measurement in ambient air. (b) Energy diagram for the KPFM measurement in ambient air. (c) KPFM measurement in decane. Decane molecules are indicated in blue. (d) Energy diagram for the KPFM measurement in decane. (e) KPFM measurement on hexadecanethiol monolayer on Au(111) in decane. Hexadecanthiol molecule (alkyl chain in red, sulfur atom in yellow) chemisorb on Au(111) surface. (f) Energy diagram for the KPFM measurement on a layer of hexadecanthiols in decane.

$\Delta\Phi_{decane}$ and thus to a decreased metal work function for both the Pt tip material and the Au surface. Assuming that the effect of decane is approximately the same for Pt and Au surfaces and that identical adsorbates are present at the surfaces in air, we should obtain the same eCPD value for the measurement in decane as for the one in air, i.e. $eCPD_{air} \approx eCPD_{decane}$. Ito and coworkers [118] determined a work function shift of $\Delta\Phi = -0.7$ eV for the physisorption of tetratetracontane ($C_{44}H_{90}$) on Au by UPS. Using this value we can determine the AFM tip work function in decane $\Phi_{tip,decane}$ by

$$\Phi_{tip,decane} = \Phi_{tip,air} + \Delta\Phi_{decane} \tag{7.3}$$

In analogy, the work function of the Au surface in decane $\Phi_{Au,decane}$ is obtained by

$$\Phi_{Au,decane} = \Phi_{tip,decane} - eCPD_{Au,decane} \tag{7.4}$$

As mentioned before, the above consideration is only valid for the same amount of water and other hydrocarbons (green ellipsoids, Figure 7.3a) adsorbed on both the AFM tip and the sample surface during the measurement in air. According to the studies of Sugimura and coworkers [119], an adsorbed water layer can shield the recorded CPD due to the orientation of dipole moments of the water molecules at the surface. This shielding effect results in a lower CPD than the one of a clean surface. A mole fraction of water of $x_{water} = 0.54 \times 10^{-3}$ can be dissolved in decane [120]. In our case it is very likely that the AFM tip and the sample surfaces are covered by different amounts of diverse adsorbates. Hence, the removal of water and hydrocarbons from the surfaces by filling decane into the liquid cell and the subsequent physisorption of different amounts of decane leads to a difference in the measured CPDs in air and decane. The effect of the unspecific adsorbates, in particular of water, can be obtained by

$$\Delta\Phi_{H_2O} = eCPD_{Au,air} - eCPD_{Au,decane} \tag{7.5}$$

In order to ascribe a contact potential difference during the chemical reaction of alkanethiols to a work function of the measured surface it is crucial that either the work function of the AFM tip or the sample surface remains constant or is known throughout the reaction as both parts contribute to the measured CPD.

In our case, we use the AFM tip as a reference surface, keeping the tip work function constant. Chemisorption of the alkanethiols to the AFM tip can be avoided by exposing only the Au surface to the alkanethiol solution.

7.3.1 Constant tip work function

The physisorbed decane molecules on the Au surface are replaced by chemisorbed hexadecanethiol molecules whereas the surface of the AFM tip remains covered by decane molecules (Fig. 7.3e). Hence, only the chemisorbed alkanethiol molecules need to be considered for determining the work function of the Au ($\Phi_{Au+HDT,decane}$). In general, the chemisorbed alkanethiols on a metal substrate can be considered as a layer of dipoles. In this layer the negative charges are situated at the metal/sulfur interface and the positive charges face decane. Zehner and coworkers [121] described the layer of alkanethiols as consisting of two internal dipole moments which are located at the two interfaces and are stacked on top of each other. The intrinsic dipole at the metal-sulfur interface is caused by the charge-transfer interaction and depends therefore also on the nature of the metal. The second dipole along the alkanethiol molecules is solely determined by the composition of the monolayer, i.e., the length of the alkyl chain and its ω-terminating group. For hexadecanethiols the electropositive alkyl chain leads to a decrease in the surface potential and thus to a shift of the vacuum level towards lower energies as depicted in the corresponding energy level diagram (Figure 7.3f). The HOMO and LUMO levels of the alkanethiols (Figure 7.3f, levels in red) have a lower energy compared to the ones of the decane molecules. The vacuum level close to the Au surface is further decreased which results in a lower work function of the Au owing to the chemisorption of the alkanethiols. As a result, the measured CPD is increased and $eCPD_{decane+HDT} > eCPD_{decane}$. The work function of the Au surface after exposure to alkanethiols can be calculated by

$$\Phi_{Au+HDT,decane} = \Phi_{tip,decane} - eCPD_{Au+HDT,decane} \tag{7.6}$$

The work function shift of the Au surface due to chemisorption of the alkanethiols is then given by

$$\Delta\Phi_{Au+HDT,decane-Au,air} = \Phi_{Au+HDT,decane} - \Phi_{Au,air} \tag{7.7}$$

By inserting equations 7.2 and 7.6 into equation 7.7, we can write

$$\Delta\Phi_{Au+HDT,decane-Au,air} = eCPD_{Au,air} - eCPD_{Au+HDT,decane} + \Delta\Phi_{decane} \quad (7.8)$$

Equation 7.8 allows us to calculate $\Delta\Phi_{Au+HDT,decane-Au,air}$ from measured or otherwise unknown values and it does not depend anymore on a calibration of the AFM tip coating.

7.3.2 Experimental realization

Measurements were carried out on Au(111). First, the contact potential difference was measured in ambient air at 60% relative humidity and in pure decane. In a second step, the Au(111) sample was immersed into a 1.6 wt% solution (c = 4.45 × $10^{-2} mol/l$) of hexadecanethiols (HDT) in decane for 35 h at room temperature. Afterwards, the Au(111) surface was carefully rinsed with pure decane. The CPDs measured in different environments are displayed in Table 1. The error was obtained by measuring at three different positions on the sample and calculating the standard deviation of all measured data points ($\geq$ 60000).

The shift in work function from the Au(111) in air to the HDT exposed Au in decane was determined with equation 7.8: $\Delta\Phi_{Au+HDT,decane-Au,ambient} = -1.33eV \pm 0.07eV$. Here, $\Delta\Phi_{decane}$ was taken from the literature as -0.7 eV.33 The measured shift of the work function of the adsorption of hexadecanethiols on the Au surface is in excellent agreement with the value ($\Delta\Phi = -1.35$ eV) reported by Alloway and coworkers determined from UPS measurements in UHV [112]. In analogy to our above considerations, we can calculate the work function of Au(111) from the CPDs measured in different environments (Table 1) by using equations 7.2, 7.4, and 7.8. Furthermore, the tip work functions in air and decane were determined to be $\Phi_{tip,air}$ = (4.76 ± 0.01) eV and $\Phi_{tip,decane} = \Phi_{tip,air} + \Delta\Phi_{decane} = 4.06eV \pm 0.01eV$.

For a visual representation of the data we plotted all work functions ($\Phi_{Au,air}$, $\Phi_{Au,decane}$, $\Phi_{Au+HDT,decane}$) in a histogram (Figure 7.4). The work functions for the measurement in air and in decane are clearly separated. The work function

	Measurement on Au ($eCPD_{Au}$, eV)	Work function of AFM tip (Φ_{tip}, eV)	Work function of Au (Φ_{Au}, eV)
air	0.020 ± 0.004	4.76 ± 0.01	4.74 ± 0.01
decane	-0.200 ± 0.004	4.06 ± 0.01	4.26 ± 0.01
HDT, decane	0.65 ± 0.02	4.06 ± 0.01	3.41 ± 0.02

Table 7.1: CPDs of Au(111) measured in different environments and the corresponding work functions calculated by using equation 7.8

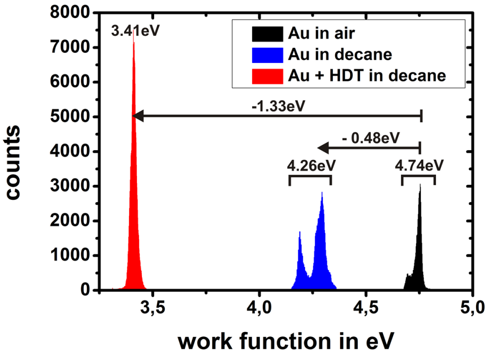

Figure 7.4: Histogram of work function of the KPFM measurement on untreated Au(111) surface in air (black), in decane (blue) and on the Au surface with an adsorbed monolayer of HDT in decane (red). Upon immersion in decane the work function of the untreated Au shifted by $\Delta\Phi_{Au,air-Au,decane}$= -0.48 eV ± 0.01 eV to lower values. The adsorption of hexadecanethiols onto the Au resulted in a work function shift of $\Delta\Phi_{Au+HDT,decane-Au,air}$ = -1.33 eV ± 0.07 eV.

shift of $\Delta\Phi_{Au,decane-Au,air} = -0.48eV \pm 0.01eV$ is less than the theoretically predicted work function shift of $\Delta\Phi_{decane}$ = -0.7 eV for physisorbed decane on Au(111). However, we ascribe this difference of $\Delta\Phi_{H_2O} = 0.22eV \pm 0.01eV$ to the presence different densities of water and hydrocarbons on the AFM tip and Au(111) surface in air that are removed upon insertion of decane. Similar differences were reported for UPS measurements on Au surfaces that were exposed to air before being measured [122].

7.4 Summary

1. In order to avoid the effect of organic adsorbates on the surface or the tip and to get a clean environments, KPFM experiments were performed in liquids.
2. Electrically insulating liquid (decane) was used that allowed us to perform standard KPFM without the risk of spurious forces acting on the tip.
3. This technique was verified by measuring the work function shift of an Au substrate upon hexadecanethiol adsorption.
4. Performing the experiment in decane and measuring the work function shift of Au allowed us to estimate the effect of the water layer present during a KPFM measurement in air.
5. Furthermore, this technique was used to monitor in situ chemical reactions and their effect on the work function of the surface.
6. The obtained work function differences were in excellent agreement with the literature values reported from UPS studies.
7. This method will enable us to do in situ measurements of the modification of work functions of metal electrodes which will be very attractive for opto-electronic studies in the future.

8

Concluding remarks and outlook

In the present work, I studied the degradation of the active organic solar cell materials namely, polymers and fullerenes using different AFM techniques (such as KPFM and cAFM), as well as NMR and UV-Vis spectroscopy. Using these experimental methods it has been possible to investigate degradation of the individual components of the active material and compare them with the degradation of the blend. The measured CPD and surface conductivity with KPFM and c-AFM have been found to be correlated with the device characteristics, i.e. open circuit voltage and short circuit current. The ability of AFM to measure these parameters locally makes our method of characterization very unique since it correlates the local characteristics of the active materials to the bulk properties of the device. This eliminates the need to make fully functional devices saving time and engineering efforts. Also, it allows us to exclude the influence of other layers, e.g., electron transport layers, on the degradation of the active layer. This method has been used, to the best of our knowledge, for systematic studies of degradation of various new low bandgap materials for the first time.

Photo-induced electron transfer processes take place over a time scale of 50-100 fs [4], which dominate over all other photo-physical processes. The time resolution of KPFM is much slower making it a steady state experiment, which therefore, allows us to probe the HOMO levels of the active materials. An early stage of degradation (photon dose ≤ 0.36 kJ/cm^2) causes changes in the energy levels of the polymer due to the formation of charge-transfer-complexes with oxygen. This results in changes in the electrical properties of the solar cell devices. The contact potential difference (CPD) measured between the tip and the sample, comes from a combination of the charges present in the HOMO levels of the donor and the acceptor materials. The presence of electrons decreases the CPD, whereas, the presence of holes increases it. The KPFM technique allows us to probe extremely small changes of the order of meV in the energy levels of the material during degradation. These shifts (7 meV) can further be correlated with the increase in the charge carrier concentration in the active layer due to oxygen doping which has been verified with our c-AFM measurements. Illumination of the sample results in photo generation of the charges in the system that leave the surface enriched with holes as seen by an overall increase of 0.2 eV in the CPD. This stage of degradation results in no change in topography and the formation of the above mentioned charge-transfer complex is reversible upon annealing. Therefore, from the KPFM data, it is possible to deduce the energy levels of the degraded and non-degraded samples explaining the various shifts in the HOMO levels of the individual components in the blend. This gives us better understanding of the physics of the organic solar cells.

A later stage of degradation (photon dose ≥ 2 kJ/cm^2) arises from chemical interactions between the oxygen and the active material in presence of light. This degradation is irreversible and not only changes the electrical properties but also results in changes of the morphology. From our measurements, it has been possible to identify two competing processes that take place inside a blend. Photo-oxidation of PCBM (acceptor) results in an increase of the volume due to the incorporation of oxygen after which, fragmentation of the both PCBM and P3HT (donor) results in the collapse of the layer as observed by topography measurements. NMR and UV-Vis spectroscopy measurements have confirmed the chemical changes occurring in these materials and further elucidated the above results.

Time resolved EFM (tr-EFM) enabled us to study the dynamic processes, such as, the rate of charging of the active layer on illumination. The time resolution of this method (100 μs) is limited by the vertical resonance frequency of the cantilever and the bandwidth of the feedback circuit. Therefore, currently it is only possible to do time resolved measurements on comparatively less efficient samples (MDMO-PPV: PCBM). The low efficiency of this blend results from the large phase separation between the donor and the acceptor components. This large phase separation proved advantageous since it allowed us to investigate the degradation of individual components separately within the blends. Other characterization techniques like XPS, NMR etc. probe the bulk properties of the materials and cannot resolve the individual components within the blend. This makes our method of characterization ideal for investigating such samples.

Early signs of degradation of these blends show an increase in the charging rate of PCBM domains. This increase was attributed to the oxygen scavenging role of the PCBM in the blend which protects the polymer from degradation. However, it does not completely prevent photo-oxidation. Incorporation of additional radical scavenging additives would further improve the stability of these materials. 3-hydroxyflavone is one such free-radical scavenging agent that not only improves the stability but also enhances the efficiency of P3HT: PCBM based organic solar cells due to improved carrier mobility [123].

It would be possible to improve the time resolution of the tr-EFM technique by using more sophisticated feedback controls. However, any feedback system would ultimately face a signal-to-noise stability limit. It has been demonstrated recently [124], that with a feedback free approach it is possible to reach a time resolution of 100-200 ns. Implementation of this method would allow us to investigate fast local changes on degradation, such as the carrier dynamics of highly efficient sample materials having optimum morphology.

Other than the morphology of the active layer, the performance of any organic semiconductor depends on the band alignment between the electrodes and the active material. Therefore, modification of the work function of the electrode has been attractive for opto-electronic devices. The self-assembly of organic molecules in monolayers induces an alignment of their molecular dipole moment and results in a change in their surface work function of the underlying metal. Establishing KPFM in liquids enabled us to do in-situ measurements of the modification of the work function of Au substrate upon hexadecanethiol adsorption from decane. In addition, measurements in liquids ensure the removal of water and other organic adsorbents from the surface, thereby, reducing shielding effects. It also bears the advantage of topographic imaging of the surface in liquids with reduced tip-sample forces. Therefore, sensitive molecules and soft interfaces are accessible to the KPFM also. This method opens up new possibilities such as measurements of Graetzel cells [125] (or dye-sensitized solar cells) with KPFM.

From all the above studies, we now have a better understanding of the different stages and processes of degradation of active materials in an organic photovoltaic device. Furthermore, the possibility to record electrical parameters at the nm scale makes the AFM method unique for studying nanoscale morphology, their interfaces and the related degradation effects. This method can also be used to study the cross-sections of entire solar cell devices which will give information about the various processes occurring in each layer individually and how the degradation of each layer would affect the other layers. Finally, having a better understanding of the degradation processes and how they change the energy levels and the molecular structures will help us design more stable photovoltaic devices leading to a bright and sunny future.

Bibliography

[1] Kasap and Capper, editors. *Springer Handbook of Electronic and Photonic Materials*. Springer.

[2] D. M. Chapin, C. S. Fuller, and G. L. Pearson. A new silicon p-n junction photocell for converting solar radiation into electrical power. *Journal of Applied Physics*, 25(5):676–677, 1954.

[3] Hideki Shirakawa, Edwin J. Louis, Alan G. MacDiarmid, Chwan K. Chiang, and Alan J. Heeger. Synthesis of electrically conducting organic polymers: halogen derivatives of polyacetylene, (ch). *J. Chem. Soc., Chem. Commun.*, (16):578–580, 1977.

[4] Li Gang, Zhu Rui, and Yang Yang. Polymer solar cells. *Nature Photonics*, 6:153–161, 2012.

[5] D. L. Staebler and C. R. Wronski. Reversible conductivity changes in discharge-produced amorphous si. *Applied Physics Letters*, 31(4):292–294, 1977.

[6] G. Yu, C. Zhang, and A. J. Heeger. Dual-function semiconducting polymer devices: Light-emitting and photodetecting diodes. *Applied Physics Letters*, 64(12):1540–1542, 1994.

[7] Frederik C. Krebs and Holger Spanggaard. Significant improvement of polymer solar cell stability. *Chemistry of Materials*, 17(21):5235–5237, 2005.

[8] C. W. Tang. Two-layer organic photovoltaic cell. *Applied Physics Letters*, 48(2):183–185, 1986.

[9] Harald Hoppe and N. Sariciftci. Polymer solar cells. In Seth Marder and Kwang-Sup Lee, editors, *Photoresponsive Polymers II*, volume 214 of *Advances in Polymer Science*, pages 1–86. Springer Berlin / Heidelberg, 2008. 10.1007/122007121.

[10] I. H. Campbell, T. W. Hagler, D. L. Smith, and J. P. Ferraris. Direct measurement of conjugated polymer electronic excitation energies using metal/polymer/metal structures. *Phys. Rev. Lett.*, 76:1900–1903, Mar 1996.

[11] Jean-Luc Bredas, Jerome Cornil, and Alan J. Heeger. The exciton binding energy in luminescent conjugated polymers. *Advanced Materials*, 8(5):447–452, 1996.

[12] Ian A. Howard and Frederic Laquai. Optical probes of charge generation and recombination in bulk heterojunction organic solar cells. *Macromolecular Chemistry and Physics*, 211(19):2063–2070, 2010.

[13] Brian A. Gregg. Excitonic solar cells. *The Journal of Physical Chemistry B*, 107(20):4688–4698, 2003.

[14] Brian A. Gregg and Mark C. Hanna. Comparing organic to inorganic photovoltaic cells: Theory, experiment, and simulation. *Journal of Applied Physics*, 93(6):3605–3614, 2003.

[15] Xiaoniu Yang, Joachim Loos, Sjoerd C. Veenstra, Wiljan J. H. Verhees, Martijn M. Wienk, Jan M. Kroon, Matthias A. J. Michels, and Rene A. J. Janssen. Nanoscale morphology of high-performance polymer solar cells. *Nano Letters*, 5(4):579–583, 2005.

[16] Sean E. Shaheen, Christoph J. Brabec, N. Serdar Sariciftci, Franz Padinger, Thomas Fromherz, and Jan C. Hummelen. 2.5 *Applied Physics Letters*, 78(6):841–843, 2001.

[17] Mikkel Joergensen, Kion Norrman, and Frederik C. Krebs. Stability/degradation of polymer solar cells. *Solar Energy Materials and Solar Cells*, 92(7):686–714, July 2008.

[18] Andrea Seemann, H.-J. Egelhaaf, Christoph J. Brabec, and Jens A. Hauch. Influence of oxygen on semi-transparent organic solar cells with gas permeable electrodes. *Organic Electronics*, 10(8):1424 – 1428, 2009.

[19] Andrea Seemann, Tobias Sauermann, Christoph Lungenschmied, Oskar Armbruster, Siegfried Bauer, H.-J. Egelhaaf, and Jens Hauch. Reversible and irreversible degradation of organic solar cell performance by oxygen. *Solar Energy*, 85(6):1238 – 1249, 2011. Organic photovoltaics and dye sensitized solar cells.

[20] L. Luer, H.-J. Egelhaaf, D. Oelkrug, G. Cerullo, G. Lanzani, B.-H. Huisman, and D. de Leeuw. Oxygen-induced quenching of photoexcited states in polythiophene films. *Organic Electronics*, 5(1-3):83 – 89, 2004. Current Trends in Crystalline Organic Semiconductors: Growth Modelling and Fundamental Properties.

[21] Julia Schafferhans, Andreas Baumann, Alexander Wagenpfahl, Carsten Deibel, and Vladimir Dyakonov. Oxygen doping of p3ht:pcbm blends: Influence on trap states, charge carrier mobility and solar cell performance. *Organic Electronics*, 11(10):1693 – 1700, 2010.

[22] Matthieu Manceau, Agnes Rivaton, Jean-Luc Gardette, Stephane Guillerez, and Noella Lemaitre. The mechanism of photo- and thermooxidation of poly(3-hexylthiophene) (p3ht) reconsidered. *Polymer Degradation and Stability*, 94(6):898 – 907, 2009.

[23] Libor Juha, Vera Hamplova, Jarmila Kodymova, and Otomar Spalek. Reactivity of fullerenes with chemically generated singlet oxygen. *J. Chem. Soc., Chem. Commun.*, (21):2437–2438, 1994.

[24] Kathleen M. Creegan, John L. Robbins, Win K. Robbins, John M. Millar, Rexford D. Sherwood, Paul J. Tindall, Donald M. Cox, John P. McCauley, and David R. and Jones. Synthesis and characterization of c60o, the first

fullerene epoxide. *Journal of the American Chemical Society*, 114(3):1103–1105, 1992.

[25] C. Taliani, G. Ruani, R. Zamboni, R. Danieli, S. Rossini, V. N. Denisov, V. M. Burlakov, F. Negri, G. Orlandi, and F. Zerbetto. Light-induced oxygen incision of c60. *J. Chem. Soc., Chem. Commun.*, (3):220–222, 1993.

[26] Mark Dante, Jeffrey Peet, and Thuc-Quyen Nguyen. Nanoscale charge transport and internal structure of bulk heterojunction conjugated polymer/fullerene solar cells by scanning probe microscopy. *The Journal of Physical Chemistry C*, 112(18):7241–7249, 2008.

[27] Xiaoniu Yang, Jeroen K. J. van Duren, Rene A. J. Janssen, Matthias A. J. Michels, and Joachim Loos. Morphology and thermal stability of the active layer in poly(p-phenylenevinylene)/methanofullerene plastic photovoltaic devices. *Macromolecules*, 37(6):2151–2158, 2004.

[28] R. Joseph Kline, Michael D. McGehee, Ekaterina N. Kadnikova, Jinsong Liu, Jean M. J. Frechet, and Michael F. Toney. Dependence of regioregular poly(3-hexylthiophene) film morphology and field-effect mobility on molecular weight. *Macromolecules*, 38(8):3312–3319, 2005.

[29] H. Yamada, T. Fukuma, K. Umeda, K. Kobayashi, and K. Matsushige. Local structures and electrical properties of organic molecular films investigated by non-contact atomic force microscopy. *Applied Surface Science*, 188:391 – 398, 2002. Proceedings of the 4th International Conference on Noncontact Atomic Microscopy¿.

[30] A. Alexeev, J. Loos, and M.M. Koetse. Nanoscale electrical characterization of semiconducting polymer blends by conductive atomic force microscopy (c-afm). *Ultramicroscopy*, 106(3):191 – 199, 2006.

[31] Liam S. C. Pingree, Obadiah G. Reid, and David S. Ginger. Electrical scanning probe microscopy on active organic electronic devices. *Advanced Materials*, 21(1):19–28, 2009.

[32] David C. Coffey, Obadiah G. Reid, Deanna B. Rodovsky, Glenn P. Bartholomew, and David S. Ginger. Mapping local photocurrents in poly-

mer/fullerene solar cells with photoconductive atomic force microscopy. *Nano Letters*, 7(3):738–744, 2007.

[33] Daniel A. Kamkar, Mingfeng Wang, Fred Wudl, and Thuc-Quyen Nguyen. Single nanowire opv properties of a fullerene-capped p3ht dyad investigated using conductive and photoconductive afm. *ACS Nano*, 6(2):1149–1157, 2012.

[34] David C. Coffey and David S. Ginger. Time-resolved electrostatic force microscopy of polymer solar cells. *Nat Mater*, 5(9):735–740, September 2006.

[35] E. Lopez-Elvira, E. Escasain, A. Baro, J. Colchero, and E. Palacios-Lidon. Wavelength dependence of nanoscale photodegradation in poly(3-octylthiophene) thin films. *Polymer Degradation and Stability*, 96(7):1279 – 1285, 2011.

[36] Jose Abad, Nieves Espinosa, Rafael Garcia-Valverde, Jaime Colchero, and Antonio Urbina. The influence of uv radiation and ozone exposure on the electronic properties of poly-3-octyl-thiophene thin films. *Solar Energy Materials and Solar Cells*, 95(5):1326 – 1332, 2011. Special Issue : 3rd International Summit on OPV Stability.

[37] G BINNIG and H ROHRER. Scanning tunneling microscopy. *Helvetica physica acta*, 55(6):726–735, 1982.

[38] G. Binnig, C. F. Quate, and Ch. Gerber. Atomic force microscope. *Phys. Rev. Lett.*, 56:930–933, Mar 1986.

[39] T. R. Albrecht, P. Grutter, D. Horne, and D. Rugar. Frequency modulation detection using high-q cantilevers for enhanced force microscope sensitivity. *Journal of Applied Physics*, 69(2):668–673, 1991.

[40] Kelvin. Contact-electricity of metals. *Philosophical Magazine*, 46:82–120120, 1898. Uk.

[41] M. Nonnenmacher, M. O'Boyle, and H.K. Wickramasinghe. Surface investigations with a kelvin probe force microscope. *Ultramicroscopy*, 4244, Part 1(0):268 – 273, 1992.

[42] V. Palermo, M. Palma, and P. Samori. Electronic characterization of organic thin films by kelvin probe force microscopy. *Advanced Materials*, 18(2):145–164, 2006.

[43] Evan J. Spadafora, Renaud Demadrille, Bernard Ratier, and Benjamin Grevin. Imaging the carrier photogeneration in nanoscale phase segregated organic heterojunctions by kelvin probe force microscopy. *Nano Letters*, 10(9):3337–3342, 2010.

[44] Klara Maturova, Martijn Kemerink, Martijn M. Wienk, Dimitri S. H. Charrier, and Rene A. J. Janssen Janssen. Scanning kelvin probe microscopy on bulk heterojunction polymer blends. *Advanced Functional Materials*, 19(9):1379–1386, 2009.

[45] Obadiah G. Reid, Glennis E. Rayermann, David C. Coffey, and David S. Ginger. Imaging local trap formation in conjugated polymer solar cells: A comparison of time-resolved electrostatic force microscopy and scanning kelvin probe imaging. *The Journal of Physical Chemistry C*, 114(48):20672–20677, 2010.

[46] M. P. Murrell, M. E. Welland, S. J. O'Shea, T. M. H. Wong, J. R. Barnes, A. W. McKinnon, M. Heyns, and S. Verhaverbeke. Spatially resolved electrical measurements of sio[sub 2] gate oxides using atomic force microscopy. *Applied Physics Letters*, 62(7):786–788, 1993.

[47] Yish-Hann Liau, Norbert F. Scherer, and Kent Rhodes. Nanoscale electrical conductivity and surface spectroscopic studies of indium tin oxide. *The Journal of Physical Chemistry B*, 105(16):3282–3288, 2001.

[48] Kevin D. O'Neil, Bryan Shaw, and Oleg A. Semenikhin. On the origin of mesoscopic inhomogeneity of conducting polymers. *The Journal of Physical Chemistry B*, 111(31):9253–9269, 2007.

[49] Hyo Joong Lee and Su-Moon Park. Electrochemistry of conductive polymers. 30. nanoscale measurements of doping distributions and current-voltage characteristics of electrochemically deposited polypyrrole films. *The Journal of Physical Chemistry B*, 108(5):1590–1595, 2004.

[50] B. J. Leever, M. F. Durstock, M. D. Irwin, A. W. Hains, T. J. Marks, L. S. C. Pingree, and M. C. Hersam. Spatially resolved photocurrent mapping of operating organic photovoltaic devices using atomic force photovoltaic microscopy. *Applied Physics Letters*, 92(1):013302, 2008.

[51] Xuan-Dung Dang, Arnold B. Tamayo, Junghwa Seo, Corey V. Hoven, Bright Walker, and Thuc-Quyen Nguyen. Nanostructure and optoelectronic characterization of small molecule bulk heterojunction solar cells by photoconductive atomic force microscopy. *Advanced Functional Materials*, 20(19):3314–3321, 2010.

[52] Cuiying Yang, Jerry G. Hu, and Alan J. Heeger. Molecular structure and dynamics at the interfaces within bulk heterojunction materials for solar cells. *Journal of the American Chemical Society*, 128(36):12007–12013, 2006.

[53] Fabian Etzold, Ian A. Howard, Nina Forler, Don M. Cho, Michael Meister, Hannah Mangold, Jie Shu, Michael Ryan Hansen, Klaus Muellen, and Frederic Laquai. The effect of solvent additives on morphology and excited-state dynamics in pcpdtbt:pcbm photovoltaic blends. *Journal of the American Chemical Society*, 134(25):10569–10583, 2012.

[54] H. Hintz, H.-J. Egelhaaf, H. Peisert, and T. Chasse. Photo-oxidation and ozonization of poly(3-hexylthiophene) thin films as studied by uv/vis and photoelectron spectroscopy. *Polymer Degradation and Stability*, 95(5):818 – 825, 2010.

[55] Frederik C. Krebs. Fabrication and processing of polymer solar cells: A review of printing and coating techniques. *Solar Energy Materials and Solar Cells*, 93(4):394 – 412, 2009. Processing and Preparation of Polymer and Organic Solar Cells.

[56] K. Norrman, A. Ghanbari-Siahkali, and N. B. Larsen. Studies of spin-coated polymer films. *Annual Reports on the Progress of Chemistry, Section C: Physical Chemistry*, 101:174, 2005.

[57] Thomas Tromholt, Matthieu Manceau, Martin Helgesen, Jon E. Carle, and Frederik C. Krebs. Degradation of semiconducting polymers by concen-

trated sunlight. *Solar Energy Materials and Solar Cells*, 95(5):1308 – 1314, 2011. Special Issue : 3rd International Summit on OPV Stability.

[58] Thomas Tromholt, Assaf Manor, Eugene A Katz, and Frederik C Krebs. Reversible degradation of inverted organic solar cells by concentrated sunlight. *Nanotechnology*, 22(22):225401, 2011.

[59] Donald A. Melnick. Zinc oxide photoconduction, an oxygen adsorption process. *The Journal of Chemical Physics*, 26(5):1136–1146, 1957.

[60] Ruediger Berger, Hans-Juergen Butt, Maria B. Retschke, and Stefan A. L. Weber. Electrical modes in scanning probe microscopy. *Macromolecular Rapid Communications*, 30(14):1167–1178, 2009.

[61] S. Hayashi and K. Hayamizu. Chemical-shift standards in high-resolution solid-state nmr (1) c-13, si-29 and h-1 nuclei. *Bulletin of the Chemical Society of Japan*, 64(2):685–687, 1991. ISI Document Delivery No.: FA797 Times Cited: 85 Cited Reference Count: 7 Hayashi, s hayamizu, k Chemical soc japan Tokyo.

[62] Corey R Morcombe and Kurt W Zilm. Chemical shift referencing in mas solid state nmr. *Journal of Magnetic Resonance*, 162(2):479 – 486, 2003.

[63] Matthew O. Reese, Alexandre M. Nardes, Benjamin L. Rupert, Ross E. Larsen, Dana C. Olson, Matthew T. Lloyd, Sean E. Shaheen, David S. Ginley, Garry Rumbles, and Nikos Kopidakis. Photoinduced degradation of polymer and polymer-fullerene active layers: Experiment and theory. *Advanced Functional Materials*, 20(20):3476–3483, 2010.

[64] A. D. Xia, S. Wada, and H. Tashiro. Optical data storage in c[sub 60] doped polystyrene film by photo-oxidation. *Applied Physics Letters*, 73(10):1323–1325, 1998.

[65] Nathaniel P. Curry, Barry Doust, and Daniel A. Jelski. A computational study of the combinatorial addition of oxygen to buckminsterfullerene. *Journal of Cluster Science*, 12(2):385–390, 2001.

[66] H. Neugebauer, C. Brabec, J.C. Hummelen, and N.S. Sariciftci. Stability

and photodegradation mechanisms of conjugated polymer/fullerene plastic solar cells. *Solar Energy Materials and Solar Cells*, 61(1):35 – 42, 2000.

[67] M. T. Lloyd, A. Garcia, J. J. Berry, M. O. Reese, D. S. Ginley, and D. C. Olson. Overcoming degradation in organic photovoltaics: Illuminating the role of fullerene functionalization. *37th IEEE Photovoltaic Specialists Conference (PVSC 37), 19-24 June 2011, Seattle, Washington*, page 6 pp, 2011.

[68] B. Paci, A. Generosi, D. Bailo, V. Rossi Albertini, and R. de Bettignies. Discriminating bulk, surface and interface aging effects in polymer-based active materials for efficient photovoltaic devices. *Chemical Physics Letters*, 494:69 – 74, 2010.

[69] Agnes Rivaton, Sylvain Chambon, Matthieu Manceau, Jean-Luc Gardette, Muriel Firon, Noella Lemaitre, Stephane Guillerez, and Stephane Cros. *Impact of light on organic solar cells: Evolution of the chemical structure, morphology and photophysical properties of the active layer*, volume 7002 of *Proceedings of SPIE*. 2008. Times Cited: 0 Conference on Photonics for Solar Energy Systems II Apr 07-08, 2008 Strasbourg, FRANCE.

[70] K. Norrman, N.B. Larsen, and F.C. Krebs. Lifetimes of organic photovoltaics: Combining chemical and physical characterisation techniques to study degradation mechanisms. *Solar Energy Materials and Solar Cells*, 90(17):2793 – 2814, 2006.

[71] Malcom. H. Levitt. Spin dynamics : Basics of nuclear magnetic resonance, 2008.

[72] K. Schmidt-Rohr and H.W. Spiess. Multidimensional solid-state nmr and polymers, 1994.

[73] Sylvian Cadars, Anne Lesage, Chris J. Pickard, Philippe Sautet, and Lyndon Emsley. Characterizing slight structural disorder in solids by combined solid-state nmr and first principles calculations. *The Journal of Physical Chemistry A*, 113(5):902–911, 2009.

[74] Anne Bohle, Gunther Brunklaus, Michael R. Hansen, Tobias W. Schleuss, Andreas F. M. Kilbinger, Jens Seltmann, and Hans W. Spiess. Hydrogen-

bonded aggregates of oligoaramide-poly(ethylene glycol) block copolymers. *Macromolecules*, 43(11):4978–4985, 2010.

[75] A. Pines, M. G. Gibby, and J. S. Waugh. Proton-enhanced nmr of dilute spins in solids. *The Journal of Chemical Physics*, 59(2):569–590, 1973.

[76] G. Metz, X.L. Wu, and S.O. Smith. Ramped-amplitude cross polarization in magic-angle-spinning nmr. *Journal of Magnetic Resonance, Series A*, 110(2):219 – 227, 1994.

[77] Jan C. Hummelen, Brian W. Knight, F. LePeq, Fred Wudl, Jie Yao, and Charles L. Wilkins. Preparation and characterization of fulleroid and methanofullerene derivatives. *The Journal of Organic Chemistry*, 60(3):532–538, 1995.

[78] R. Mens, S. Chambon, S. Bertho, G. Reggers, B. Ruttens, J. D'Haen, J. Manca, R. Carleer, D. Vanderzande, and P. Adriaensens. Description of the nanostructured morphology of 6,6 -phenyl-c-61-butyric acid methyl ester (pcbm) by xrd, dsc and solid-state nmr. *Magnetic Resonance in Chemistry*, 49(5):242–247, 2011.

[79] Wanzhu Cai, Xiong Gong, and Yong Cao. Polymer solar cells: Recent development and possible routes for improvement in the performance. *Solar Energy Materials and Solar Cells*, 94(2):114 – 127, 2010.

[80] Nikos Tasios, Christos Grigoriadis, Michael Ryan Hansen, Henrike Wonneberger, Chen Li, Hans W. Spiess, Klaus Muellen, K.len, and George Floudas. Self-assembly, dynamics, and phase transformation kinetics of donor-acceptor substituted perylene derivatives. *Journal of the American Chemical Society*, 132(21):7478–7487, 2010. PMID: 20446687.

[81] Almut Rapp, Ingo Schnell, Daniel Sebastiani, Steven P. Brown, Virgil Percec, and Hans Wolfgang Spiess. Supramolecular assembly of dendritic polymers elucidated by 1h and 13c solid-state mas nmr spectroscopy. *Journal of the American Chemical Society*, 125(43):13284–13297, 2003.

[82] Evgeni S. Penev, Vasilii I. Artyukhov, Feng Ding, and Boris I. Yakobson.

Unfolding the fullerene: Nanotubes, graphene and poly-elemental varieties by simulations. *Advanced Materials*, 24:4956–4976, 2012.

[83] Dmytro Dudenko, Adam Kiersnowski, Jie Shu, Wojciech Pisula, Daniel Sebastiani, Hans Wolfgang Spiess, and Michael Ryan Hansen. A strategy for revealing the packing in semicrystalline pi-conjugated polymers: Crystal structure of bulk poly-3-hexyl-thiophene (p3ht). *Angewandte Chemie International Edition*, 2012.

[84] Marco Chiesa, Lukas Buergi, Ji-Seon Kim, Rafi Shikler, Richard H. Friend, and Henning Sirringhaus. Correlation between surface photovoltage and blend morphology in polyfluorene-based photodiodes. *Nano Letters*, 5(4):559–563, 2005.

[85] H. Hoppe, T. Glatzel, M. Niggemann, A. Hinsch, M. Ch. Lux-Steiner, and N. S. Sariciftci. Kelvin probe force microscopy study on conjugated polymer/fullerene bulk heterojunction organic solar cells. *Nano Letters*, 5(2):269–274, 2005.

[86] Rajiv Giridharagopal, Guozheng Shao, Chris Groves, and David S. Ginger. New spm techniques for analyzing opv materials. *Materials Today*, 13(9):50 – 56, 2010.

[87] H. O. Jacobs, H. F. Knapp, and A. Stemmer. Practical aspects of kelvin probe force microscopy. *Review of Scientific Instruments*, 70(3):1756–1760, 1999.

[88] H. O. Jacobs and A. Stemmer. Measuring and modifying the electric surface potential distribution on a nanometre scale: a powerful tool in science and technology. *Surface and Interface Analysis*, 27(5-6):361–367, 1999.

[89] R Radbeh, E Parbaile, J Boucle, C Di Bin, A Moliton, V Coudert, F Rossignol, and B Ratier. Nanoscale control of the network morphology of high efficiency polymer fullerene solar cells by the use of high material concentration in the liquid phase. *Nanotechnology*, 21(3):035201, 2010.

[90] D. Muhlbacher, M. Scharber, M. Morana, Z. Zhu, D. Waller, R. Gaudiana,

and C. Brabec. High photovoltaic performance of a low-bandgap polymer. *Advanced Materials*, 18(21):2884–2889, 2006.

[91] Zhengguo Zhu, David Waller, Russell Gaudiana, Mauro Morana, David Muehlbacher, Markus Scharber, and Christoph Brabec. Panchromatic conjugated polymers containing alternating donor/acceptor units for photovoltaic applications. *Macromolecules*, 40(6):1981–1986, 2007.

[92] Mauro Morana, Matthias Wegscheider, Alberta Bonanni, Nikos Kopidakis, Sean Shaheen, Markus Scharber, Zhengguo Zhu, David Waller, Russell Gaudiana, and Christoph Brabec. Bipolar charge transport in pcpdtbt-pcbm bulk-heterojunctions for photovoltaic applications. *Advanced Functional Materials*, 18(12):1757–1766, 2008.

[93] J. Peet, J. Y. Kim, N. E. Coates, W. L. Ma, D. Moses, A. J. Heeger, and G. C. Bazan. Efficiency enhancement in low-bandgap polymer solar cells by processing with alkane dithiols. *Nat Mater*, 6(7):497–500, July 2007.

[94] C. Soci, I.-W. Hwang, D. Moses, Z. Zhu, D. Waller, R. Gaudiana, C.-J. Brabec, and A.-J. Heeger. Photoconductivity of a low-bandgap conjugated polymer. *Advanced Functional Materials*, 17(4):632–636, 2007.

[95] Markus Scharber, Markus Koppe, Jia Gao, Fabrizio Cordella, and Maria Loi. Influence of the bridging atom on the performance of a low-bandgap bulk heterojunction solar cell. *Advanced materials*, 22(3):367, 2010.

[96] Mauro Morana, Hamed Azimi, Gilles Dennler, Hans-Joachim Egelhaaf, Markus Scharber, Karen Forberich, Jens Hauch, Russell Gaudiana, David Waller, Zenghuo Zhu, Kurt Hingerl, Svetlana S. van Bavel, Joachim Loos, and Christoph J. Brabec. Nanomorphology and charge generation in bulk heterojunctions based on low-bandgap dithiophene polymers with different bridging atoms. *Advanced Functional Materials*, 20(7):1180–1188, 2010.

[97] Eric T. Hoke, I. T. Sachs-Quintana, Matthew T. Lloyd, Isaac Kauvar, William R. Mateker, Alexandre M. Nardes, Craig H. Peters, Nikos Kopidakis, and Michael D. McGehee. The role of electron affinity in determining whether fullerenes catalyze or inhibit photooxidation of polymers for solar cells. *Advanced Energy Materials*, 2012.

[98] J Kettle, H Waters, M Horie, and S-W Chang. Effect of hole transporting layers on the performance of pcpdtbt:pcbm organic solar cells. *Journal of Physics D: Applied Physics*, 45(12):125102, 2012.

[99] David R. Lide. *Handbook of Chemistry and Physics*. CRC Press, 81 edition, 2000.

[100] Sylvain Chambon, Agnes Rivaton, Jean-Luc Gardette, and Muriel Firon. Photo- and thermal degradation of mdmo-ppv:pcbm blends. *Solar Energy Materials and Solar Cells*, 91(5):394 – 398, 2007. Selected Papers from the European Conference on Hybrid and Organic Solar Cells–ECHOS '06.

[101] Agnes Rivaton, Sylvain Chambon, Matthieu Manceau, Jean-Luc Gardette, Noella Lemaetre, and Stephane Guillerez. Light-induced degradation of the active layer of polymer-based solar cells. *Polymer Degradation and Stability*, 95(3):278 – 284, 2010. Special Issue: MoDeSt 2008.

[102] B. Paci, A. Generosi, V. Rossi Albertini, P. Perfetti, R. de Bettignies, and C. Sentein. Time-resolved morphological study of organic thin film solar cells based on calcium/aluminium cathode material. *Chemical Physics Letters*, 461(13):77 – 81, 2008.

[103] Jan Cermak, Bohuslav Rezek, Vera CimrovaÂ¡, Antonin Fejfar, Adam Purkrt, Milan Vanecek, and Jan Kocka. Time-resolved opto-electronic properties of poly(3-hexylthiophene-2,5-diyl): Fullerene heterostructures detected by kelvin force microscopy. *Thin Solid Films*, 519(2):836 – 840, 2010. Special Section: Romanian Conference on Advanced Materials 2009.

[104] Xavier Bulliard, Soo-Ghang Ihn, Sungyoung Yun, Yungi Kim, Dukhyun Choi, Jae-Young Choi, Min Kim, Myungsun Sim, Jong-Hwan Park, Woong Choi, and Kilwon Cho. Enhanced performance in polymer solar cells by surface energy control. *Advanced Functional Materials*, 20(24):4381–4387, 2010.

[105] Steven K. Hau, Hin-Lap Yip, Orb Acton, Nam Seob Baek, Hong Ma, and Alex K.-Y. Jen. Interfacial modification to improve inverted polymer solar cells. *J. Mater. Chem.*, 18(42):5113–5119, 2008.

[106] Todd C. Monson, Matthew T. Lloyd, Dana C. Olson, Yun-Ju Lee, and Julia W. P. Hsu. Photocurrent enhancement in polythiophene- and alkanethiol-modified zno solar cells. *Advanced Materials*, 20(24):4755–4759, 2008.

[107] J. Lue, E. Delamarche, L. Eng, R. Bennewitz, E. Meyer, and H. J. Guentherodt. Kelvin probe force microscopy on surfaces: Investigation of the surface potential of self-assembled monolayers on gold. *Langmuir*, 15(23):8184–8188, 1999.

[108] J. Christopher Love, Lara A. Estroff, Jennah K. Kriebel, Ralph G. Nuzzo, and George M. Whitesides. Self-assembled monolayers of thiolates on metals as a form of nanotechnology. *Chemical Reviews*, 105(4):1103–1170, 2005.

[109] Colin D. Bain, E. Barry Troughton, Yu Tai Tao, Joseph Evall, George M. Whitesides, and Ralph G. Nuzzo. Formation of monolayer films by the spontaneous assembly of organic thiols from solution onto gold. *Journal of the American Chemical Society*, 111(1):321–335, 1989.

[110] G. E. Poirier and E. D. Pylant. The self-assembly mechanism of alkanethiols on au(111). *Science*, 272(5265):1145–1148, 1996.

[111] B. de Boer, A. Hadipour, M. M Mandoc, T. van Woudenbergh, and P. W M Blom. Tuning of metal work functions with self-assembled monolayers. *Advanced Materials*, 17(5):621–625, 2005.

[112] Dana M. Alloway, Michael Hofmann, Darrin L. Smith, Nadine E. Gruhn, Amy L. Graham, Ramon Colorado, Vicki H. Wysocki, T. Randall Lee, Paul A. Lee, and Neal R. Armstrong. Interface dipoles arising from self-assembled monolayers on gold: Uv-photoemission studies of alkanethiols and partially fluorinated alkanethiols. *The Journal of Physical Chemistry B*, 107(42):11690–11699, 2003.

[113] Paul C. Rusu and Geert Brocks. Work functions of self-assembled monolayers on metal surfaces by first-principles calculations. *Physical Review B*, 74(7):073414, 2006. PRB.

[114] V. De Renzi, R. Rousseau, D. Marchetto, R. Biagi, S. Scandolo, and U. del Pennino. Metal work-function changes induced by organic adsorbates: A

combined experimental and theoretical study. *Phys. Rev. Lett.*, 95:046804, Jul 2005.

[115] K. Uosaki and R. Yamada. Formation of two-dimensional crystals of alkanes on the au(111) surface in neat liquid. *Journal of the American Chemical Society*, 121(16):4090–4091, 1999.

[116] Norbert Koch. Organic electronic devices and their functional interfaces. *ChemPhysChem*, 8(10):1438–1455, 2007.

[117] Hisao Ishii, Kiyoshi Sugiyama, Eisuke Ito, and Kazuhiko Seki. Energy level alignment and interfacial electronic structures at organic/metal and organic/organic interfaces. *Advanced Materials*, 11(8):605–625, 1999.

[118] Eisuke Ito, Hiroshi Oji, Hisao Ishii, Kazuyoshi Oichi, Yukio Ouchi, and Kazuhiko Seki. Interfacial electronic structure of long-chain alkane/metal systems studied by uv-photoelectron and metastable atom electron spectroscopies. *Chemical Physics Letters*, 287(1-2):137–142, 1998.

[119] Hiroyuki Sugimura, Yuzuru Ishida, Kazuyuki Hayashi, Osamu Takai, and Nobuyuki Nakagiri. Potential shielding by the surface water layer in kelvin probe force microscopy. *Applied Physics Letters*, 80(8):1459–1461, 2002.

[120] Sandra Hellinger and Stanley I. Sandler. Liquid-liquid equilibria of fuel oxygenate + water + hydrocarbon mixtures. 2. *Journal of Chemical & Engineering Data*, 40(1):321–325, 1995.

[121] Robert W. Zehner, Bradley F. Parsons, Richard P. Hsung, and Lawrence R. Sita. Tuning the work function of gold with self-assembled monolayers derived from x-[c6h4-c:c-]nc6h4-sh (n = 0, 1, 2; x = h, f, ch3, cf3, and och3). *Langmuir*, 15(4):1121–1127, 1999.

[122] S. Rentenberger, A. Vollmer, E. Zojer, R. Schennach, and N. Koch. Uv/ozone treated au for air-stable, low hole injection barrier electrodes in organic electronics. *Journal of Applied Physics*, 100(5):053701–6, 2006.

[123] Yun-Ming Sung, Fang-Chi Hsu, Chiang-Ting Chen, Wei-Fang Su, and Yang-Fang Chen. Enhanced photocurrent and stability of inverted

polymer/zno-nanorod solar cells by 3-hydroxyflavone additive. *Solar Energy Materials and Solar Cells*, 98(0):103 – 109, 2012.

[124] Rajiv Giridharagopal, Glennis E. Rayermann, Guozheng Shao, David T. Moore, Obadiah G. Reid, Andreas F. Tillack, David. J. Masiello, and David S. Ginger. Submicrosecond time resolution atomic force microscopy for probing nanoscale dynamics. *Nano Letters*, 12(2):893–898, 2012.

[125] Brian O'Regan and Michael Gratzel. A low-cost, high-efficiency solar cell based on dye-sensitized colloidal tio2 films. *Nature*, 353(6346):737–740, October 1991.